TU Delft

Delft University of Technology

Experimental investigation of turbulence in canonical wall bounded flows

Pipe flow and Taylor-Couette flow

Gül, Melika

DOI
10.4233/uuid:1a2adab5-0137-47f2-b8a4-a4949f790f60

Publication date
2019

Document Version
Final published version

Citation (APA)
Gül, M. (2019). *Experimental investigation of turbulence in canonical wall bounded flows: Pipe flow and Taylor-Couette flow.* [Dissertation (TU Delft), Delft University of Technology].
https://doi.org/10.4233/uuid:1a2adab5-0137-47f2-b8a4-a4949f790f60

Important note
To cite this publication, please use the final published version (if applicable).
Please check the document version above.

Copyright
Other than for strictly personal use, it is not permitted to download, forward or distribute the text or part of it, without the consent of the author(s) and/or copyright holder(s), unless the work is under an open content license such as Creative Commons.

Takedown policy
Please contact us and provide details if you believe this document breaches copyrights.
We will remove access to the work immediately and investigate your claim.

This work is downloaded from Delft University of Technology.
For technical reasons the number of authors shown on this cover page is limited to a maximum of 10.

MELIKA GÜL

EXPERIMENTAL INVESTIGATION OF TURBULENCE IN CANONICAL WALL BOUNDED FLOWS

PIPE FLOW AND TAYLOR-COUETTE FLOW

EXPERIMENTAL INVESTIGATION OF TURBULENCE IN CANONICAL WALL BOUNDED FLOWS

PIPE FLOW AND TAYLOR-COUETTE FLOW

PROEFSCHRIFT

ter verkrijging van de graad van doctor
aan de Technische Universiteit Delft,
op gezag van de Rector Magnificus Prof. dr. ir. T.H.J.J. van der Hagen,
voorzitter van het College voor Promoties,
in het openbaar te verdedigen op maandag 28 oktober 2019 om 12:30 uur

door

Melika GÜL

Master of Science in Aerospace Engineering
Middle East Technical University
geboren te Tunceli, Turkey.

This dissertation has been approved by the

Promotor: Prof. dr. ir. J. Westerweel

Promotor: Dr. ir. G. E. Elsinga

Composition of the committee:

Rector Magnificus,	Chairman
Prof. dr. ir. J. Westerweel	Technische Universiteit Delft
Dr. ir. G. E. Elsinga	Technische Universiteit Delft

Independent members:

Dr. C. M. Vanderwel	University of Southampton
Prof. dr. D. B. da Silva	Universidade de Lisboa
Prof. dr. D. Tordella	Politecnico di Torino
Prof. dr. S. Hickel	Technische Universiteit Delft
Prof. dr. ir. C. Poelma	Technische Universiteit Delft

This work is part of the research programme of the Foundation for Fundamental Research on Matter (FOM), which is part of the Netherlands Organisation for Scientific Research (NWO).

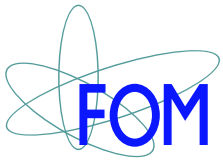

Nederlandse Organisatie voor Wetenschappelijk Onderzoek

Printed by: Gildeprint - Enschede

Copyright © 2019 by M. Gül, all rights reserved
ISBN 978-94-6366-211-6
An electronic version of this dissertation is available at
`http://repository.tudelft.nl/`

to my parents and sister Derya

CONTENTS

SUMMARY ix

SAMENVATTING xiii

1 INTRODUCTION 1

1.1 Background . . . 2

1.2 Aim of the Thesis . . . 5

1.3 Outline of the Thesis . . . 6

2 EXPERIMENTAL FLOW CONDITIONS FOR THE STATISTICALLY STEADY TURBULENT PIPE FLOW 9

2.1 Introduction . . . 10

2.2 Experimental Setup . . . 10

2.3 Results and Discussion . . . 12

2.3.1 First and Second Order Turbulence Statistics . . . 12

2.3.2 Two-Point Spatial Correlations . . . 13

2.4 Conclusions . . . 21

3 SHEAR LAYERS IN A TURBULENT PIPE FLOW 23

3.1 Introduction . . . 24

3.2 Experimental Datasets and Methodology . . . 26

3.2.1 Detection of the Shear Layers . . . 28

3.3 Results and Discussion . . . 29

3.3.1 Three Dimensional Features of Shear Layers . . . 29

3.3.2 Shear Layers in the Spanwise-Wall Normal Plane . . . 34

3.3.3 Shear Layers in the Streamwise-Wall Normal Plane . . . 39

3.4 Conclusions . . . 42

4 UNIFORM MOMENTUM ZONES 47

4.1 Introduction . . . 48

4.2 Results and Discussion . . . 48

4.2.1 UMZs in the Wall Normal-Streamwise Plane . . . 48

4.2.2 UMZs in the Wall Normal-Spanwise Plane . . . 55

4.2.3 Comparison of the UMZ Edges and the Shear Layers . . . 55

4.3 Conclusions . . . 57

5 RAMP-TYPE ACCELERATING/DECELERATING TURBULENT PIPE FLOW 61

5.1 Introduction . . . 62

5.2 Experimental Datasets and Methodology . . . 64

5.3 Results and Discussion . . . 66

5.3.1 First and Second Order Turbulence Statistics . . . 66

5.3.2 Two-Point Spatial Correlations . . . 69

5.3.3 Internal Shear Layers 76
5.4 Conclusions 80
6 TORQUE HYSTERESIS BEHAIOUR OF TAYLOR-COUETTE FLOW 81
6.1 Introduction 82
6.2 Experimental Setup and Methodology 84
6.3 Results and Discussions 88
6.3.1 Torque Measurements 88
6.3.2 PIV Measurements 91
6.4 Conclusions 93
7 SUMMARY AND OUTLOOK 97
7.1 Summary 98
7.2 Outlook 99

REFERENCES 103
ACKNOWLEDGMENTS 115
LIST OF PUBLICATIONS 119

SUMMARY

This thesis aims to contribute to the physical understanding of turbulence in canonical flows. For that purpose, experiments are conducted in a statistically steady turbulent pipe flow, ramp-type accelerating/decelerating turbulent pipe flow and turbulent Taylor-Couette flow. For the first two flows, time-resolved data is acquired in the cross section of the pipe with stereoscopic PIV. The databases spanning over a friction Reynolds number range of $Re_\tau = 340-1259$ are utilised to study coherent motions, in particular the large-scale motions and the internal shear layers bounding them. For the turbulent Taylor-Couette flow study, in addition to torque measurements, high resolution stereoscopic-PIV measurements are performed in the radial-axial planes to investigate the hysteresis phenomenon in the system.

The large coherent motions are studied in an average sense by means of two-point correlation analysis in the cross sections of the pipe as well as in the streamwise-wall normal planes at several reference wall locations. Results reveal large positively correlated regions surrounded by anti-correlated regions both in the statistically steady and unsteady turbulent pipe flows. For the steady cases, these average structures are $\sim 5R$ long in the streamwise direction, and $\sim 0.33R$ wide in the spanwise direction in the logarithmic region, where R is the pipe radius. For all flow conditions, the width of the correlation peaks is observed to increase with the wall distance up to $y/R = 0.4$. Beyond that wall location, on the other hand, no significant changes in the width of the correlation peaks is observed. Furthermore, it is also found that the width of the correlation peaks (based on the correlation coefficient for the streamwise velocity fluctuations, $R_{uu} \geq 0.5$) is very similar for the steady flow conditions provided $Re_\tau \geq 752$. For the unsteady flow conditions, the streamwise length of the average structures maintains its initial length during the deceleration or acceleration. The spanwise length, on the other hand, increases during the deceleration, while it decreases towards the end of the acceleration.

In the second part of this thesis, a comprehensive analysis is performed of the internal shear layers, that bound large-scale energetic motions in a statistically steady turbulent pipe flow. Similar to the previous turbulent boundary layer studies, a significant step-like change in the flow properties is observed to occur across them in the wall normal direction. Furthermore, these layers are observed to be highly dissipative. This work also provides the 3D geometry of these structures. Iso-surfaces marking these shear layers are observed to be quite connected surrounding the whole cross section of the pipe. Even after distinguishing the strong shear regions from the surrounding using 1.5× *local mean* of the shear layer detection parameter (Horuiti & Takagi [54]), the thresholded structures are found to be extended in the spanwise and streamwise directions, while they are relatively thin in the radial direction. Furthermore, the intense shear layers are observed at the edges of

large-scale regions of nearly uniform velocities. Their streamwise length is of the order of the streamwise length scales of the large-scale motions determined through the two point correlations. Moreover, 3D conditional flow analysis relative to the shear layers reveals a strong low-speed flow beneath the averaged shear layers. This low-speed flow is associated with positive wall-normal velocity fluctuations and accompanied by two swirling motions with opposite signs. Also, the average shear layers are observed to be stretched by two opposite azimuthal motions. This could explain why the shear layers are thin in the radial direction. This whole picture conveyed by the 3D conditional analysis points out the connection between shear layers and hairpin structures. Similar type of shear layers having similar geometrical sizes are also found in the accelerating/decelerating turbulent pipe flows. The streamwise velocity profiles across the detected shear layers during the acceleration/deceleration are of the same order of magnitude as those for the steady turbulent cases.

Large-scale motions having nearly uniform streamwise velocities, and their thin bounds (shear layers), are also studied using the histogram of the streamwise velocities. Here, the shear layers are considered as the continuous interfaces of the large-scale motions. Obviously, this method is totally different from the above mentioned 3D detection method. Histogram analysis are performed using two different orientation of the planes, namely streamwise-wall normal plane and cross-section of the pipe. A comparison of these two different methods and different orientation of the planes reveals that the shear layers detected using the 3D method have a very good overlap with the interfaces detected by the histogram method, especially when the wall normal-streamwise planes are used. This confirms the above findings that the shear layers are located at the edge of nearly uniform momentum zones (UMZs), which links small-scale activity (structure) directly to large-scale structure.

Finally, the hysteresis behaviour in Taylor-Couette flow is studied at different shear Reynolds numbers ranging between $Re_s = 1.5 \times 10^4 - 5.5 \times 10^4$. The lowest Reynolds number is around the transition, while the other flow conditions are in the fully turbulent regime. The torque measurements conducted at all these flow conditions reveal hysteresis for a certain range of a number, which is the ratio of the rotational frequencies of the inner and outer cylinders. However, the behaviour of the hysteresis observed at the lowest shear Reynolds number (which is around transition) is found to differ significantly from the behaviour of the hysteresis observed in the fully turbulent regimes. For the fully turbulent conditions, the magnitude of the hysteresis as well as the extent of the a number that it is observed decreases. To investigate whether this phenomenon is artificially generated by the finite geometry of the system or not, further torque measurements are conducted at different aspect ratios of the system, which is achieved simply by changing the water level in the gap. The hysteresis, this time, is observed to become more pronounced although the boundary conditions as well as the flow conditions are kept the same. Although these results imply that the phenomenon is a genuine change happening in the flow, the torque measurements with different boundary conditions reveal that its behaviour and magnitude

is still affected by the boundary conditions of the system. Finally, stereo-PIV experiments are conducted at several a numbers to investigate if and how the large-scale flow structures differ with the occurrence of the hysteresis in the torque. Results reveal that the dominant flow structures at the same flow condition and a number are non-unique, *i.e.* the number of the rolls as well as their sizes change, when the a number is within the hysteresis loop.

SAMENVATTING

Dit proefschrift heeft als doel bij te dragen aan het fysisch begrip van turbulentie in canonieke stromingen. Hiervoor zijn experimenten uitgevoerd in een statistisch stationaire turbulente pijpstroming, versnellende/vertragende turbulente pijpstroming en in turbulente Taylor-Couette-stroming. Voor de eerste twee stromingen zijn tijdsopgeloste data verkregen in de dwarsdoorsnede van de pijp door middel van stereoscopische PIV voor Reynolds getallen gebaseerd op de wrijving van $Re_\tau = 340-1259$. De databases worden gebruikt om coherente structuren te bestuderen, met name de grootschalige structuren en de interne afschuiflagen die deze grote structuren begrenzen. Voor de studie van hysterese in turbulente Taylor-Couette-stroming worden naast koppelmetingen ook stereoscopische PIV-metingen met hoge resolutie uitgevoerd in het radiaal-axiale vlak.

De grote coherente bewegingen worden in een gemiddelde zin bestudeerd door middel van een twee-punts-correlatie in de dwarsdoorsneden van de buis en in de wand-normale vlakken op verschillende referentie posities ten opzichte van de wand. De resultaten onthullen grote positief gecorreleerde gebieden omgeven door anti-gecorreleerde gebieden zowel in de statistisch stationaire als in de ontwikkelende turbulente pijpstromingen. Voor de stationaire gevallen zijn deze gemiddelde structuren $\sim 5R$ lang in de stroomrichting, en $\sim 0.33R$ breed in de spanwijdte voor punten in de logaritmische laag, waarbij R de pijpradius is. Voor alle stromingscondities wordt waargenomen dat de breedte van de correlatiepieken toeneemt met de wandafstand tot $y/R = 0.4$. Voor grotere wandafstanden wordt daarentegen geen significante veranderingen in de breedte van de correlatiepieken waargenomen. Verder is ook gebleken dat de breedte van de correlatiepieken (gebaseerd op de correlatiecoëfficiënt voor de snelheidsbewegingen, $R_{uu} \geq 0.5$) zeer vergelijkbaar is voor stationaire condities waarbij $Re_\tau \geq 752$. Voor de instationaire stromingscondities behoudt de lengte van de gemiddelde structuren zijn initiële lengte tijdens de vertraging of versnelling. De breedte neemt daarentegen toe tijdens de vertraging, terwijl deze afneemt tegen het einde van de versnelling.

In het tweede deel van dit proefschrift wordt een uitgebreide analyse uitgevoerd van de interne afschuiflagen, die de grootschalige energetische bewegingen in een stationaire turbulente pijpstroming van elkaar scheiden. Vergelijkbaar met eerdere turbulentegrenslaagstudies, wordt waargenomen dat in de wand-normale richting er een significante stapachtige verandering in de stromingseigenschappen optreedt over deze lagen. Verder wordt waargenomen dat deze lagen zeer dissipatief zijn. Dit werk laat ook de 3D geometrie van deze structuren zien. Met behulp van iso-oppervlakken die deze afschuiflagen markeren, wordt waargenomen dat ze verbonden zijn en de hele dwarsdoorsnede van de buis omringen. Zelfs na het onderscheiden van de sterke afschuifgebieden van de omgeving met behulp van 1.5× lokaal gemiddelde van de afschuiflaagdetectieparameter (Horuiti

& Takagi [54]), blijken de structuren boven deze drempelwaarde te zijn uitgestrekt in de breedte- en stromingsrichting, terwijl zij relatief dun zijn in de radiale richting. Verder worden de intense afschuiflagen waargenomen aan de randen van grootschalige gebieden met bijna uniforme snelheden. Hun lengte is van dezelfde orde als van die van de grootschalige bewegingen, zoals bepaald door de twee puntcorrelaties. Bovendien onthult de 3D conditionele stromingsanalyse ten opzichte van de afschuiflagen een gebied met sterk verlaagde snelheid onder de gemiddelde afschuiflagen. Deze stroming met lage snelheid wordt geassocieerd met positieve wand-normale snelheidsfluctuaties en gaat gepaard met twee wervelende bewegingen met tegengestelde draairichtingen. Ook wordt waargenomen dat de gemiddelde afschuiflagen worden uitgerekt door twee tegengestelde bewegingen in de omtreksrichting. Dit zou kunnen verklaren waarom de afschuiflagen in radiale richting dun zijn. Dit hele beeld dat naar voren komt door de 3D conditionele analyse wijst op het verband tussen afschuiflagen en haarspeldwervelstructuren. Een soortgelijk type afschuiflagen met vergelijkbare geometrische afmetingen worden ook gevonden in de versnellende/vertragende turbulente pijpstroming. De profielen van de axiale snelheid over de gedetecteerde afschuiflagen tijdens de versnelling/vertraging zijn van dezelfde orde van grootte als die voor de constante turbulente gevallen.

Grootschalige bewegingen met bijna uniforme stroomsnelheden en hun dunne begrenzing (afschuiflagen) worden ook bestudeerd met behulp van het histogram van de stroomsnelheden. Hier worden de afschuiflagen beschouwd als de continue interfaces van de grootschalige bewegingen. Het is duidelijk dat deze methode totaal verschilt van de bovengenoemde 3D detectiemethode. Histogramanalyse wordt uitgevoerd met behulp van twee verschillende oriëntatie van de vlakken waarover het histogram wordt bepaald, namelijk het vlak gegeven door de wand-normale en de stromingsrichting en het vlak van de dwarsdoorsnede van de pijp. Een vergelijking van deze twee verschillende methoden en van de verschillende oriëntatie van de vlakken onthult dat de afschuiflagen gedetecteerd met behulp van de 3D-methode een zeer goede overlap hebben met de interfaces gedetecteerd met de histogrammethode, vooral wanneer het vlak door de wand-normale en de stromingsrichting wordt gebruikt. Dit bevestigt de bovenstaande bevindingen dat de afschuiflagen zich bevinden aan de rand van de uniforme momentumzones (UMZ's), en koppelt de kleinschalige activiteit (structuur) direct aan de grootschalige structuur.

Ten slotte wordt het hysteresegedrag in Taylor-Couette-stroming bestudeerd bij verschillende afschuif-Reynolds-getallen variërend van $Re_s = 1.5 \times 10^4 - 5.5 \times 10^4$. Het laagste Reynolds-getal bevindt zich rond transitie, terwijl de andere stromingscondities zich in het volledig turbulente regime bevinden. De koppelmetingen uitgevoerd bij al deze stroomomstandigheden onthullen hysterese voor een bepaald bereik van het a getal, wat de verhouding van de rotatiefrequenties van de binnenste en buitenste cilinders weergeeft. Het hysterese gedrag waargenomen bij het laagste afschuif-Reynolds-getal (rond transitie) blijkt echter aanzienlijk te verschillen van het hysterese gedrag waargenomen in de volledig turbulente regimes. Voor volledig turbulente omstandigheden neemt de omvang van de hysterese en bereik van a getallen waarover hysterese wordt waargenomen af. Om

te onderzoeken of dit fenomeen kunstmatig wordt gegenereerd door de eindige geometrie van het systeem, worden verdere koppelmetingen uitgevoerd bij verschillende geometrie-verhoudingen van het systeem, wat eenvoudig wordt bereikt door het waterniveau in de opening te veranderen. De hysterese wordt meer uitgesproken naarmate de geometrie-verhouding groter wordt. Hoewel deze resultaten impliceren dat het fenomeen een echte verandering in de stroming is, onthullen de koppelmetingen met verschillende randvoor-waarden dat het gedrag en de omvang ervan nog steeds wordt beïnvloed door de rand-voorwaarden van het systeem. Ten slotte worden stereo-PIV-experimenten uitgevoerd bij verschillende a getallen om te onderzoeken of en hoe de grootschalige stromingsstruc-turen verschillen met het optreden van de hysterese in het koppel. Uit de resultaten blijkt dat de dominante stromingsstructuren bij dezelfde stromingsconditie en a getal niet uniek zijn, dat wil zeggen dat het aantal rollen en hun grootte veranderen, wanneer het a getal zich bevindt binnen de hysterese-gebied.

1

INTRODUCTION

1.1 BACKGROUND

From the large scale mixing in the oceans to harvesting energy from wind farms, turbulent fluid flow plays a crucial role in nature as well as in various applications in science and engineering. However, it still remains a big challenge to describe the full physics of this flow phenomenon and to accurately predict it. This is substantially related to the complex nature of turbulent flow itself; that can be represented by random fluctuations, undergoing nonlinear interactions, over a broad range of scales both in time and space.

Since Osborne Reynolds [102], researchers have developed several approaches to study this complex fluid flow. One way is to describe turbulent flows as collection of organised motions, or *eddies* (Townsend [124]); that have significant coherence over time and space (Robinson [104]). Indeed, studies on coherent motions in turbulent flows have contributed importantly to our knowledge about the nature of these complex fluid flows, in particular for wall turbulence, which is the main focus of this thesis. These coherent motions are also closely associated to the local skin friction (*e.g.* Kravchenko *et al.* [71] and Hwang & Sung [60]). Thus, the ability to manipulate these motions plays a key role for drag reduction over surfaces.

For wall bounded turbulent flows, the near wall region is known to be populated by low speed streaks, which are basically composed of slow fluid regions lifted from the wall by quasi-streamwise vortices (*e.g.* Kline *et al.* [68], Smith & Metzler [114], Schoppa & Hussain [106]). These thin slow fluid regions are oriented in the streamwise direction, and flanked by high speed regions in the spanwise orientation. These low-speed streaks occur with approximately 100 wall units (ν/u_τ) spacing, independent of the Reynolds number (Kline *et al.* [68], Gupta *et al.* [46], Smith & Metzler [114], Kähler [66]). Here, ν is the kinematic viscosity of the fluid, and u_τ is the wall friction velocity.

The outer layer (typically $y > 30\,\nu/u_\tau$), on the other hand, is characterised by energetically significant large scale motions (LSMs). The existence of these structures was first postulated by Townsend [122] based on the long correlation tail of the streamwise velocity fluctuation, the experiments of which were conducted by Grant [39] in a turbulent boundary layer (TBL). The presence of LSMs in wall turbulence was later supported by several other correlation based studies (*e.g.* Bradshaw [17], Blackwelder & Kovasznay [14]) and spectral based studies (*e.g.* Bullock *et al.* [20], Perry & Abell [97], Guala *et al.* [43]). The long correlation tails and the spectral peaks in these studies showed that the length of these LSMs is of the order of $\sim R$ or δ, where R is the radius of the pipe, and δ is the boundary layer thickness. With developments in experimental measurement techniques, Tomkins & Adrian [120] and Ganapathisubramani *et al.* [36] captured some instantaneous snapshots of these structures using particle image velocimetry (PIV). They showed that these long structures are flanked by high speed fluid regions, forming the streaky nature of the log region (typically between $30\,\nu/u_\tau < y < 0.2R$). Compared to the near wall streaks, on the other hand, the streak-like structures in the outer layer are much longer in the streamwise direction and much wider in the spanwise orientation.

In addition to LSMs, wall turbulence has been reported to contain even larger structures, called *very large scale motions* (VLSMs). VLSMs have a streamwise extent of typically $\sim 10R$ (but individual structures can be as long as $30R$) in turbulent pipe and channel flows (Kim & Adrian [67], del Àlamo & Jiménez [137], Guala *et al.* [43], Monty *et al.* [90], Bailey *et al.* [10]). Originally, the low wavenumber peaks in the pre-multiplied energy spectra of the streamwise velocity fluctuations led to the discovery of these structures. Very long elongated regions of high and low speed fluids were also identified in a turbulent boundary layer (TBL) by Hutchins & Marusic [59]. They termed these very large energy motions as *superstructures*. Although large scale motions in internal and external flows are argued to be qualitatively very similar (Balakumar & Adrian [11], Monty *et al.* [91]), Monty *et al.* [91] showed that the large-scale energetic motions in internal flows extend to much higher wall normal distances. Also, they found that the energy of VLSMs corresponds to larger wavelengths in internal flows.

A lot of effort has been put into the investigation of large energy-containing motions in the outer layer of wall turbulence, mainly because these coherent motions carry a substantial portion of the turbulent kinetic energy (TKE) and Reynolds stress. Also, they play an important role in the transport mechanism (Zhou *et al.* [135], Liu *et al.* [79], Ganapathisubramani, Longmire & Marusic [36], Guala, Hommema & Adrian [43], Wu *et al.* [132], Ahn *et al.* [3]). The large scale motions have also been reported to modulate the amplitude of small scale motions near the wall (Hutchins & Marusic [58], Mathis *et al.* [87], Guala *et al.* [44], Ganapathisubramani *et al.* [37]). Furthermore, as discussed in this thesis (Chapter 6), the large coherent motions were found non-unique in Taylor-Couette flow, that is, different large-scale flow states were observed for the same flow conditions. Therefore, understanding the characteristics of these motions is very important for the conceptual picture of wall turbulence as well as its advanced modelling, which still remains a great challenge.

Compared to the near wall cycle there is relatively little known about the origin and evolution of these energetically significant coherent motions. Kim and Adrian [67] and Adrian *et al.* [1] argued that these structures are formed by the streamwise alignment of several packets of hairpin vortices. The formation of individual hairpin vortices in a packet, on the other hand, is explained by *auto-generation* (Zhou *et al.* [135], [136]). The auto-generation is a non-linear process where a new hairpin vortex is formed if the vortex strength is above a certain threshold. Evidence for the hairpin vortex concept was provided by the experimental studies of Christensen & Adrian [24], Dennis and Nickels [26] and Jodai & Elsinga [65]. In these studies and many others (*e.g.* Perry & Chong [98], Head & Bandyopadhyay [53], Zhou *et al.* [135], Marusic [85]), individual or packets of hairpin vortices were argued to be representative features of the attached eddy hypothesis of Townsend [123], [124]. According to this hypothesis, the logarithmic region of wall turbulence is dominated by a hierarchy of energetically significant eddies whose sizes scale with the distance from the wall. Moreover, structures similar to the packets of hairpin vortices were also observed in the DNS of del Àlamo *et al.* [139] in a turbulent channel flow

(TCF), which they termed *vortex clusters*. They argued that the detected vortex clusters cannot grow from the wall because of their short lifetime, but they are formed from the larger vortex clusters in front of them, supporting a top-down approach rather than the bottom-up approach mentioned above.

According to the conceptual picture of Adrian *et al.* [1], based on their PIV experiments in a TBL, the hairpins within a travelling packet induce low speed fluid motions, forming regions of similar streamwise velocity called uniform momentum zones (UMZs) as first introduced by Meinhart & Adrian [88]. This framework was later supported by de Silva *et al.* [111], where they generated UMZs and their structural statistics with superimposing hierarchies of hairpin packets (using attached eddy model) in a turbulent boundary layer. The results of the synthetic data were compatible with their experimental findings, which revealed a log linear increase in the detected number of the zones with Reynolds number. Different to the attached eddy model, Saxton-Fox & McKeon [105] used a spectral model based on travelling waves to represent large scale motions, and they could also produce these structural features of instantaneous turbulent flows and UMZs. The structural nature of a turbulent boundary layer was also investigated recently by Laskari *et al.* [74]. They observed high turbulence activity associated with the ejection events in the log layer for the cases conditioned on the higher number of UMZs than average. The statistics conditioned on the lower number of zones, on the other hand, showed low small-scale activity accompanied by high sweep events near the wall. Apart from these TBL studies, Kwon *et al.* [73] studied the interface demarcating the less turbulent core of a channel flow from the comparatively more turbulent part closer to the wall. They observed that this continuous interface is appearing around 95% of the central velocity of the channel.

These large scale organisations of UMZs are interesting also because they are bounded by relatively thin intense vorticity regions where strong jumps in the flow quantities have been reported (*e.g.* Meinhart & Adrian [88], Adrian *et al.* [1], Eisma *et al.* [32]; de Silva *et al.* [112], Laskari *et al.* [74]). These regions are referred to as internal shear layers or internal interfaces, and together with UMZs they appear to characterise the instantaneous behaviour of wall turbulence. As shown by Eisma *et al.* [32] in a TBL, the internal shear layers have similar characteristics as the turbulent/nonturbulent interfaces (TNTI). Also, they reported that these structures in the outer layer of the TBL move away from the wall faster than the growing rate of the boundary layer. Other than wall turbulence, highly sheared thin regions were also reported in homogeneous and isotropic turbulence both experimentally (*e.g.* Worth & Nickels [131]) and numerically (*e.g.* Ishihara *et al.* [61]). These studies showed that the shear layers are overlapping with the regions of high enstrophy, dissipation and stretching. Moreover, Wei *et al.* [127] and Elsinga *et al.* [34] investigated shear layers in the averaged flow field based on the local frame of reference defined by the eigenvectors of the strain rate tensor. These average shear layer structures were observed to be separating two large-scale regions of nearly uniform streamwise velocities similar to instantaneous observations of UMZs.

Although the importance of large scale motions and thin shear layers bounding them have been recognised by several researchers, there are still several issues that remain to be addressed, in particular, understanding the mechanism by which these structures form and evolve, scaling laws, 3D geometrical features of these structures and the effect of flow confinement. To address some of these questions, a comprehensive analysis is conducted in this thesis on the internal shear layers and the large scale regions of nearly uniform streamwise velocities bounded by them in a turbulent pipe flow.

As briefly presented in this chapter, the large scale coherent motions and the shear layers bounding them have long been a topic of interest for the turbulence community. However, similar to the studies mentioned above, most studies of turbulence are restricted to statistically steady flows. Unfortunately, unsteady turbulent flows have not taken the attention of the researchers as their steady counterparts. This is especially the case for the ramp-type accelerating/decelerating type of unsteady turbulent flows. On the other hand, these type of flows are frequently encountered both in nature (*e.g.* weather and coastal flows) and various engineering applications (*e.g.* turbomachinery, valve opening/closing), therefore, it is quite important to accurately predict and model these types of flows as well. Studies on these flows are also crucial to gain further understanding about the nature of non-equilibrium state of turbulence. Therefore, in this thesis, additional analysis on the coherent structures have been presented for the ramp-type turbulent pipe flows.

1.2 AIM OF THE THESIS

The overarching objective of the present thesis is to improve the physical understanding and the conceptual picture of wall turbulence based on experimental investigations in a turbulent pipe flow and Taylor-Couette flow. The objectives can, more specifically, be articulated in three groups each related to a different flow, namely, the steady turbulent pipe flow, ramp-type accelerated/decelerated turbulent pipe flow and Taylor-Couette flow.

For the case of steady turbulent pipe flow, the primary goal is to provide a comprehensive analysis of the structural properties (including 3D geometry) and kinematics of internal shear layers. Since the shear layers are often studied in TBLs, the second goal of this part is to investigate the effect of the flow confinement on these structures by comparing the results for the shear structures with those for TBLs available in the literature. In addition, the shear layers in the instantaneous turbulent flows are mostly treated as the continuous interfaces of the UMZs, where the identification of the interfaces relies on the identification of the large scale motions. Shear layers, on the other hand, are thin regions that are dominated by small scale activities. Therefore, it is also aimed in this study to compare these two methods and assess whether they represent similar type of structures.

The main goal of the ramp-type accelerating and decelerating turbulent flow study is to investigate the response of turbulence and the development of turbulent structures during the acceleration and deceleration. For unsteady turbulent flows, collecting enough inde-

pendent samples of the same flow conditions, and simultaneously resolving the whole flow development in time, remains a challenge for experimentalists. It is also quite expensive numerically to repeat the ramps for hundreds of times. Therefore, in this part, it is also aimed to show the feasibility of stereo-PIV measurements (with only a few times repeated experiments) for these kind of studies.

Finally, for Taylor-Couette flow, the primary goal is to investigate the hysteresis behaviour (or multiple turbulent states). In particular, the aim is to find out if this phenomenon is a genuine change happening in the flow or influenced by the finite geometry of the system. Three related research questions investigated in this part are: If and how does the aspect ratio as well as the end conditions of the system affect the hysteresis behaviour of a Taylor-Couette flow? Is the hysteresis behaviour also visible in the size and type of the flow structures other than the torque values? How does the magnitude of the hysteresis as well as its behaviour change with different flow conditions (*i.e.* with shear Reynolds numbers)?

1.3 OUTLINE OF THE THESIS

The present thesis consists of seven chapters. After the Introduction (Chapter 1), the experimental flow conditions for statistically steady turbulent pipe flow are introduced in Chapter 2. In addition to the basic turbulence statistics, structural properties of coherent motions are quantified in this chapter in an average sense based on two-point correlations. In Chapter 3, a comprehensive analysis is conducted on the internal shear layers in turbulent pipe flow using the datasets introduced in Chapter 2. The internal shear layers in this chapter are detected using the method of Houriti & Kawaga [54], which provides a 3D representation of these structures as opposed to earlier studies dealing exclusively with the 2D signatures of shear layers. This work is continued in Chapter 4 with a different detection method, the so-called *pdf* method, which was employed by Adrian *et al.* [1] to identify UMZs in a TBL. Following the approach of de Silva *et al.* [111], the shear layers are basically considered to be the continuous interfaces of these detected UMZs. In addition to providing a comparison of the properties of the shear layers detected using these two methods, the relation between the number of the detected UMZs and the associated turbulence properties is analysed in this chapter. In Chapter 5, the response of turbulence and the development of coherent structures along ramp-type accelerated and decelerated turbulent pipe flow is investigated. The ramp-type changes in the bulk Reynolds number are achieved through a nearly constant rate of change in the mass flow rate starting from an initial statistically steady turbulent flow. The acceleration/deceleration is stopped when reaching a prescribed mass flow rate, after which the flow settles again into a statistically steady state. In Chapter 6, the hysteresis behaviour of Taylor-Couette flow, *i.e* the existence of multiple turbulent states, is discussed based on torque as well as stereo-PIV measure-

ments. Finally, in Chapter 7, the main findings of the previous chapters are summarised and discussed along with an outlook for the further research in wall turbulence.

2

EXPERIMENTAL FLOW CONDITIONS FOR THE STATISTICALLY STEADY TURBULENT PIPE FLOW

2.1 INTRODUCTION

As introduced in the previous chapter, this thesis consists of three independent experimental campaigns. The first experimental campaign covers the statistically steady turbulent pipe flow. The data acquired was used to study the spatial structures, in particular, the internal shear layers and the regions of nearly uniform streamwise velocities bounded by them (Chapters 3 & 4). For this work, experiments at four different Reynolds numbers, namely $Re_\tau = 340, 752, 999$ and 1259 were conducted. Here, Re_τ is the friction Reynolds number, $Re_\tau = u_\tau R/\nu$, defined based on the wall friction velocity, u_τ, radius of the pipe, R, and the kinematic viscosity of the fluid (water in this case), ν. The experiments of the second campaign consist of the statistically steady turbulent cases at $Re_\tau = 459$ and 1233, as well as their unsteady counterparts where unsteadiness was imposed through a ramp-type change in the mass flow rate. These unsteady cases are discussed in Chapter 5. Note that for both campaigns, the experiments were performed on the same pipe flow facility where the datasets were acquired using stereoscopic Particle Image Velocimetry (PIV) in the cross section of the pipe. Finally, the experiments of the last campaign were conducted in a Taylor-Couette system to investigate the hysteresis behaviour (multiple turbulent states) of Taylor-Couette flow (see Chapter 6). Since a number of steady turbulent pipe flow conditions were considered for the first two experimental campaigns, a brief analysis is conducted in this chapter to provide a brief summary about the accuracy and repeatability of these experiments as well as to discuss some basic turbulence statistics and the large-scale coherent motions in an average sense.

This chapter is organised as follows: A description of the experimental setup, methodology and flow conditions is given in Section 2.2. This is followed, in Section 2.3, by the results of the first and second order turbulence statistics as well as the structural properties of coherent motions based on two-point correlations. Finally, the findings are summarized in Section 2.4 .

2.2 EXPERIMENTAL SETUP

The experiments were performed in the pipe flow facility at the Laboratory for Aero- and Hydrodynamics of Delft University of Technology. The pipe is ~ 28 m long, and has an inner diameter, D, of 40 mm. The measurement location is 21.82 m downstream of the pipe inlet, corresponding to $545.5D$. Further description of the pipe facility can be found in the thesis of Draad [30].

The turbulent flows were captured with high-speed, stereoscopic particle image velocimetry (PIV), where the measurement plane was perpendicular to the streamwise velocity. A water-filled rectangular box with two prisms was located between the pipe and cameras to decrease the optical distortions due to refraction (Figure 2.1). The stereoscopic PIV measurements provide all three components of velocity across the entire pipe cross

section. To enable the PIV measurements the flow was seeded with 10 μm diameter tracer particles (Sphericell). These are hollow glass spheres, which have a density close to that of water. The entire cross section of the pipe was illuminated by a light sheet generated using a twin-cavity frequency-doubled Nd:YLF laser (25 mJ, 527 nm at 1 kHz). The thickness of this light sheet was ~ 0.9 mm, which was determined based on the method by Wieneke [130].

For the first experimental campaign, the particle images were recorded using two high speed CMOS cameras equipped with a Micro-Nikkor F105 mm objective operating at an aperture number of $f_\# = 11$. The field of view was $2.36R \times 2.58R$, where R is the radius of the pipe. The nominal image magnification and the depth of field is ~ 0.5 and ~ 2.5 mm, respectively. Images were recorded at a frame rate of 0.714 kHz. For each flow condition, $Re_\tau = 340, 752, 999$ and $1259, 1782$ instantaneous velocity fields were obtained. Two additional sets were collected for $Re_\tau = 752$.

The images of the second experimental campaign were recorded with different high speed CMOS cameras (Phantom VEO 640L 4M, LaVision) with a pixel format of 2176×1600, which resulted in a field of view of $2.39R \times 2.23R$. Similar to the first campaign, these high speed cameras were equipped with a Micro-Nikkor F105 mm objective operating at an aperture number of $f_\# = 11$. The time resolved vector fields were captured at a frame rate of 0.859 kHz, and each set of experiments for each flow condition, *i.e.* $Re_\tau = 459$ and 1233, contains 1799 instantaneous velocity fields, and three independent sets were collected for each case.

For both experimental campaigns, calibration, data acquisition, and post-processing were performed with a commercial software package (Davis 8.3.1 & 8.4, LaVision). The PIV images were interrogated with a multi-pass interrogation technique, where the final interrogation windows had a 24×24 pixel size with 75% overlap, corresponding to a spatial resolution based on the window size of $8.8, 11.1, 19.4, 25.8, 29.7$ and 32.5 viscous wall units (ν/u_τ) for $Re_\tau = 340, 459, 752, 999, 1233$ and 1259, respectively. A summary of the flow properties and resolution is given in Table 2.1.

In the present study, r, θ and x represents the radial, azimuthal and axial coordinates, respectively, with the corresponding velocity components, u_r, u_θ, u_x. Similar to the previous studies (*e.g.* Guala, Hommema & Adrian [43], Wu, Baltzer & Adrian [132]), the cylindrical coordinates were transformed to the Cartesian coordinates to enable comparison with other wall bounded turbulent flows. In the new coordinate system, x, $y = R - r$ and $z = r\theta$ represent the streamwise, wall normal and spanwise directions, respectively. The corresponding instantaneous velocities are u, v and w. The time averaged quantities are denoted by capital letters (*e.g.* U), and fluctuations in the velocities are denoted by prime symbol (*e.g.* u'). The superscript '+' is used to denote the inner scaling of length, (*e.g.* $y^+ = yu_\tau/\nu$), and velocity, (*e.g.* $u^+ = u/u_\tau$). The bulk velocity is denoted by U_b. Note that, throughout this thesis, the wall friction velocities, u_τ, obtained from the Blasius empirical correlation [15], was used, unless otherwise stated. This enables a better comparison between the steady and unsteady datasets which are discussed in Chapter 5. The discrep-

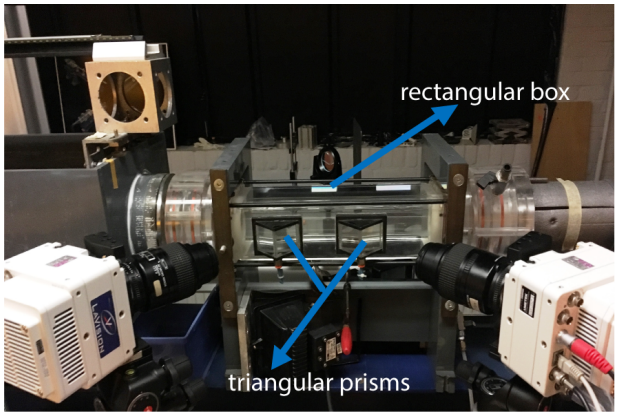

Figure 2.1: Stereoscopic PIV configuration with the high speed CMOS cameras (Phantom VEO). A water-filled rectangular box with two prisms are located between the pipe and cameras to decrease the optical distortions due to refraction.

ancies between the wall friction velocities from the pressure measurements and from the Blasius emprical correlation are less than 3% for any Reynolds numbers studied in this thesis.

Table 2.1: Summary of the steady flow conditions for the turbulent pipe flow, with $d_l^+ = d_l u_\tau / \nu$ and $\Delta t^+ = \Delta t u_\tau^2 / \nu$, where d_l and Δt are the dimension of the PIV interrogation domain (in the light sheet plane) and PIV exposure time delay, respectively.

Re_τ	Re_D	U_b (m/s)	u_τ (m/s)	Spatial Res. d_l^+	Temporal Res. Δt^+	Number of Velocity Fields
340	10944	0.229	0.0142	8.8	0.3380	1782
459	15393	0.396	0.0236	11.1	0.7587	1799×3
752	27092	0.57	0.0316	19.4	1.6656	1782×3
999	37505	0.789	0.042	25.8	2.9377	1782
1233	47727	1.227	0.0634	29.7	5.4752	1799×3
1259	48828	1.024	0.0528	32.5	4.6538	1782

2.3 RESULTS AND DISCUSSION

2.3.1 FIRST AND SECOND ORDER TURBULENCE STATISTICS

To assess the accuracy of the datasets, mean velocity (U^+), root-mean-square velocity fluctuations (u^+_{rms}, v^+_{rms} and w^+_{rms}) and Reynolds shear stress ($-\overline{u'v'}$) profiles were compared with the experimantal and DNS data of Toonder & Nieuwstadt [121] and Lee & Sung [77],

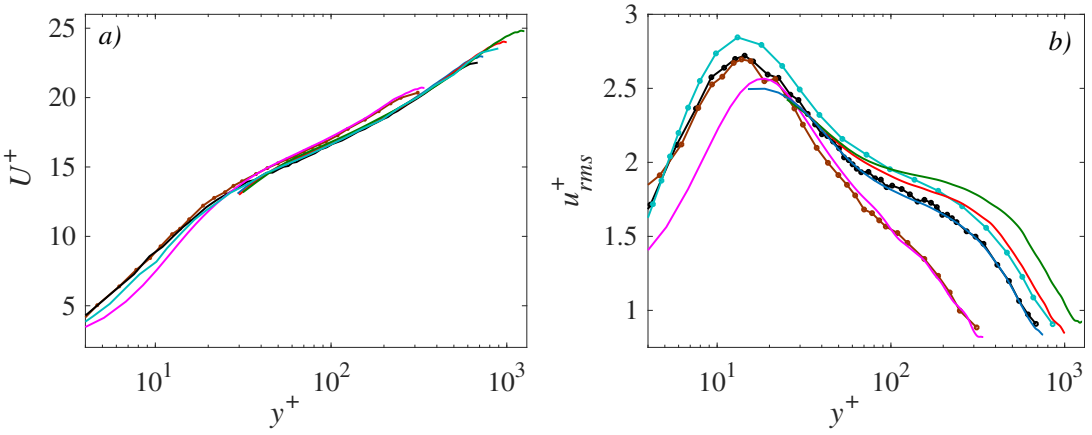

Figure 2.2: (*a*) Mean velocity, U^+, (*b*) *rms* profiles for the streamwise velocity component, u^+_{rms}, for the first experimental campaign. Magenta, blue, red and green lines correspond to current data at $Re_\tau = 340$, 752, 999 and 1259, respectively. Brown and black lines with symbols represent the experimental data of Toonder & Nieuwstadt [121] for $Re_\tau = 315$ and 690, respectively; light blue with symbols (○) represent the DNS results of Lee & Sung [77] for $Re_\tau = 930$.

respectively, at similar Reynolds numbers (Figures 2.2, 2.3 & 2.4). Figure 2.2 and Figure 2.3 show the flow conditions from the first experimental campaign, while Figure 2.4 mainly corresponds to the results from the second experimental campaign. As can be seen from these figures, quite good agreement between the current data and the data of Toonder & Nieuwstadt [121] as well as the DNS of Lee & Sung [77] is observed in the outer region of the turbulent pipe flow. The deviations in the *rms* profiles are less than 2% for all the compared cases beyond $y^+ = 50$. In addition, the results for the similar Reynolds numbers from two different experimental campaigns, *i.e.* 1259 and 1233 (see Figure 2.4) confirms the repeatability of the experiments.

To assess the noise contribution from the PIV images to the *rms* profiles, a 2D Gaussian smoothing over a kernel size of 5×5 was applied to the velocity fields in the spanwise-wall normal planes for each snapshot. After the smoothing, a deviation of 0.7%, 1.7%, 2.1% and 2.6% was observed at a wall normal distance of $y^+ = 50$ for the Reynolds numbers $Re_\tau = 340$, 752, 999 and 1259, respectively. Beyond that wall distance, the deviations gradually become much smaller, which shows that the noise level in the PIV images is not significant. Note that relatively larger deviations near the wall is expected as the near wall region is dominated by the small scales of turbulence, and their contribution to the *rms* profiles are attenuated by the smoothing.

2.3.2 TWO-POINT SPATIAL CORRELATIONS

The characteristic dimensions of the large scale structures can be obtained from two-point correlations. Moreover, this statistical approach allows a comparison of the present re-

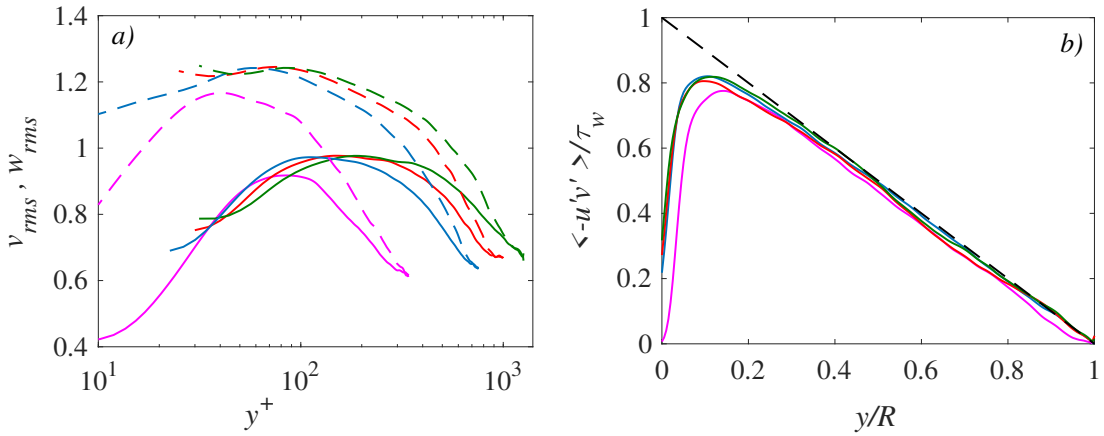

Figure 2.3: (*a*) *Rms* profiles of the wall normal, v^+_{rms} (solid lines), and azimuthal, w^+_{rms} (dashed lines), velocity components in inner coordinates. (*b*) Turbulent shear stress, $-\overline{u'v'}$, profiles normalised by the wall friction, τ_w. Magenta, blue, red and green lines correspond to $Re_\tau = 340$, 752, 999 and 1259, respectively (experimental data of the first campaign). Black dashed line in (*b*) correspond to theoretical total shear stress.

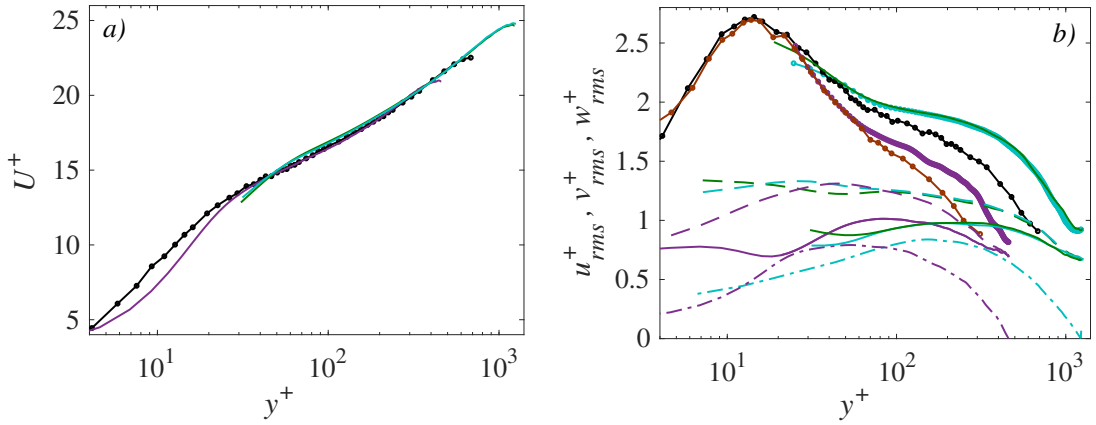

Figure 2.4: (*a*) Mean velocity, U^+, (*b*) turbulence intensity and turbulent shear stress profiles for the second experimental campaign. Streamwise, u^+_{rms}, wall normal, v^+_{rms}, and azimuthal, w^+_{rms}, profiles of the turbulence intensity is represented by the solid lines with filled circles, solid lines and dashed lines, respectively. The turbulent shear stress profiles, $-\overline{u'v'}$, are shown by dashed-dotted lines. Purple and light blue correspond to the results for $Re_\tau = 459$ and 1233, respectively. Brown and black dotted lines represent the experimental data of Toonder & Nieuwstadt [121] for $Re_\tau = 315$ and 690, respectively; while the data represented by green correspond to the current result for $Re_\tau = 1259$ from the first experimental campaign (Figure 2.2).

sults with the available literature. The two point correlation coefficient in the azimuthal (spanwise)-wall normal plane was determined as:

$$R_{uu}(y_{ref}, y, r_z) = \frac{\overline{u'(y_{ref}, z)\, u'(y, z + r_z)}}{u_{rms}(y_{ref})\, u_{rms}(y)} \tag{2.1}$$

Here, y_{ref} and r_z is the reference wall normal position and the spanwise separation, respectively. The overbar represents temporal and spatial average along the homogeneous (*i.e.* azimuthal) direction.

The contours of the resulting two-point correlation coefficient are shown in Figure 2.5 for all the flow conditions considered in this chapter. The contours of the correlation coefficients in (*a, b, c, d*) were determined using single sets, while those in (*e, f, g*) were obtained using three independent sets to see the effect of convergence. Similar to the previous studies (*e.g.* hot wire rake measurements of Bailey *et al.* [10], DNS of Lee *et al.* [76]), the two point correlation contours show large scale coherent motions in an average sense, *i.e.* large positively correlated regions which are surrounded by anti-correlated structures. The positively correlated motions near the wall are observed to be connected to the wall, but they become detached as the reference wall normal position moves beyond the log region. The anti-correlated parts appearing on both sides of the correlated region, on the other hand, come closer to each other as the wall normal distance increases, and with the effect of the confinement, these structures are observed to merge forming a connected anti-correlated motion on top of the positively correlated motion.

Two-point correlations were also evaluated in the streamwise-azimuthal plane at several wall normal positions. Results revealed streamwise elongated regions of positive correlation flanked by anti-correlated parts (Figure 2.6). Here, the streamwise extent of the flow was reconstructed using the local mean value of the streamwise velocity together with Taylor's hypothesis. Taylor's frozen turbulence hypothesis [116] is a frequently invoked assumption in many experiments when the time resolved data is needed to be converted into spatial information. The spatio-temporal correlations of Dennis & Nickels [25] in a turbulent boundary layer (TBL) showed the accuracy of this assumption up to a streamwise distance of 6δ, where δ is the boundary layer thickness. Beyond this distance, however, they reported that the accuracy of this assumption decreases as the streamwise extent further increases.

Further analysis was conducted to quantify the width (l_z) and the length (l_x) of these correlation peaks. The width and the length of the correlations were determined in the streamwise-spanwise planes for $R_{uu} \geq 0.05$ at $r_z = 0$ and $r_x = 0$, respectively (see Figure 2.7). Since the convergence in the tail of the correlation was lower, the following figures also include results evaluated for $R_{uu} \geq 0.5$. In Figure 2.8 and Figure 2.9, the present results are shown together with some data from the existing literature for turbulent pipe, channel (TCF) and boundary layer (TBL) flows. The error bars show the maximum deviation among the independent sets for a certain flow condition (present experiments).

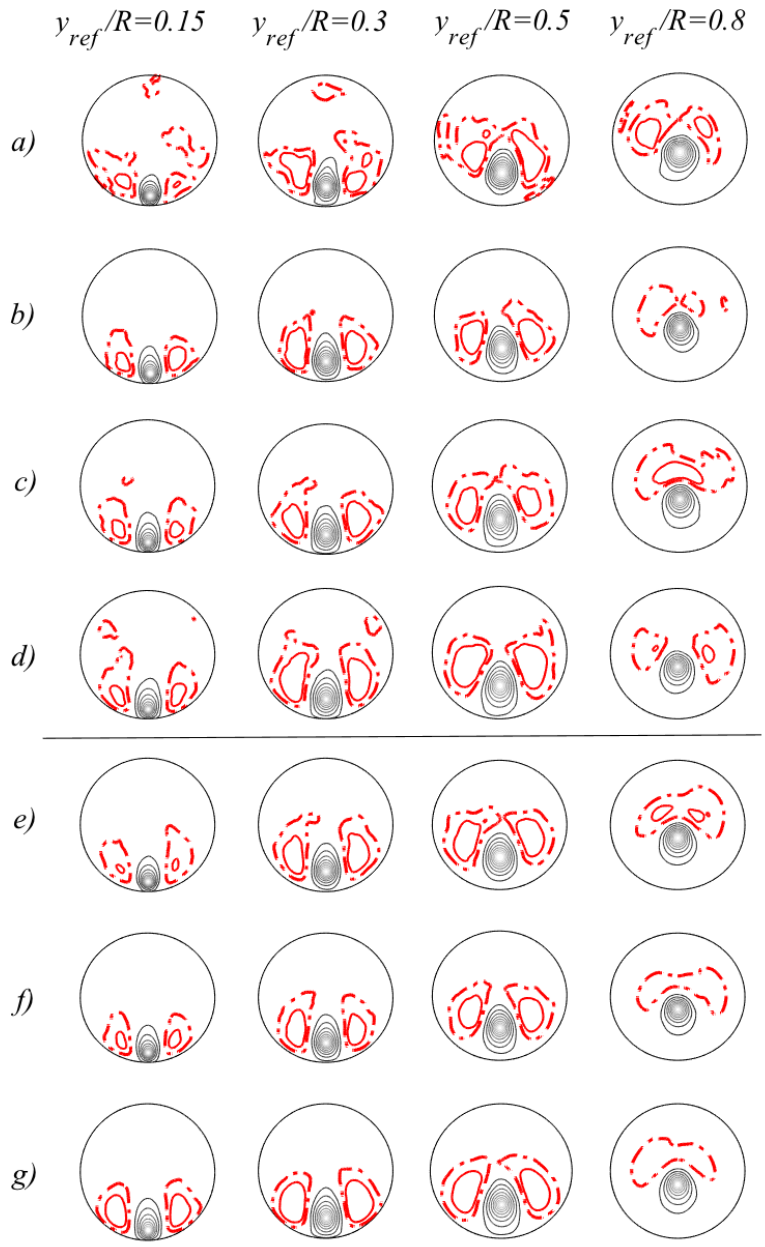

Figure 2.5: Two-point correlation coefficient of the streamwise velocity fluctuations in the azimuthal (spanwise)-wall normal plane with reference points at wall normal locations $y_{ref}/R = 0.15$ (first column), 0.3 (second column), 0.5 (third column), and 0.8 (fourth column). First four rows correspond to the data at (*a*) Re_τ = 340, (*b*) Re_τ = 752, (*c*) Re_τ = 999 and (*d*) Re_τ = 1259, where single sets are used; whereas last three rows correspond to (*e*) $Re_\tau = 459$, (*f*) $Re_\tau = 752$ and (*f*) $Re_\tau = 1233$, where three independent sets are used to determine the correlations. Positive correlations are shown by grey contour lines varied from 0.1 to 1, while dashed-dotted and solid red contour lines correspond to a negative correlation of −0.05 and −0.1, respectively.

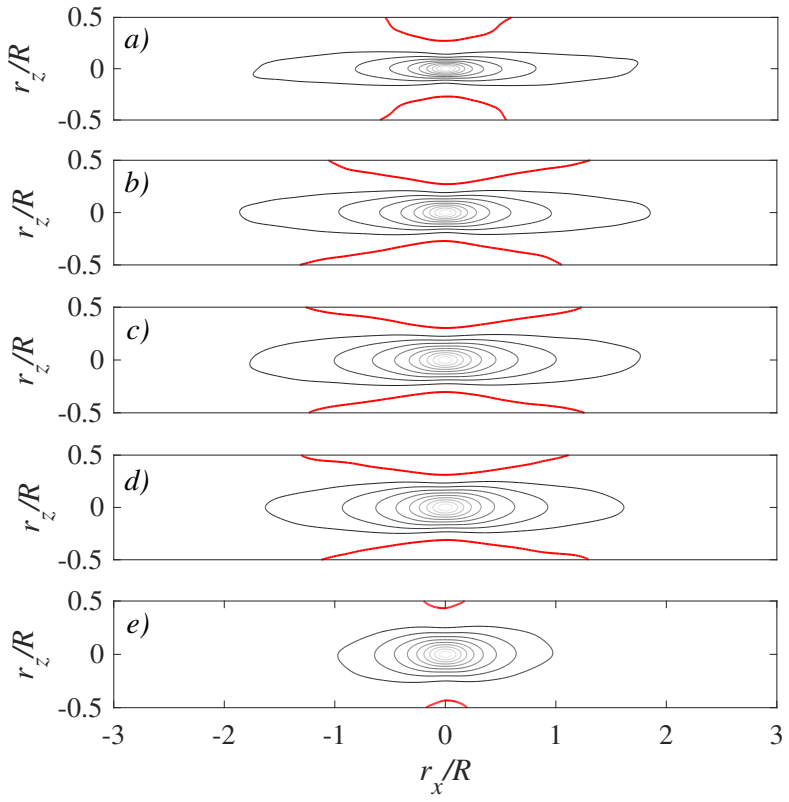

Figure 2.6: Two-point correlation coefficient of the streamwise velocity fluctuations for $Re_\tau = 752$ (consisting of three independent sets) in the streamwise-spanwise planes at several wall normal locations y/R = 0.1 (*a*), 0.2 (*b*), 0.35 (*c*), 0.5 (*d*) and 0.8 (*e*). Positive correlations are shown by grey contour lines varied from 0.1 to 1, while red contour lines correspond to a negative correlation of −0.05.

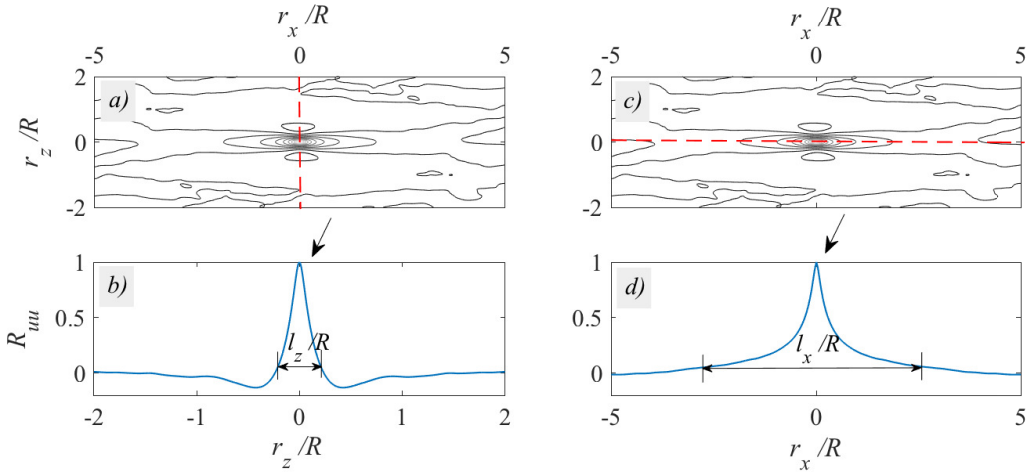

Figure 2.7: Sketch illustrating how the spanwise width, l_z, (*a*, *b*) and the streamwise length, l_x (*c*, *d*) of the correlation coefficients are determined for $R_{uu} = 0.05$. Dashed (red) lines on the correlation contours (*a*) and (*c*) indicate the cross section where the correlation coefficient profiles in (*b*) and (*d*) are obtained.

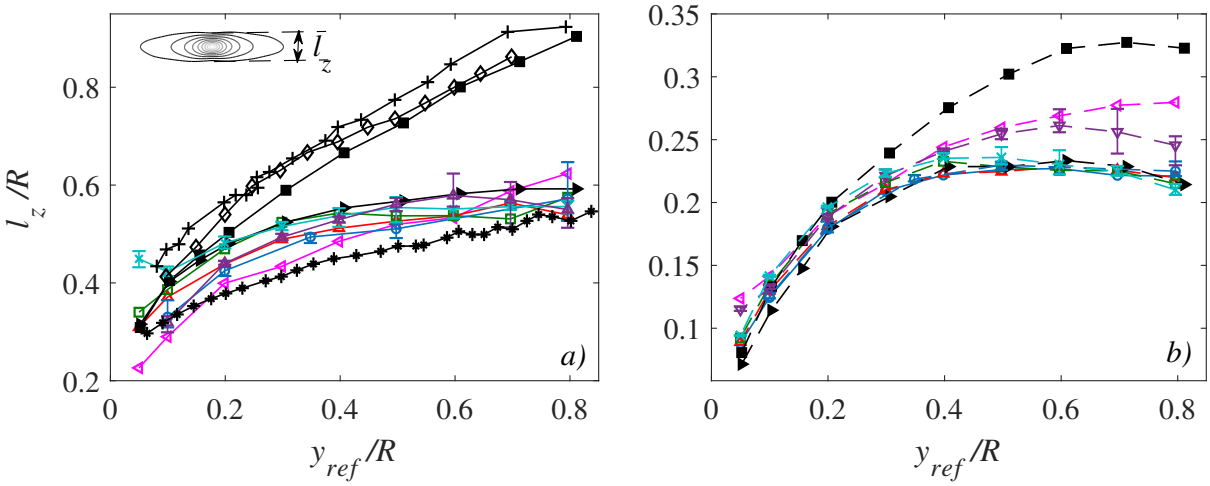

Figure 2.8: Width of the correlation peak, l_z/R, for different wall normal locations, y/R, determined based on $R_{uu} \geq 0.05$ (a), and $R_{uu} \geq 0.5$ (b). Magenta, purple, blue, red, light blue and green correspond to the experimental data for $Re_\tau = 340$ (◁), 459 (▽), 752 (○), 999 (△), 1233 (×) and 1259 (□), respectively. DNS data of Lee *et al.* [77] for turbulent pipe flow and channel flow at $Re_\tau = 930$ is represented by black symbols (►) and (■), respectively. Black (+), (◇), (⋇) symbols, on the other hand, represent the experimental channel flow data of Monty *et al.* [90] at $Re_\tau = 3100$, DNS of Del Alamo *et al.* [138] for channel flow at $Re_\tau = 934$, and boundary layer experiments of Hutchins *et al.* [57] for $Re_\tau = 2800$, respectively.

The present results (Figure 2.8) show that the azimuthal width of the structures is increasing rapidly with the wall distance in the log region (roughly $0.05 \leq y/R \leq 0.2$). This is consistent with the attached eddy hypothesis of Townsend [123], [124]. Beyond the log region, on the other hand, the rate of increase is decreasing, and finally the width of the structures becomes approximately constant near the core of the pipe. When different flow conditions are compared for $R_{uu} \geq 0.5$, the width of the structures is observed to be independent of the Reynolds numbers for $Re_\tau \geq 752$ (Figure 2.8b). However, for the lower Reynolds number cases, *i.e.* $Re_\tau = 340$ and 459, the width of the correlation peak is larger than those at higher Reynolds numbers beyond $y/R = 0.4$. Considering the error bars for $Re_\tau = 459$, 752 and 1233, the difference in the width of the correlation peaks at $0.5 \leq y/R \leq 0.7$ could not be due to the lack of convergence. In Figure 2.8 (b), it is also seen that there is a very good agreement between the current experimental results and the DNS of Lee *et al.* [76] for the turbulent pipe flow at $Re_\tau = 930$. However, when the azimuthal width of the structures in the turbulent pipe flow are compared with the ones in the channel flow studies (Figure 2.8 a & b), clear differences are visible beyond the log layer. This breaks the notion about the similarity between turbulent pipe and channel flows, for which the structural properties of the coherent structures have been reported to be quite similar not only near the wall but also in the wake region (*e.g.* Monty *et al.* [92]).

In Figure 2.9 (a), it is seen that the correlation peaks based on $R_{uu} \geq 0.05$ are quite long in the streamwise direction. The trend of the streamwise length scales of the average

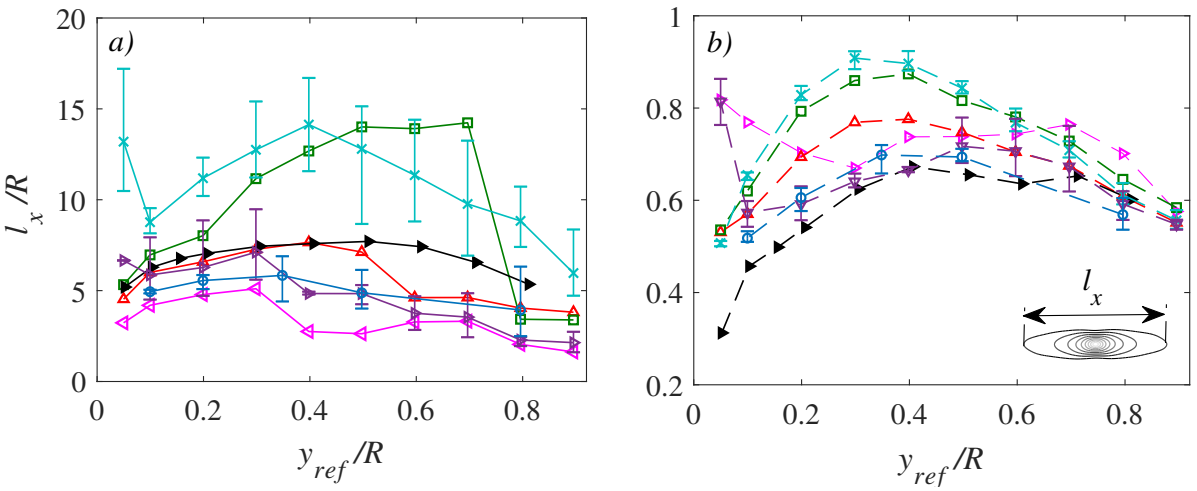

Figure 2.9: Streamwise length of the correlation peak, l_x/R, for different wall normal locations, y/R, determined based on $R_{uu} > 0.05$ (a), and $R_{uu} > 0.5$ (b). Magenta, purple, blue, red, light blue and green correspond to the experimental data for $Re_\tau = 340$ (◁), 459 (▽), 752 (○), 999 (△), 1233 (×) and 1259 (□), respectively. DNS data of Lee *et al.* [77] for turbulent pipe flow at $Re_\tau = 930$ is represented by black (►) symbols.

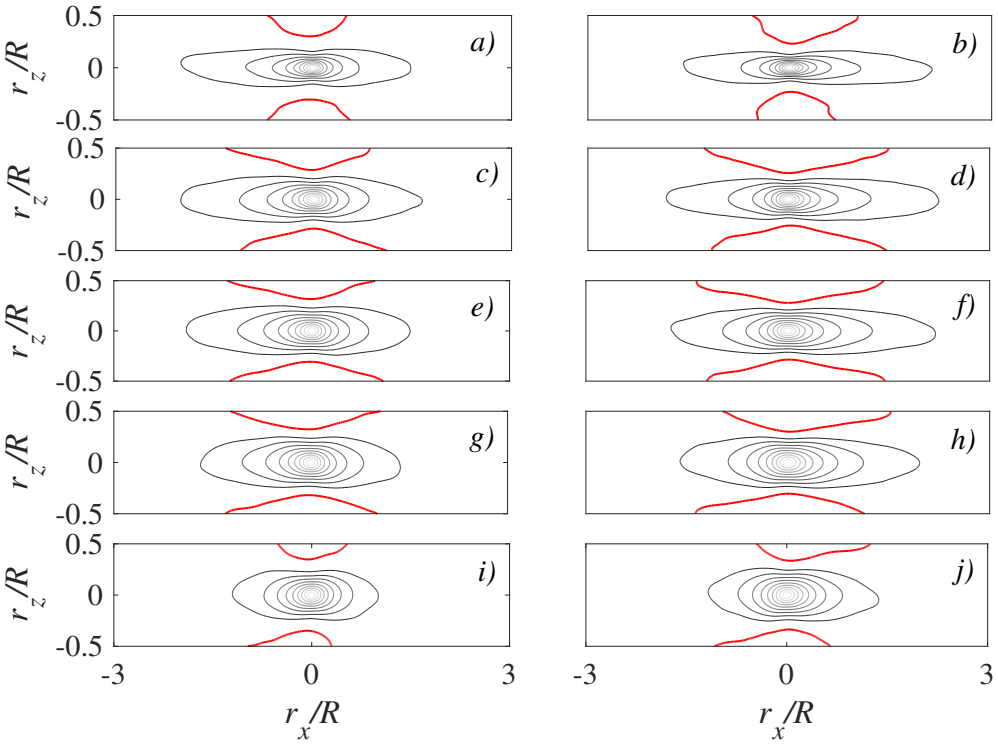

Figure 2.10: Contours of two-point correlation coefficients of the streamwise velocity fluctuations conditioned on the positive events, $u' > 0$ (a, c, e, g, i), and negative events, $u' < 0$ (b, d, f, h, j), for $Re_\tau = 752$ (consisting of three independent sets) in the streamwise-spanwise planes at several wall normal locations $y/R = 0.1$ (a, b), 0.2 (c, d), 0.3 (e, f), 0.5 (g, h) and 0.7 (i, j). Positive correlations are shown by grey contour lines varied from 0.1 to 1, while red contour lines correspond to a negative correlation coefficient of -0.05.

structures is clearer when based on $R_{uu} \geq 0.5$ (Figure 2.9 *b*). Except for the cases at lower Reynolds numbers, *i.e.* $Re_\tau = 340$ and 459, it is seen that the length of the correlation increases in the log region and beyond, similar to the width (Figure 2.8). However, around $y/R = 0.4$, the length starts to decrease with y. It can be also seen in Figure 2.9 (*b*) that for the present flow conditions, $Re_\tau \geq 752$, the streamwise length of the correlation peaks are very similar near the wall as well as near the core of the pipe. However, at all other wall locations, the correlation peaks are longer with higher Reynolds numbers.

Furthermore, two point correlations in the streamwise-spanwise planes were conditioned on the positive streamwise velocity fluctuation events ($u' > 0$) or negative events ($u' < 0$). Contour plots of these correlations are shown in Figure 2.10 for several wall normal locations, *i.e.* $y_{ref}/R = 0.1$, 0.2, 0.3, 0.5 and 0.7. Left column in Figure 2.10 corresponds to the correlations conditioned on the high speed regions ($u' > 0$), while the right column represents the results conditioned on the low speed regions ($u' < 0$). As can be seen in these plots, the correlations are asymmetric in the streamwise direction, such that those that are conditioned on the negative events are biased towards the downstream direction, whereas the correlations conditioned on the positive events are biased towards the upstream direction. These observations are consistent with the results of Lee *et al.* [76]. Furthermore, these authors related this bias to sweep and ejection events. Some differences are also observed in the width and the length of these structures. Figure 2.11 (*a* and *b*) shows the width (for $R_{uu} > 0.3\,\&\,0.5$) and the length (for $R_{uu} > 0.3\,\&\,0.5$) of these conditional correlation peaks, respectively, at several wall normal positions. In Figure 2.11 (*a*), it is seen that the width of these correlations (for both conditions) increases in the log layer as the reference wall normal position increases, similar to the original azimuthal width of the unconditional correlation. Also, similar to the previous observations, the rate of increase is decreasing beyond the log layer. Below $y_{ref}/R \sim 0.5$, the width of the high speed regions is larger than the low speed regions; however, beyond that point the azimuthal width of the low speed regions becomes greater than the high speed regions. These observations are very similar to those of Lee & Sung [77] based on their DNS of turbulent pipe flow, except for the wall normal positions very close to the core of the pipe. For these reference locations, they observed a significant decrease in the width of the structures, whereas in the current experiments no decrease in the width of the structures is found.

For the length of the structures conditioned on positive and negative events, it is seen in Figure 2.11 (*b*) that the correlations are longer for the negative events everywhere in the pipe, except for the wall normal position around $y_{ref}/R = 0.2$. On the other hand, near the wall, the differences are observed to be quite small. Similar to the previous observations about the length of the correlations without any event conditioning, it is seen that the length of the coherent motions also increases near the wall beyond the log layer as the wall normal positions increases. Beyond $y_{ref}/R = 0.2$, the length of the correlation peak is observed to decrease rapidly towards the core of the pipe.

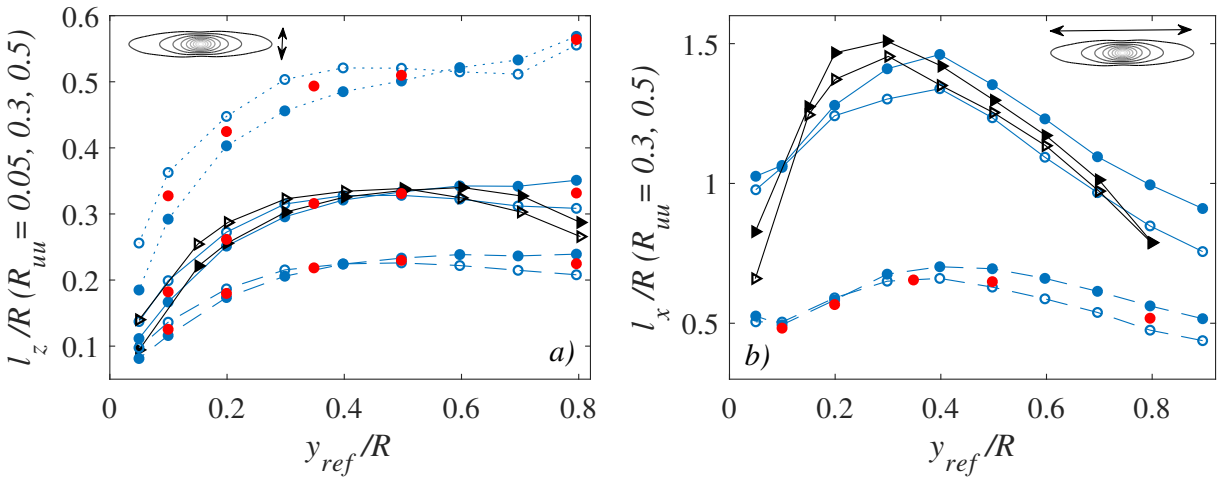

Figure 2.11: (*a*) Azimuthal width, l_z/R, (*b*) streamwise length, l_x/R, of the correlation peak for different wall normal locations, y/R, determined based on $u' > 0$ (open symbols) and $u' < 0$ (filled symbols) for $Re_\tau = 752$ (including three independent sets). Symbols with dotted, solid and dashed lines correspond to the scales for $R_{uu} > 0.05$, 0.3 and 0.5, respectively. DNS data of Lee *et al.* [77] for turbulent pipe flow at $Re_\tau = 930$ is represented by black (►) symbols.

2.4 CONCLUSIONS

In this chapter, two independent PIV measurement campaigns in a turbulent pipe flow were presented, and the accuracy was assessed. The steady flow conditions of the first experimental campaign are $Re_\tau = 340$, 752, 999 and 1259, while the second experimental campaign consists of the steady cases at $Re_\tau = 459$ and 1233.

In the first part of this chapter, the basic turbulence statistics (first and second order) were evaluated for all these flow conditions. The resultant mean, *rms* and turbulent shear stress profiles showed good agreement between the current data and the previously reported ones in the literature (*e.g.* Toonder & Nieuwstadt [121] and Lee & Sung [77]) at similar flow conditions.

In the second part of the chapter, the two point correlations were examined in the spanwise (azimuthal)-wall normal as well as in the streamwise-spanwise planes at several reference wall normal locations. The results revealed positively correlated coherent motions which are surrounded by anti-correlated regions as previously reported by Bailey *et al.* [10] and Lee *et al.* [76]. Furthermore, in this study, the average spanwise and streamwise length of the correlations peaks were assessed at the same wall locations. The trend of the azimuthal width of the peaks were observed to be the same for all the flow conditions where $Re_\tau \geq 752$. In the log layer, the azimuthal width of these structures are increasing quite rapidly, whereas beyond the log region the rate of this increase first decreases and then becomes more or less constant in the wake region. Furthermore, the correlations conditioned on the positive and negative events were observed to be biased towards up-

stream and downstream, respectively, which could be associated to the quadrant events. The length of the correlations conditioned on the negative events are observed to be greater than the ones conditioned on the positive events, in particular beyond the log region. For the azimuthal width of the correlation coefficients, on the other hand, the correlations conditioned on the positive events are wider until the wake region, however, near the core, they are smaller in width compared to their counterparts conditioned on the negative events. All these results were found to be consistent with the DNS results of Lee *et al.* [76] and Lee & Sung [77] at $Re_\tau = 930$.

3

SHEAR LAYERS IN A TURBULENT PIPE FLOW

3.1 INTRODUCTION

Two-dimensional shear layer structures were reported before in TBLs by Meinhart & Adrian [88] and Adrian *et al.* [1] as the regions where high gradients in the streamwise velocity occur; and by Eisma *et al.* [32] as highly sheared regions. Several other studies (*e.g.* Kwon *et al.* [73], de Silva *et al.* [111], Laskari *et al.* [74]), on the other hand, treated the continuous edges of large-scale motions that have nearly uniform streamwise velocities as shear layers. All previous studies involved the identification and analysis of these structures within two-dimensional cross sections of the flow. In this chapter, we present the appearance of the internal shear layers in 3D using a 3D detection method. In addition to their thickness and streamwise extent, we also provide information about the spanwise length of these structures, which has not been reported before. Furthermore, we provide a comprehensive analysis on the 3D signature of these structures in the flow field using conditional analysis.

Starting with the pioneering work of Townsend [122] and Grant [39], a lot of effort has been put into the investigation of large scale motions in wall turbulence. These energetically significant coherent motions have been known to carry a substantial portion of the turbulent kinetic energy (TKE) and Reynolds stress (Liu *et al.* [79], Ganapathisubramani *et al.* [36], Guala *et al.* [43], Wu *et al.* [132], Ahn *et al.* [3]). The momentum exchange across these large scale regions as well as their growth rate, on the other hand, must be largely determined by the thin shear layers bounding them, where large velocity gradients occur (*e.g.* Eisma *et al.* [32]). The large-scale motions have also been reported to modulate the amplitude (Hutchins & Marusic [58], Mathis *et al.* [87], Guala *et al.* [44], Ganapathisubramani *et al.* [37], Awasthi & Anderson [8]) and frequency (Ganapathisubramani *et al.* [37], Baars *et al.* [9], Awasthi & Anderson [8]) of small scale motions near the wall. Therefore, understanding the characteristics of these large-scale motions and their thin bounds (*i.e.* the shear layers) is very important for the conceptual picture of turbulence in canonical wall-bounded flows, as well as its advanced modelling, which still remains a great challenge.

Initially, the long tail of the auto-correlation function of the streamwise velocity fluctuations in the experiments of Grant [39], led Townsend [122] to argue the presence of large scale motions (LSMs) in the outer region of wall turbulence. The existence of LSMs has been supported later by several other correlation-based (*e.g.* Bradshaw [17], Blackwelder & Kovasznay [14]) and spectral-based studies (Bullock *et al.* [20], Perry & Abell [97], Guala *et al.* [43]). The long correlation tails and the spectral peaks in these studies showed that LSMs are of the order of $\sim R$ or $\sim \delta$; where R is the radius of the pipe, and δ is either the boundary layer thickness or half channel height. With developments in experimental measurement techniques, Tomkins & Adrian [120] and Ganapathisubramani *et al.* [36] captured the instantaneous snapshots of these structures using particle image velocimetry (PIV). They showed that these long low-speed structures are flanked by high speed fluid regions, characterising the streaky nature of the log region.

In addition to LSMs, Kim & Adrian [67] hypothesized the existence of very large-scale motions (VLSMs) in a turbulent pipe flow based on the low-wavenumber peaks in the pre-multiplied energy spectra of the streamwise velocity fluctuations. The presence of VLSMs with a streamwise extent as much as $30R$ in turbulent pipe and channel flows was also discussed by del Alamo & Jiménez [137], Guala *et al.* [139], del Alamo *et al.* [138], Monty *et al.* [90], Bailey *et al.* [10]. Very long elongated regions of high and low velocity were, similarly, identified in a TBL by Hutchins & Marusic [59]. They termed these very large energy motions as *superstructures*. Although large scale motions in internal and external flows have been argued to be qualitatively very similar (*e.g.* Balakumar & Adrian, [11], Monty *et al.* [91]), Monty *et al.* showed that the large energy motions in internal flows extends to much higher wall normal distances. Also, they found that the energy of VLSMs corresponds to larger wavelengths in internal flows.

While there are different views about the origin and evolution of these large energy motions, Kim and Adrian [67] and Adrian *et al.* [1] argued that these structures are formed by the streamwise alignment of several hairpin packets. According to the conceptual picture of Adrian *et al.* [1], the hairpins within a packet induce a single low speed velocity region, where the streamwise velocity is nearly uniform, which is referred to as a uniform momentum zone (UMZ). Superimposing hierarchies of hairpin packets using the attached eddy hypothesis, de Silva *et al.* [111] generated UMZs and their structural statistics in a turbulent boundary layer. The results of the synthetic data were compatible with the log linear increase in the detected number of the zones with Reynolds number as observed in their experiments. Recently, Laskari *et al.* [74] associated the higher than average number of the UMZs at a certain Reynolds number with the increased turbulence activity and ejection events in the log region in a TBL. The lower than average number of the UMZs, on the other hand, were coupled with sweep events together with low turbulence activity away from the wall.

The UMZs are interesting also because they are bounded by relatively thin regions of intense vorticity associated with strong jumps in the flow velocity (*e.g.* Meinhart & Adrian [88], Adrian *et al.* [1], Eisma *et al.* [32]). These thin regions are referred to as internal shear layers or internal interfaces, and together with UMZs they characterise instantaneous wall turbulence. The vorticity in the layer may be associated (in part) with hairpins in a packet, which encloses a low-speed (uniform) flow region. However, the 3D structure of the shear layer and possible connection with hairpins are unclear at this point. Similar shear layer structures were also reported by Worth & Nickels [131] and Ishihara *et al.* [61] in homogeneous and isotropic turbulence. Therefore, shear layers may be important general features of turbulence. This finds statistical support in the average flow field associated with turbulent strain, which reveals a shear layer bounded by two large-scale approximately uniform flow regions similar to the instantaneous internal shear layers (Wei *et al.* [127] and Elsinga *et al.* [34])

Although the importance of internal thin shear layers have been recognised by several researches since the late 1900s (*e.g.* Blackwelder & Kovasznay [14] and Robinson [104]),

there are still several issues that remain to be addressed; in particular, their geometrical features, the mechanism by which these structures form and evolve, and if and how their characteristics differ between turbulent flows. Moreover, two different approaches seen in the literature have been employed so far to detect the internal shear layers. The first approach relies on distinguishing the shear through the velocity gradient tensor, while the second one relies on the histogram of the streamwise velocities determined over wall normal-streamwise planes at a certain spanwise position. With the latter method, the shear layers are treated as the continuous interfaces of the UMZs. Obviously, these two methods are rather different from each other, which may introduce some differences. Therefore, it is also of interest to provide a comparison between these two different approaches.

To address some of the above questions, we provide a comprehensive analysis of internal shear layers based on the experimental databases acquired with time-resolved stereoscopic PIV in the cross section of a turbulent pipe flow which can be reconstructed into quasi-instantaneous 3D realizations of the flow, following van Doorne & Westerweel [29]. In particular, we investigate the geometrical properties of these shear layers and their 3D signature in the flow field through conditional sampling and two point correlations. Also, we provide a comparison between the above mentioned 3D detection method and the histogram method (Chapter 4). We carry this analysis for four different flow conditions, *i.e.* $Re_\tau = 340, 752, 999$ and 1259, to examine if and how their properties change with Reynolds number.

This chapter is organised as follows: A description of the datasets used in this chapter as well as the 3D detection method for the internal shear layers are given in Section 3.2. The geometrical properties of the shear layers are discussed in Section 3.3, and the flow profiles/fields conditioned on the layers are exemplified and quantified for four different Reynolds numbers. Finally, the findings are summarized in Section 3.4.

3.2 EXPERIMENTAL DATASETS AND METHODOLOGY

For this study, the experimental databases acquired with stereoscopic particle image velocimetry (PIV) in the cross section of a turbulent pipe flow were utilised. The databases span over four different friction Reynolds numbers, namely $Re_\tau = 340$, 752, 999 and 1259. Here, the friction Reynolds number, $Re_\tau = u_\tau R/\nu$, is defined based on the wall friction velocity, u_τ, radius of the pipe, R, and kinematic viscosity of the fluid, ν, which is water in the present experiments. For the details about the experimental setup (both the pipe facility and measurement technique) as well as for a discussion of the accuracy of the experiments, the reader is referred to Chapter 2.

Since the shear layer detection method is based on an evaluation of the velocity derivatives, further assessment was carried out on the velocity gradients, for $y/R = 0.1{-}1$. The velocity gradients were obtained by applying a second order regression filter over a kernel size of $5\times 5\times 5$ (Elsinga *et al.* [33]). Here, the local mean streamwise velocity along with

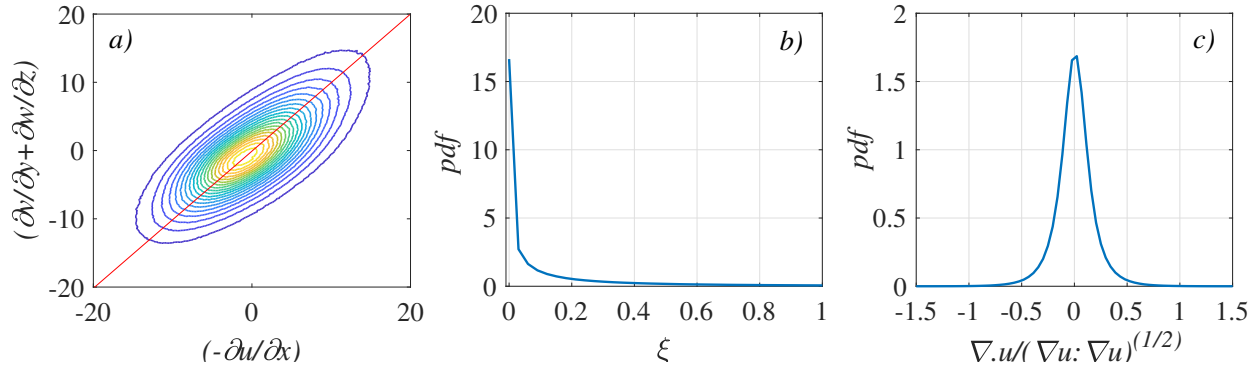

Figure 3.1: (*a*) *Joint pdf* of $(\partial v/\partial y + \partial w/\partial z)$ and $(-\partial u/\partial x)$. The contours are from 0.05 to 0.95 with an increment of 0.05. *Pdf* of the parameter ξ (*b*) and divergence of the vector field $\nabla.u$ which was normalized by the 2-norm of the velocity gradient tensor, $(\nabla u{:}\nabla u)^{1/2}$ (*c*). All these profiles were determined between the wall normal location of $y/R = 0.1 - 1$.

the Taylor hypothesis was used to convert the temporal derivatives into the out-of-plane component of the velocity gradient. The *joint pdf* of $(\partial v/\partial y + \partial w/\partial z)$ and $(-\partial u/\partial x)$, presented in Figure 3.1 (*a*) for $Re_\tau = 752$, shows that the data tends to the red diagonal line, which is indicative of the divergence-free condition, as required for mass conservation in an incompressible fluid. The data away from the diagonal, *i.e.* non-zero divergence, indicates a finite measurement error, which is quantified by the *rms* divergence error. For the flow conditions, $Re_\tau = 340$, 752, 999 and 1259, the *rms* divergence error is 1.8, 4.5, 6.2 and 8 s^{-1}, respectively. All these values are consistent with the values reported by Jodai & Elsinga [65] and Eisma [64] for tomographic PIV (TPIV) in a TBL. The increase in the *rms* divergence with Reynolds number is mainly due to the effect of the decreased spatial resolution in x. The local divergence error was further assessed using two other parameters, *i.e.* ξ (as proposed by Zhang *et al.* [134]) and $\nabla.u$ normalised by the 2-norm of the velocity gradient tensor $(\nabla u{:}\nabla u)^{1/2}$. Here, ξ is defined as:

$$\xi = \frac{(\partial u/\partial x + \partial v/\partial y + \partial w/\partial z)^2}{(\partial u/\partial x)^2 + (\partial v/\partial y)^2 + (\partial w/\partial z)^2} \tag{3.1}$$

Higher values of ξ implies higher divergence error. In the present study, the mean value of ξ is found to be 0.07, 0.18, 0.27, 0.35 for $Re_\tau = 340$, 752, 999 and 1259, respectively, which is consistent with the ranges reported by Zhang *et al.* [134] ($\xi = 0.07 - 0.74$) for their turbulent channel flow (TCF) measurement using holographic PIV and by Casey *et al.* [21] ($\xi = 0.09 - 0.36$) for their turbulent jet flow experiments with scanning TPIV. From the *pdf* of $\nabla.u/(\nabla u{:}\nabla u)^{1/2}$, a mean value of approximately zero is obtained for each flow condition, whereas the *rms* value is 0.110, 0.139, 0.153 and 0.166 for $Re_\tau = 340$, 752, 999 and 1259, respectively. These parameters are also within the ranges that have been reported previously (*e.g.* Casey *et al.* [21], Mullin & Dahm [93] and Ganapathisubramani *et al.* [35]).

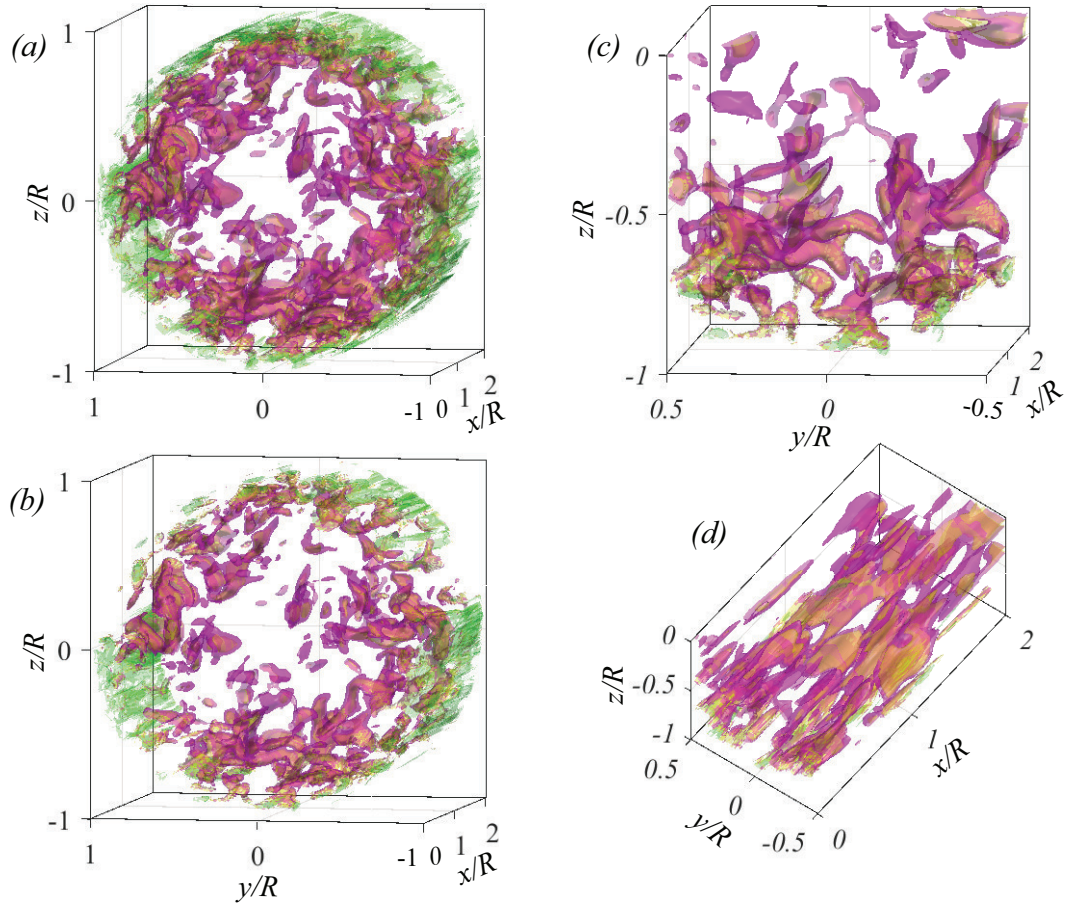

Figure 3.2: Instantaneous three dimensional views of the detected shear regions, where iso-surfaces are representing $\left[A\right]/\left[\overline{A}\right]_{y/R=0.2} = 0.5$ (magenta), 1 (yellow) and 5 (green). Azimuthally averaged *local mean* (*a*) and 1.5× *local mean* (*b*) shear values are used to distinguish the intense shear regions from the surrounding. Here, $\left[\overline{A}\right]_{y/R=0.2}$ is both time and azimuthal averaged shear value at the wall location $y/R = 0.2$. (*c*) & (*d*) show two closer views from different perspectives with the latter threshold.

3.2.1 DETECTION OF THE SHEAR LAYERS

The shear regions were detected using the identification method of Horuiti & Takagi [54] for vortex sheet like structures. This method is based on the correlation between the strain rate, $S_{ij}[=1/2(\partial u_i/\partial x_j+\partial u_j/\partial x_i)]$, and vorticity, $\Omega_{ij}[=1/2(\partial u_i/\partial x_j-\partial u_j/\partial x_i)]$, tensors, which is represented by the symmetric tensor $A_{ij} = S_{ik}\Omega_{kj} + S_{jk}\Omega_{ki}$. After the eigenvalues of this symmetric tensor are determined, they are ordered according to the alignment of their eigenvectors with the vorticity vector. The eigenvalue whose eigenvector has the maximum alignment is represented by $\left[A_{ij}\right]_z$. The largest remaining eigenvalue is represented by $\left[A_{ij}\right]_+$, and the last remaining one by $\left[A_{ij}\right]_-$. The eigenvalue $\left[A_{ij}\right]_+$ is a measure for the local shear content in a point and will be used to identify vortex sheet like structures. Throughout this chapter, we simply use $\left[A\right]$ to represent $\left[A_{ij}\right]_+$.

To distinguish the (intense) shear layers, we applied a threshold based on the local mean value, which was determined for each snapshot by averaging the instantaneous shear quantities in the azimuthal direction, $\left[A\right]$, for a given radial position. Note that the detected shear regions were very similar when time averaging was performed in addition to azimuthal averaging. We employed two different threshold strengths, *i.e the local mean* and 1.5× *the local mean* value, and identified the regions exceeding these thresholds as internal shear layers. With the higher threshold it was observed that the core of the detected shear layers are overlapping fairly well with the peaks of the instantaneous wall-normal profiles of $\left[A\right]$. Therefore, in the remainder of this chapter, results with the latter threshold are presented. In addition, throughout this chapter, figures and the corresponding information belong to the condition $Re_\tau = 752$, unless the Reynolds number is specified.

As a final note in this section, the shear regions detected using $\left[A\right]$ were observed to be overlapping fairly well with the shear layers identified using the 2D *Triple Decomposition Method* (TDM) of Kolář [69], which also was employed to distinguish shear regions in turbulent flows (*e.g.* Maciel *et al.* [83], Eisma *et al.* [32]). However, the detected regions with $\left[A\right]$, which is a 3D method, were observed to better define the azimuthal features of the structures.

3.3 RESULTS AND DISCUSSION

3.3.1 THREE DIMENSIONAL FEATURES OF SHEAR LAYERS

In Figure 3.2 (*a*, *b*), the detected shear regions using the *local mean* and 1.5× *local mean* value of the shear are shown, respectively. In (*c*) and (*d*) two closer views are presented using the latter threshold. As can be seen in these figures, the near wall region of the pipe is more densely populated by these structures as compared to the core region. Also, these shear regions are fairly long both in the azimuthal and the streamwise direction, while they are relatively thin in the radial (wall normal) direction, forming layer like structures. The structural features of the shear layers are further analysed below on different cross sections of the pipe, *i.e.* wall normal-spanwise planes (Figure 3.3) and wall normal-steamwise planes (Figure 3.4).

Figure 3.3 (*a*) shows an instantaneous snapshot of the streamwise velocity together with the detected shear regions in the spanwise-wall normal plane. The shear value corresponding to the magenta surfaces ($\left[A\right]/\left[\overline{A}\right]_{y/R=0.2} = 0.5$) is just above the noise level, while the blue and black surfaces represent very strong shear regions that appear close to the wall. These surfaces form sheet like regions, which appear to be connected in the spanwise direction surrounding the entire cross section of the pipe, especially near the wall. The shear content of the same snapshot of the flow is shown in Figure 3.3 (*b*). Here, the local shear values are normalized by the azimuthally averaged shear values (for each radial position) of the same snapshot. This results in intense regions of shear which are overlapping with

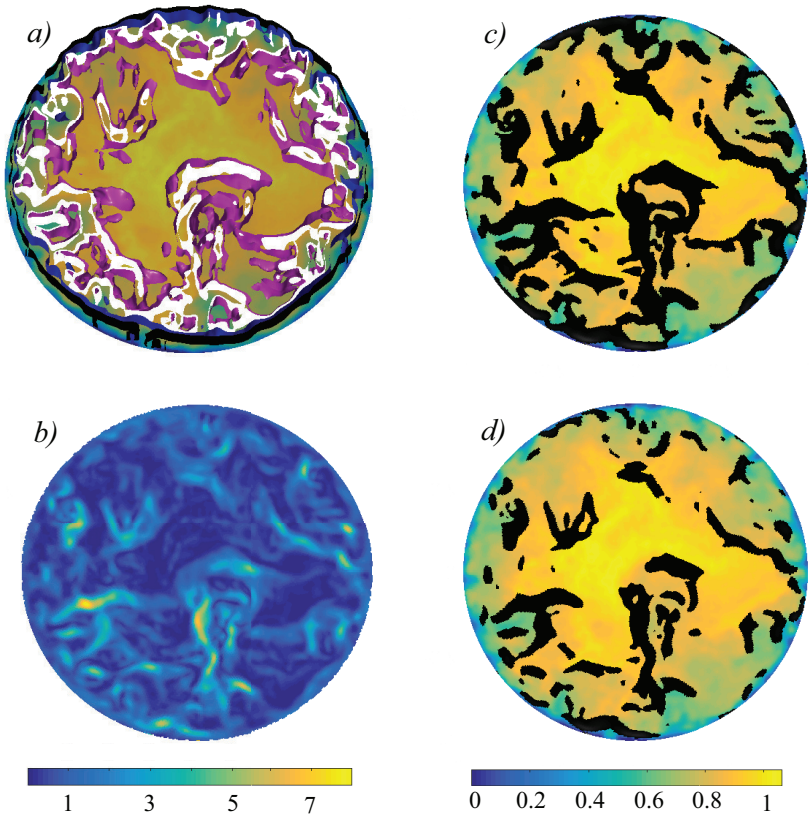

Figure 3.3: (*a*) Iso-surfaces of the shear regions for $\left[A\right]/\left[\overline{A}\right]_{y/R=0.2} = 0.5$ (magenta), 1 (white), 10 (blue) and 25 (black) for an instantaneous snapshot of the cross section of the pipe. Part of the iso-surfaces until a streamwise extent of $0.006R$ is shown here. (*b*) Shear field of the same instantaneous snapshot, where the shear values are normalised by the azimuthally averaged shear value at each wall normal location, the values are presented by the colourbar below. (*c*) and (*d*) represents the intense shear regions (shown by black) greater than the *local mean* and 1.5×*local mean* shear values, respectively. Background map in (*a*), (*c*) and (*d*) represents the instantaneous streamwise velocity field normalised by the central velocity of the pipe, u/U_{cl}.

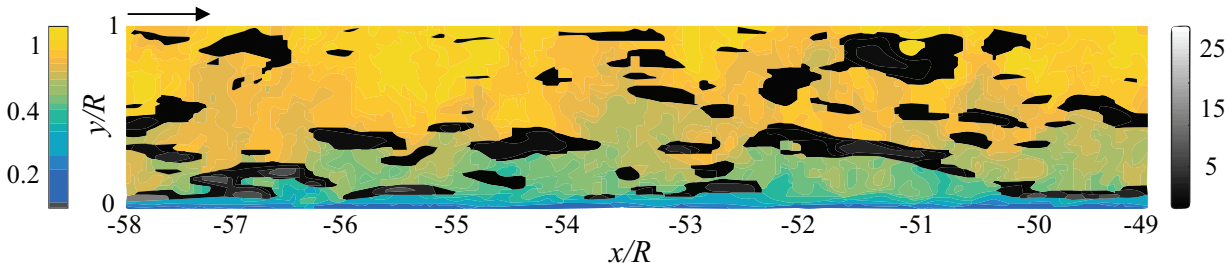

Figure 3.4: Sample instantaneous field of the streamwise velocity, u, normalised by U_{cl} (color map) in the wall normal (y)-streamwise (x) plane together with the detected shear regions, $\left[A\right]$ (shown by the gray contours), normalised by the mean shear value at $y/R = 0.2$. The streamwise extent is reconstructed using the bulk velocity, U_b. Arrow indicates the direction of the flow.

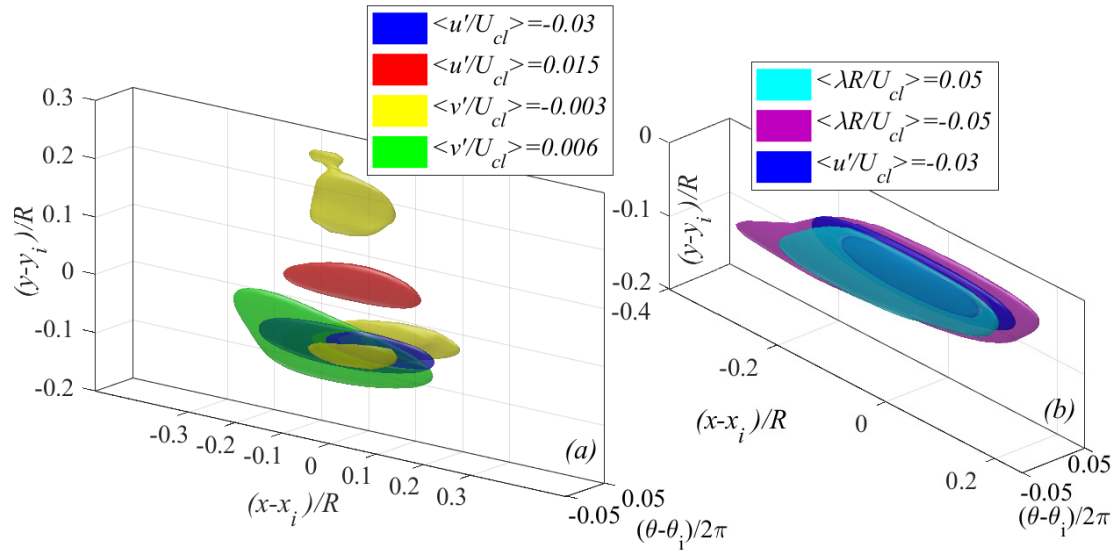

Figure 3.5: Iso-surfaces of the streamwise and wall-normal velocity fluctuations (*a*), and swirling motions together with the low speed flow (*b*), that are remapped with respect to the wall-normal centres of the detected shear layers. Here, only the shear layers between $y/R = 0.15 - 0.2$ are considered. y_i, x_i and θ_i corresponds to the wall normal, streamwise and azimuthal position of the shear layers, respectively. Blue, red, yellow and green surfaces in (*a*) correspond to $< u'/U_{cl} >= -0.03$, $< u'/U_{cl} >= 0.015$, $< v'/U_{cl} >= -0.003$ and $< v'/U_{cl} >= 0.006$, respectively. The streamwise extent is reconstructed using the local conditional-mean streamwise velocities. Iso-surfaces in cyan and magenta in (*b*) represent a swirling strength of $< \lambda R/U_{cl} >= 0.05$ and $< \lambda R/U_{cl} >= -0.05$, respectively.

the iso-surfaces in Figure 3.3 (*a*). After applying a threshold, based on the *local mean* (Figure 3.3 (*c*)) and 1.5×*local mean* (Figure 3.3 (*d*)), these intense shear regions can be distinguished from the surrounding. Based on the thresholding criterion, the thickness and the spanwise length of the structures varies somewhat, as expected. However, they remain relatively thin compared to their spanwise length. Similar to Figure 3.3 (*a, b*), the structures identified by the applied threshold in Figure 3.3 (*c, d*) are observed to surround the core region of the pipe, which is less turbulent than the region near the wall. A similar observation was reported before by Kwon *et al.* [73] for a turbulent channel flow, where they argued that a continuous interface marking a jump in the streamwise velocity demarcates the quiescent core region.

From a visualisation of the detected shear layers in the streamwise-wall normal plane (Figure 3.4), it can be seen that the layers are extended in the streamwise direction, and that they are relatively thin compared to their streamwise length supporting the previous observations in Figure 3.3. Also, the layers in the turbulent pipe flow are observed to be bounding large-scale regions of nearly uniform streamwise velocities, as previously reported observations by Meinhart & Adrian [88], Adrian *et al.* [1] and Eisma *et al.* [32] in a TBL.

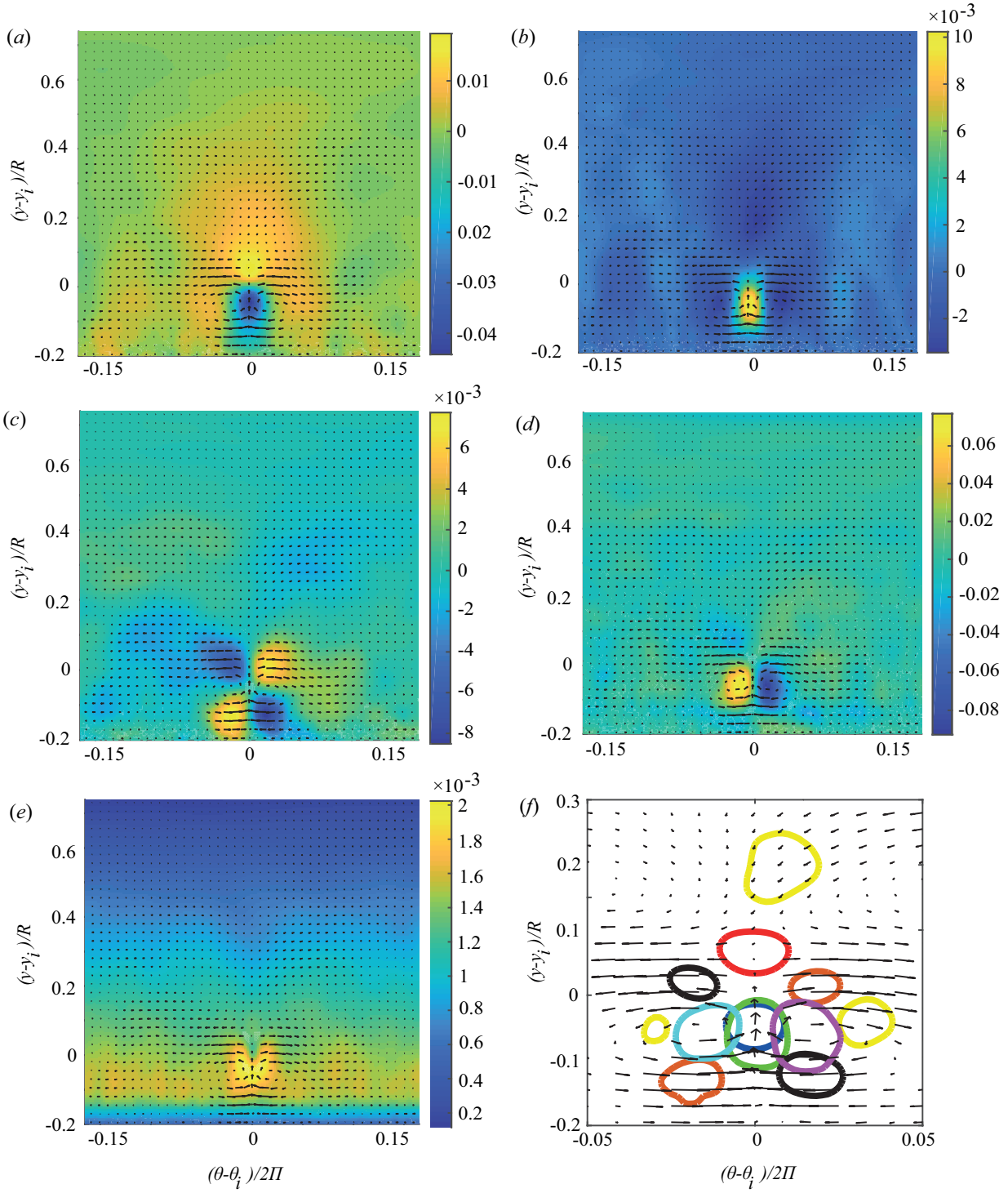

Figure 3.6: Conditionally averaged fields around the shear layers for (a) streamwise velocity fluctuation, $< u'/U_{cl} >$, (b) wall-normal velocity fluctuation, $< v'/U_{cl} >$, (c) spanwise velocity fluctuation, $< w'/U_{cl} >$, (d) swirling strength, $< \lambda R/U_{cl} >$, and (f) Reynolds shear stress, $< -u'v'/U_{cl}^2 >$. (f) shows a close view for all components of the velocity fluctuations and swirling strength. Here, contour lines in blue, red, yellow, green, black, orange, purple and cyan correspond to $< u'/U_{cl} >= -0.03$, $< u'/U_{cl} >= 0.015$, $< v'/U_{cl} >= -0.03$, $< v'/U_{cl} >= 0.06$, $< w'/U_{cl} >= -0.06$, $< w'/U_{cl} >= 0.06$, $< \lambda R/U_{cl} >= -0.05$ and $< \lambda R/U_{cl} >= 0.05$, respectively. Arrows indicate the average vector field for $< v' >$ and $< w' >$. Results correspond to the plane at $(x - x_i = 0)$.

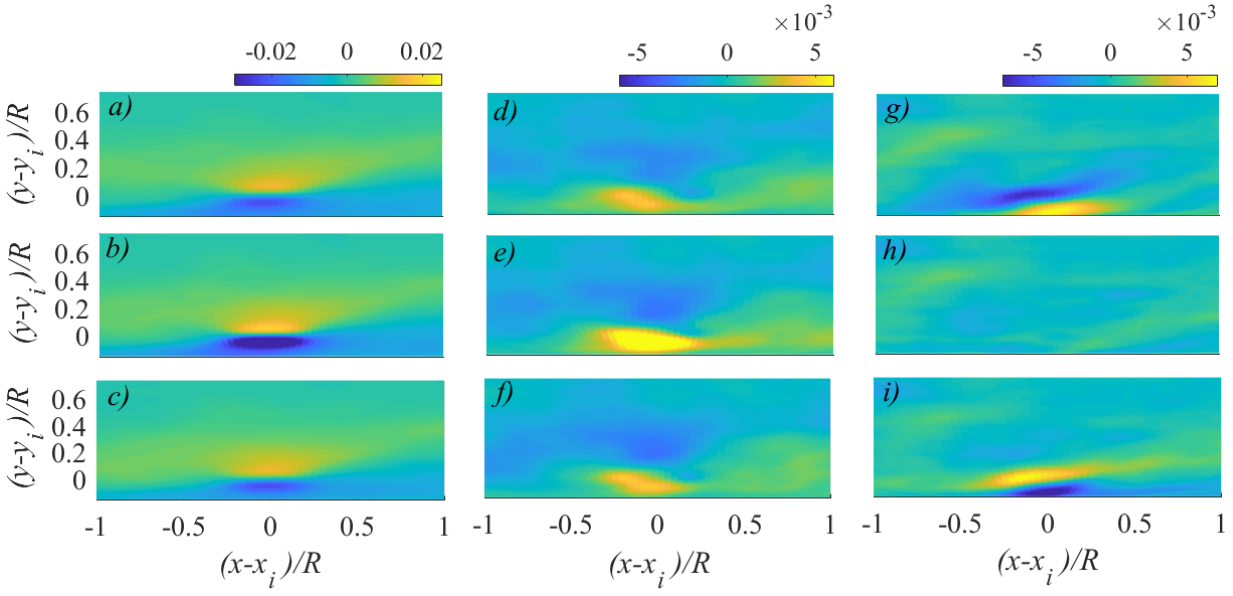

Figure 3.7: 2D cuts of the conditionally averaged fields around the shear layers at $(\theta - \theta_i)/2\pi = -0.012$ (*a, d, g*), 0 (*b, e, h*) and 0.012 (*c, f, i*). (*a, b, c*) corresponds to the streamwise velocity fluctuations, $< u'/U_{cl} >$; (*d, e, f*) corresponds to the wall-normal velocity fluctuations, $< v'/U_{cl} >$; and (*g, h, i*) corresponds to the spanwise velocity fluctuations, $< w'/U_{cl} >$.

Furthermore, Figure 3.5 (*a*) and (*b*) shows iso-surfaces of the streamwise and wall-normal velocity fluctuations and swirling strength for the mean flow field conditioned on the wall-normal centres of the internal shear layers between $y/R = 0.15 - 0.2$. Here, for each cross-section of a detected shear layer in the spanwise-wall normal plane, the shear layer was further divided into sections at each spanwise location. Finally, for each section of the shear layer the wall-normal centre was determined. While y_i corresponds to the wall normal centre of each final cross-section, x_i and θ_i indicates the streamwise and azimuthal positions of the these cross sections, respectively. Hence, the flow field was remapped with respect to y_i, x_i and θ_i for each cross-section of a shear layer. Here, local conditional mean streamwise velocities were used to reconstruct the streamwise extent. As can be seen in the resulting 3D figures, below $(y - y_i = 0)$ there is a strong low speed region extended in the streamwise direction, which is surrounded by two distinguished swirling motions having opposite signs. Also, this low speed region can be seen to be associated with strong positive wall normal-velocity fluctuations, which would indicate a region dominated by ejection events. These findings are consistent with the conceptual picture of Adrian *et al.* [1], and support the connection between the shear layers and the hairpin structures.

In addition to Figure 3.5, in Figure 3.6, a 2D cross section of some averaged flow fields at $(x - x_i = 0)$ is provided in the spanwise-wall normal plane for all components of the velocity fluctuations as well as swirling strength and Reynolds shear stress. All the above findings in Figure 3.5 can be more clearly seen in these 2D cross-sections. Furthermore, from the spanwise component of the averaged velocity fluctuations (Figure 3.6 (c)) as well

as the averaged vector field shown by the arrows and the swirling motions (Figure 3.6 (d) & (f)), it can be seen that the shear layers are strongly stretched in the spanwise direction. This is probably the reason why the layers are thin in the wall-normal direction. Moreover, from the 2D cuts at $(\theta - \theta_i)/2\pi = -0.012$, 0 and 0.012 in the wall normal-streamwise planes as shown in Figure 3.7, the spanwise and the wall normal components of these secondary motions are seen to be quite extended ($\sim 0.5R$) in the streamwise direction similar to the low-speed region, having angles of about $\sim +12^\circ$ and -12°, respectively. For brevity, results for the swirling strength in the wall normal-streamwise planes are not shown here, but swirling motions were observed to have similar angles ($\sim 10^\circ$) as well (at $(\theta - \theta_i)/2\pi = -0.012$ and 0.012).

3.3.2 SHEAR LAYERS IN THE SPANWISE-WALL NORMAL PLANE

Previously mentioned studies examined the shear structures or the continuous interfaces of the UMZs in the streamwise-wall normal plane only, either in a TBL or turbulent channel flow (TCF). In this section, we continue the study in the previous section by providing a comprehensive analysis on the properties of the shear layers in the wall normal-spanwise plane of a turbulent pipe flow.

We begin the analysis by conditionally averaging some flow properties across the shear layers in the spanwise direction. The shear layers were first divided into spanwise-wall normal cross-sections at each streamwise location similar to the previous section. Then, each cross-section was further considered as a combination of sections at each wall-normal position, having a certain wall thickness determined by the vector spacing but varying spanwise length. Afterwards, with respect to its wall position, each section was grouped from the near wall, $y = 0.1R$, to the core, $y = 1R$, of the pipe in bins with an equal increment of $0.1R$. Finally, relative to the spanwise centre of each determined section, the conditional analysis were performed to find out if there is any change in the flow properties across the detected shear layers along the spanwise direction. The resulting average profiles for the streamwise velocity, $< u >$, and the dissipation rate, $< \varepsilon >$ are shown in Figure 3.8. The profiles in (a) and (c) are normalised by U_{cl} and U_{cl}^3/R, respectively, whereas the profiles in (b) and (d) are normalised by the local conditional mean values of $< u >_y$ and $< \varepsilon >_y$, respectively, found in (a, c) away from the effect of the layers. From Figure 3.8 (a, b), it can be seen that these structures are associated with low streamwise velocity in the azimuthal direction. The effect of the shear layers is stronger near the wall and weaker towards the core of the pipe. Figure 3.8 (c, d), on the other hand, shows that these layers are highly dissipative regions where a significant peak in the dissipation occurs. Additionally, Figure 3.8 (d) shows that when the profiles are normalised by the local mean dissipation rates away from the location of the shear layers, similar peaks (in terms of the magnitude) in the dissipation rates result at each wall normal location. It should be noted here that since the dissipation rate was not fully resolved (45% near the core of the pipe), the unresolved dis-

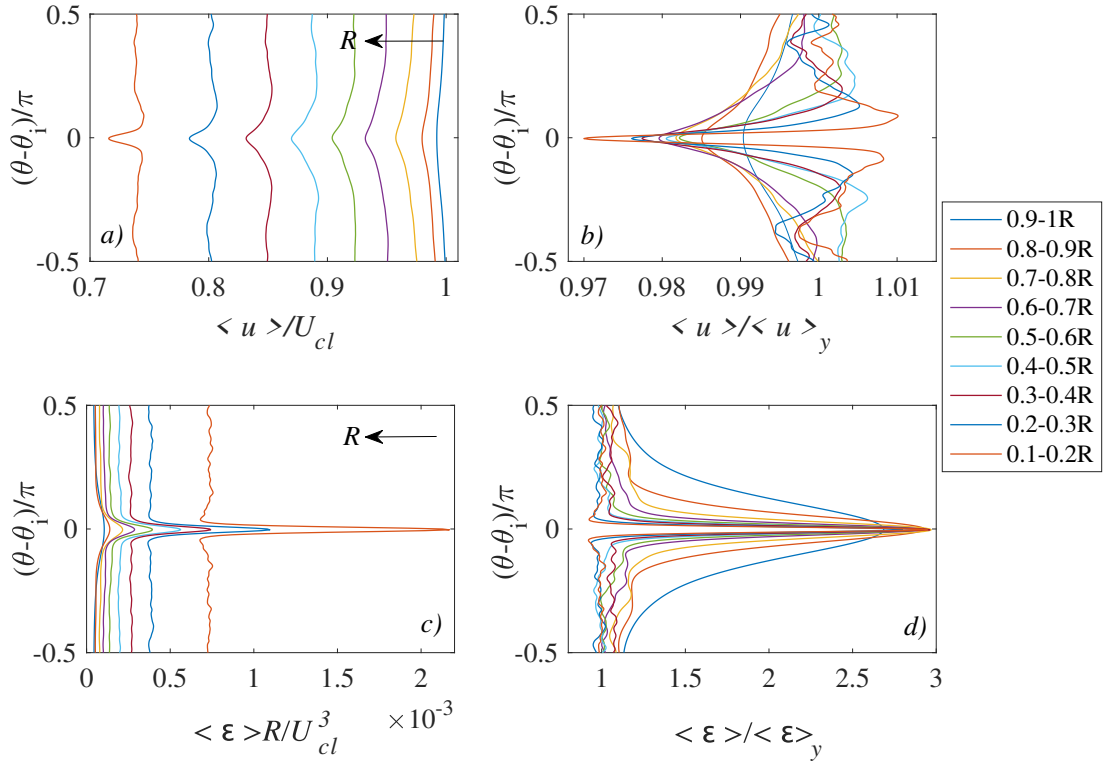

Figure 3.8: Conditionally sampled streamwise velocity, u, (*a, b*) and dissipation, ε, (*c, d*) profiles in the spanwise direction, θ. The spanwise centre of each cross section of the detected shear region is represented by θ_i, while $(\theta - \theta_i)$ represents the distance from the centre of the cross section of the layers in the spanwise direction. Shear layers are grouped according to the location of their spanwise centre (for each cross section) in the pipe, from $0.1R$ to $1R$ with a constant increment of $0.1R$. The arrows show the direction of the wall.

sipation was estimated by the large eddy (Smagorinsky) model (Sheng *et al.* [109], Sharp & Adrian [107], Tokgoz *et al.* [118]).

To check the effect of the shear layers on the average flow structures, two point correlations for the gradient of the streamwise velocity, $R(u_y u_y)$, and the streamwise velocity fluctuations, $R(u'u')$, were computed. $R(u_y u_y)$ can also provide information about the wall normal and spanwise width of the shear layers in an average sense. Here, in addition to correlations conditioned on the wall normal centres (see §3.3.1) of the shear layers (*e.g.* eqn. 3.2), general correlations (*e.g.* eqn. 3.3) conditioned on wall normal locations irrespective of whether a shear layer is detected or not were also determined for comparison. For the latter, the wall normal locations, y_{ref}, correspond to the centre of each bin that the detected shear layers are grouped into. The subscripts s and ref in eqn. 3.2 and eqn. 3.3 corresponds to the properties related to the detected shear layers and reference wall locations, respectively. The overbars, on the other hand, represent conditional averaging over θ and x.

The left column (*a, c, e, g*) in Figure 3.9 and Figure 3.12 represents the two point correlations conditioned on the wall normal centre of the shear layers, while the right columns (*b, d, f, h*) correspond to the general correlations conditioned on wall normal locations. The correlation functions in Figure 3.9 (*b, d, f, h*) show that for each wall normal location similar structures are obtained for $R(u_y u_{y,ref})$, and that the correlation peak is more elongated in the azimuthal direction towards the core region (as also observed in Figure 3.8). For the two point correlation coefficients conditioned on the wall normal centre of the shear layers, $R(u_y u_{y,s})$ (Figure 3.9 (*a, c, e, g*)), it can be seen that the correlation peaks are more elongated in the angular direction as well as their cores are wider in the wall normal direction as compared to their counterparts in Figure 3.9 (*b, d, f, h*).

$$R(u'u'_s) = \frac{\overline{u'(y_s, z)\, u'(y, z + r_z)}}{u_{rms}(y_s)\, u_{rms}(y)} \tag{3.2}$$

$$R(u'u'_{ref}) = \frac{\overline{u'(y_{ref}, z)\, u'(y, z + r_z)}}{u_{rms}(y_{ref})\, u_{rms}(y)} \tag{3.3}$$

The wall normal thickness and the spanwise length of these two-point correlations were further quantified based on the peak width at $R(u_y u_y) = 0.8$. This threshold is relatively high to ensure converged results at each wall normal location. The wall normal thickness of the correlation is determined at the spanwise center of the correlation, *i.e.* $(\theta - \theta_i = 0)$ (see Figure 3.10 (*a, b*)), while the spanwise length is determined at the wall normal center of the correlation coefficient $(y - y_i = 0)$ (see Figure 3.10 (*c, d*)). Here, θ_i and y_i represent the azimuthal (in terms of angles) and wall normal location of the detected shear.

The resulting width and the spanwise length of the two-point correlations are presented in Figure 3.11 (*a*) and (*b*), respectively, for several wall normal locations and for all Reynolds numbers. Full lines with open symbols correspond to the data conditioned on the wall normal center of the shear layers, while the dashed lines with filled symbols represent the results for general conditioning on wall normal location. When the general conditioning is compared to those for conditioning on the shear layers, a significant increase in the wall normall thickness ($\sim 40\%$) and the spanwise length ($\sim 50\%$) of the correlation coefficient is observed for the case of the shear layers (see also Figure 3.17 (*b*, *c*)). On the other hand, although the presence of the shear layers significantly affects the size of the correlation peaks, the trends with wall normal distance are quite similar. For both conditions, the wall normal width of the correlations are proportional to the Reynolds number until the wall normal position of $y/R \approx 0.6$. Beyond that position, the behaviour reverses. Similar behaviour is observed for the spanwise length of the correlation coefficients below the same wall normal position, *i.e.* $y/R \approx 0.6$, such that the spanwise length is proportional to the Reynolds number. Beyond this wall normal location, the spanwise length appears independent of the Reynolds number.

The effect of the shear layer structures is also visible in the two-point correlations of the streamwise velocity fluctuations, $R(u'u')$, (Figure 3.12). When the correlation coefficients

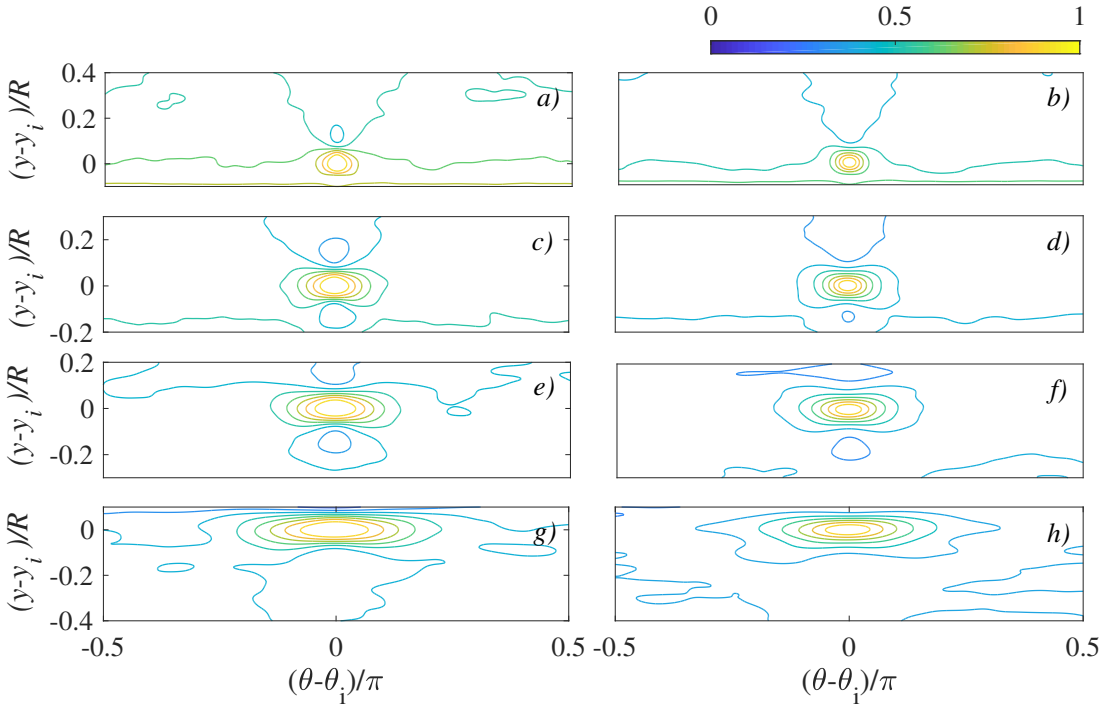

Figure 3.9: Iso-contours of two point correlation coefficient for the gradient of the streamwise velocity conditioned on the shear layer centre for different wall normal locations, $R(u_y u_{y,s})$, (*a, c, e, g*); and general correlation conditioned at a wall-normal location, $R(u_y u_{y,ref})$, (*b, d, f, h*). The shear layers are binned according to the distance of their core from the wall, $y/R = 0.1 - 0.2$ (*a*), $0.3 - 0.4$ (*c*), $0.5 - 0.6$ (*e*), $0.7 - 0.8$ (*g*). The reference points correspond to $y/R = 0.15$ (*b*), 0.35 (*d*), 0.55 (*f*), 0.75 (*h*).

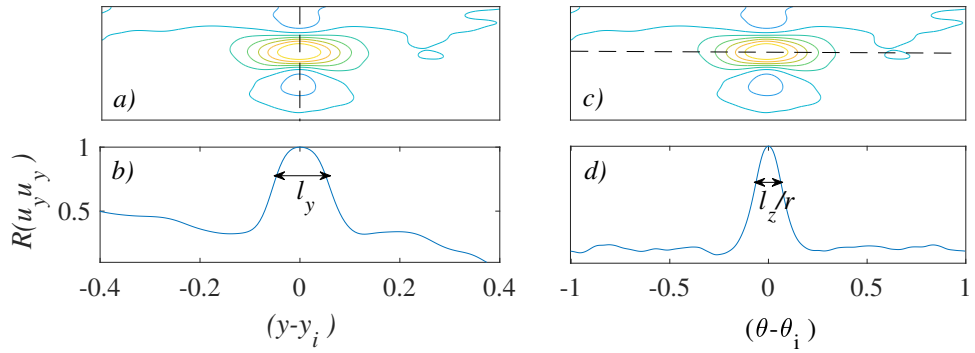

Figure 3.10: Sketch illustrating how the wall normal thickness, l_y, (*a*, *b*) and the spanwise length, l_z, (*c*, *d*) of the correlation coefficients are determined using the peak width at $R(u_y u_y) = 0.8$. Dashed lines on the correlation contours indicate the spanwise and the wall normal centers of the shear layers where $R(u_y u_y)$ in (*a*) and (*b*), respectively, corresponds to. *r* indicates the distance of the centre of the averaged shear layers from the core of the pipe.

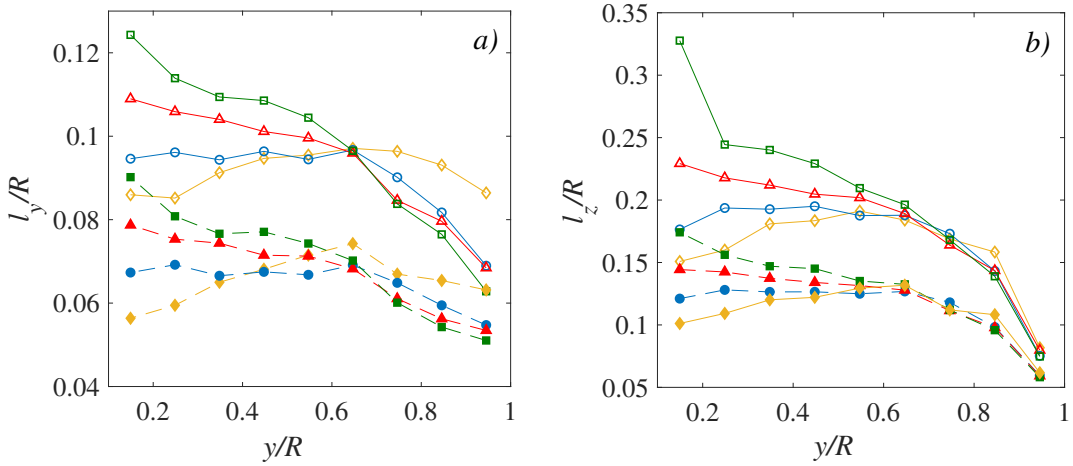

Figure 3.11: Wall normal thickness, l_y, (a) and the spanwise length, l_z, (b) as determined from the peak (see Figure 3.10). Full lines with open symbols are for the correlation conditioned on the wall normal centre of the shear layers, and dashed lines with filled symbols are for the general correlation at reference wall locations. Yellow (diamond), blue (circle), red (triangle) and green (square) correspond to the flow conditions at $Re_\tau = 340$, 752, 999 and 1259, respectively.

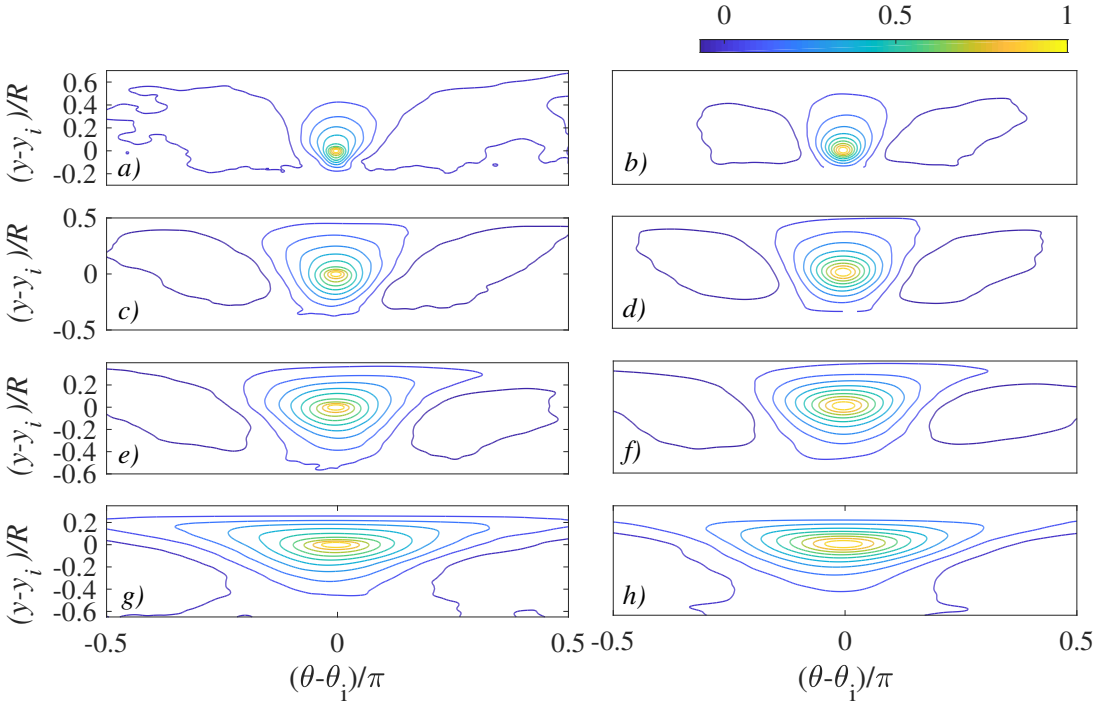

Figure 3.12: Iso-contours of two point correlation coefficient for the streamwise velocity fluctuations conditioned on the shear layer centre for different wall normal locations, $R(u'u'_s)$, (a, c, e, g); and general correlation conditioned at a wall-normal location, $R(u'u'_{ref})$, (b, d, f, h). The shear layers are binned according to the distance of their core from the wall, $y/R = 0.1 - 0.2$ (a), $0.3 - 0.4$ (c), $0.5 - 0.6$ (e), $0.7 - 0.8$ (g). The reference points correspond to $y/R = 0.15$ (b), 0.35 (d), 0.55 (f), 0.75 (h).

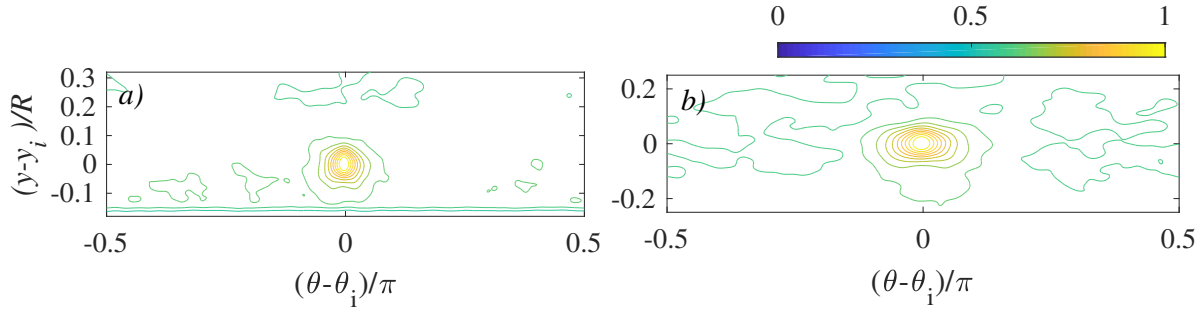

Figure 3.13: Iso-contours of two point correlation coefficient for the shear values, $[A]$, conditioned on the shear layer centre for two different wall normal locations, $y/R = 0.2-0.3$ (a) and $y/R = 0.5-0.6$ (b).

in Figure 3.12 (a, c, e, g) are compared with those in (b, d, f, h), it can be seen that the presence of the shear structures are decreasing the width of the core of the correlation coefficient. Similarly, the spanwise length scale determined from the correlation coefficient around the shear centre decreases. Apart from the peak widths, the overall structure of the correlation coeffcients in the wall normal-spanwise plane is quite similar for both conditions at each wall normal location.

As a final note in this section, the spanwise shape of the shear layers was also investigated through the two point correlations for $[A]$. However, as can be seen in Figure 3.13, similar results were obtained as for the correlations for the streamwise velocity gradients.

3.3.3 SHEAR LAYERS IN THE STREAMWISE-WALL NORMAL PLANE

In this section, the shear layers are examined in the streamwise-wall normal plane. First, the detected shear layers were grouped according to their wall normal center as in §3.3.1, and then conditional sampling was performed to analyse these structures in wall normal-streamwise planes. The conditionally averaged profiles for the streamwise velocity, $< u >$, wall normal velocity $< v >$, turbulent shear stress, $< -u'v' >$ and dissipation rate, $< \varepsilon >$, at $(x - x_i = 0)$ are shown in Figure 3.14. From the streamwise velocity (a) and dissipation rate (b) profiles, a significant increase across the averaged layers is observed at each wall-normal location, the magnitude of which is deceasing towards the core of the pipe. For the wall normal (c) and turbulent shear stress profiles (d), on the other hand, it can be seen that there occurs a significant decrease in the magnitude across the sampled layers.

The jumps in the streamwise velocities are further quantified (similar to Chauhan *et al.* [22], see Figure 3.15a) for each Re_τ, and for each wall-normal bin (Figure 3.15). Both single set and three set results for $Re_\tau = 752$ are nearly identical, which implies that the results appear to be converged. Furthermore, it can be seen that the jumps in the streamwise velocity are of the same order of magnitude for all the Reynolds numbers, that is between $10 - 17\%$ of the centreline velocity near the wall and decreasing towards the core of the pipe. However, it seems that these velocity jumps decrease in magnitude with Reynolds

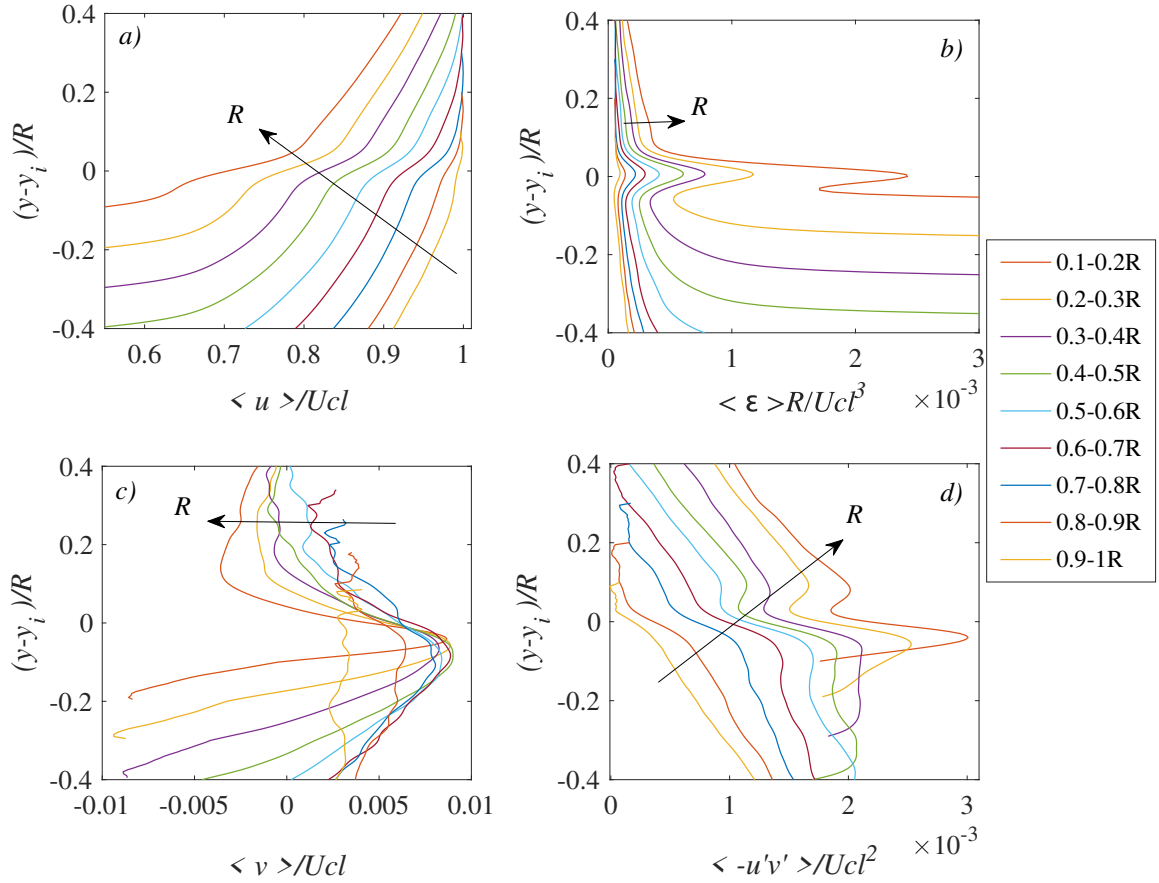

Figure 3.14: Conditionally sampled streamwise velocity, $< u >$, (a); dissipation, $< \varepsilon >$, (b); wall normal velocity, $< v >$, (c); and turbulent shear stress, $< -u'v' >$, (d) profiles. The centre of the shear region is represented by y_i, while $(y - y_i)$ represents the distance from the centre of the layers in the wall normal direction. Shear layers are grouped according to the location of their centres in the pipe, from $0.1R$ to $1R$ with a constant increment of $0.1R$. The arrow shows the direction of the wall (from $1R$ to $0.1R$).

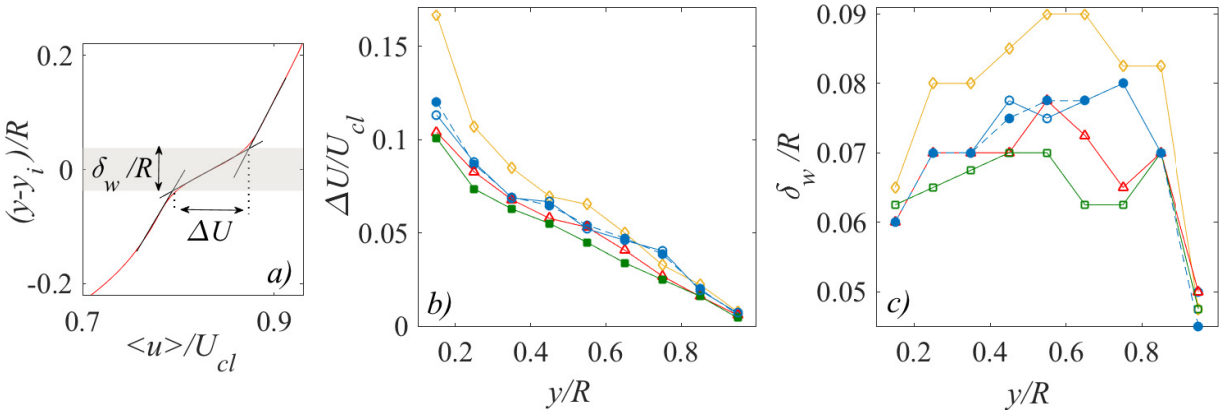

Figure 3.15: (*a*) Jumps in the streamwise velocity profiles at several wall location, ΔU, which are normalised by U_{cl}. (*b*) Thickness of the shear layers at the same wall normal locations. Yellow (diamond), blue (circle), red (triangle) and green (square) colors correspond to the flow conditions at *i.e.* $Re_\tau = 340$, 752, 999 and 1259, respectively. Additionally, filled circles correspond to data with three independent sets for $Re_\tau = 752$.

number. Based on the conditional streamwise velocity profiles (Figure 3.14 (*a*)), the thickness of the layers is also determined (Figure 3.15 (*c*)). It can be seen that the thickness of the layers is between $0.045 - 0.09R$.

Similar to the previous section, two-point correlations for the gradients of the streamwise velocity were performed in wall normal-streamwise planes to determine the effect of the shear structures on the streamwise width of the correlation coefficient peaks. Figure 3.16 (*a, c, e, g*) shows the correlations conditioned on the detected shear layers, while (*b, d, f, h*) correspond to the general correlations at the same wall normal reference positions. Similar to the thickness and the spanwise length of the correlation peaks, a significant increase in the streamwise length of the correlation coefficients are visible for the former case. When the length scale determined from the width of the correlation peaks based on $R(u_y u_y) = 0.8$ is compared for all Re_τ (Figure 3.17 (*a*)), it can be seen that the increase is around 40% (Figure 3.17 (*d*)). Moreover, the correlations for the streamwise velocity fluctuations (Figure 3.18) show that the presence of a shear layer (*a, c, e, g*) decreases the extent of the highly correlated regions in the wall normal-streamwise planes compared to the correlations with the reference wall normal locations (*b, d, f, h*). Also, it is seen that the shear layers are affecting the correlations across the plane, which was observed to be quite local in the wall normal-spanwise plane (Figure 3.12). On the other hand, still, similar types of average structures are obtained from these correlation coefficients for each condition in the streamwise-wall normal plane.

Furthermore, the streamwise shape of the shear layers was investigated through two point correlations for $\left[A\right]$ (Figure 3.19). However, similar results were obtained as for the correlations of the streamwise velocity gradients.

Finally, in this section, conditional cross correlations were evaluated for the streamwise velocity fluctuations, $R_{u'}(y - y_i\,; y' - y_i)$, between certain wall-normal distances from the

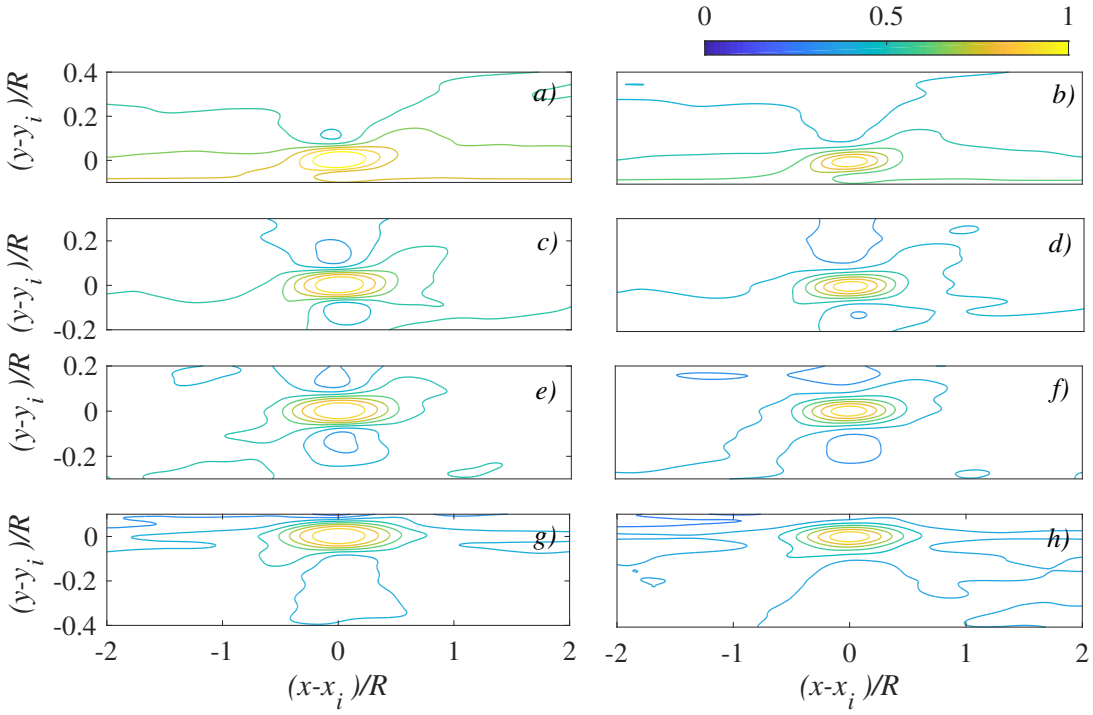

Figure 3.16: Iso-contours of two point correlation coefficient for the gradients of the streamwise velocity conditioned on the wall normal centre, $(y - y_i = 0)$, of the shear layers at each streamwise position, $R(u_y u_{y,s})$, $(a,\ c,\ e,\ g)$; conditioned on reference points, $R(u_y u_{y,ref})$, $(b,\ d,\ f,\ h)$. The shear layers are binned according to the distance of their core from the wall, $y/R = 0.1 - 0.2$ (a), $0.3 - 0.4$ (c), $0.5 - 0.6$ (e), $0.7 - 0.8$ (g). The reference points correspond to $y/R = 0.15$ (b), 0.35 (d), 0.55 (f), 0.75 (h).

centre of the detected shear layers, $(y' - y_i)$, and all other wall locations (at the same spanwise and streamwise position), which are positioned according to the centres of the layers, $(y - y_i)$. For brevity, results only for $Re_\tau = 752$ (a) and $Re_\tau = 1259$ (b), and for the shear layers between $y/R = 0.5{-}0.6$ are shown in Figure 3.20. As can be seen from this figure, a significant decrease in the correlations across the layers occurs, which shows the blockage effect of the internal shear layers. Similar results were reported before by Ishihara *et al.* [62] for turbulent/non-turbulent interfaces (TNTI) in their direct numerical simulations of a turbulent boundary layer.

3.4 CONCLUSIONS

In this chapter, a comprehensive analysis was presented on the properties of the internal shear layers in a turbulent pipe flow. The experimental datasets used were acquired with time-resolved stereoscopic PIV in the cross section of the pipe for four different Reynolds numbers, $Re_\tau = 340$, 752, 999 and 1259. For each flow condition, the shear layers were detected using the method of Houriti & Kawaga [54], which enabled us to investigate the 3D features of these structures.

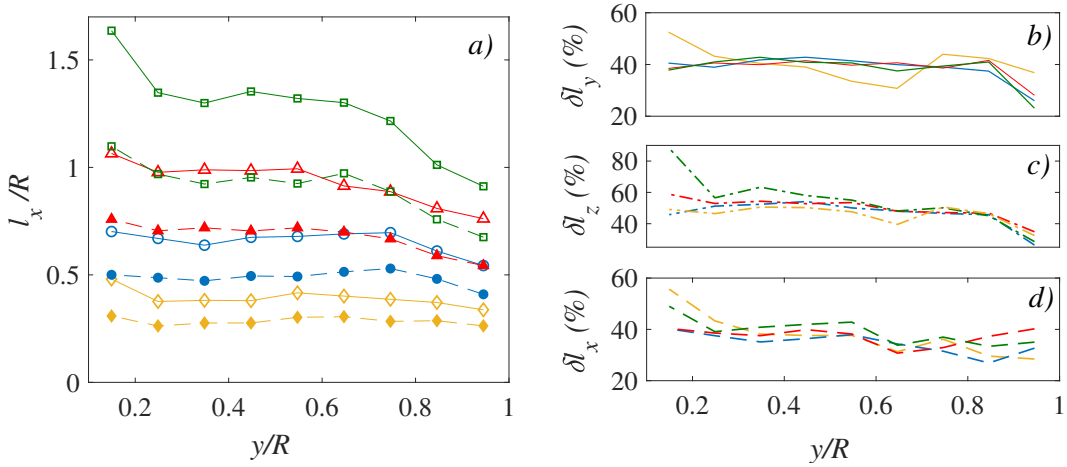

Figure 3.17: (*a*) Streamwise length, l_x, of the peak of the correlation coefficients. Full lines with open symbols are for the correlation conditioned on the wall normal centre of the shear layers, and dashed lines with filled symbols are for the general correlation at reference wall locations. (*b*), (*c*) and (*d*) shows percentage increase in the width of the correlation peaks with the presence of the shear layers in the wall normal, spanwise and streamwise directions, respectively.

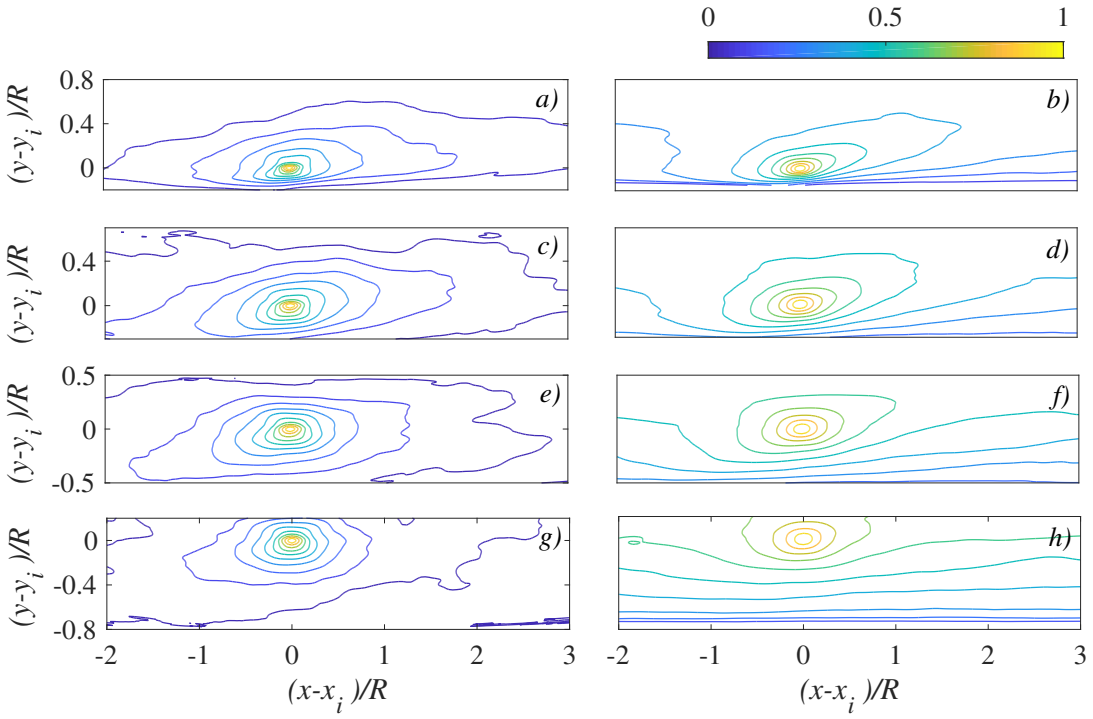

Figure 3.18: Iso- contours of two point correlation function for the streamwise velocity fluctuations conditioned on the wall normal centre, $(y - y_i = 0)$, of the shear layers at each streamwise position, $R(u'u'_s)$, (*a, c, e, g*); conditioned on reference points, $R(u'u'_{ref})$, (*b, d, f, h*). The shear layers are binned according to the distance of their core from the wall, $y/R = 0.1 - 0.2$ (*a*), $0.3 - 0.4$ (*c*), $0.5 - 0.6$ (*e*), $0.7 - 0.8$ (*g*). The reference points correspond to $y/R = 0.15$ (*b*), 0.35 (*d*), 0.55 (*f*), 0.75 (*h*).

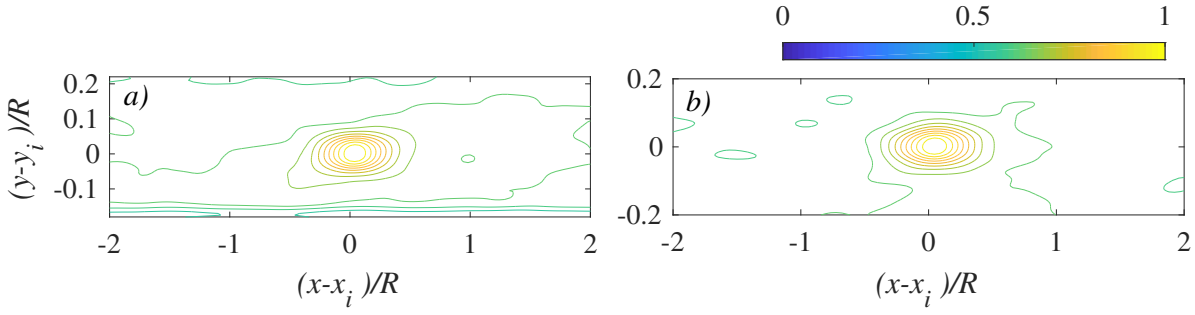

Figure 3.19: Iso-contours of two point correlation coefficient for the shear values, $[A]$, conditioned on the shear layer centre for two different wall normal locations, $y/R = 0.2-0.3$ (a) and $y/R = 0.5-0.6$ (b).

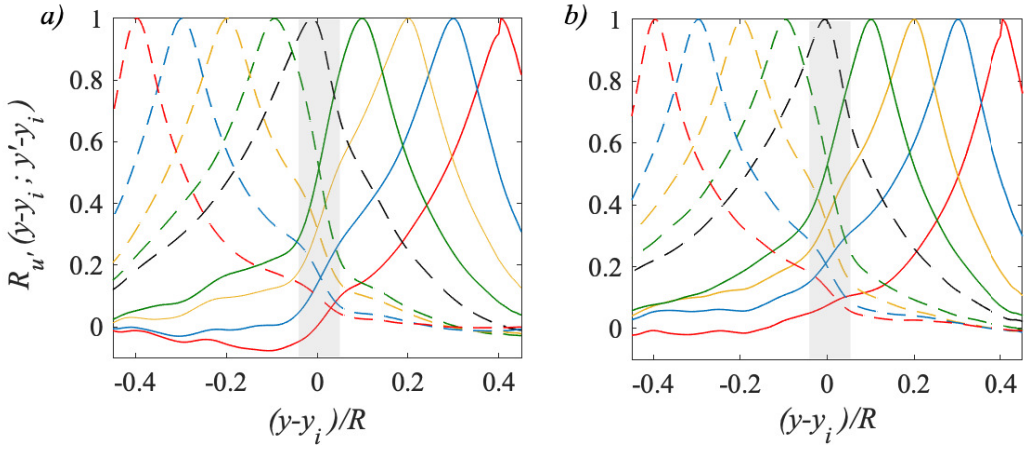

Figure 3.20: Conditional cross correlations, $R_{u'}(y - y_i\,; y' - y_i)$ between certain wall normal distances from the centre of the detected shear layers, $(y' - y_i)$, and all other wall locations which are positioned relative to the centre of the layers, $(y - y_i)$. Results are for the shear layers whose centre is between the wall locations $y/R = 0.5-0.6$, and for the Reynolds number $Re_\tau = 752$ (a) and $Re_\tau = 1259$ (b). Here, $(y' - y_i) \approx -0.4, -0.3, -0.2, -0.1$ and -0.01 (dashed lines) which are below the centre of the layers; and $(y' - y_i) \approx 0.4, 0.3, 0.2$ and 0.1 (solid lines) which are above the centre of the layers. Gray contours show the approximate thickness of the shear layers.

Visual examples of the shear layers together with the corresponding instantaneous velocity fields showed clearly observable regions of similar streamwise velocities bounded by the detected shear layers both in the spanwise-wall normal and streamwise-wall normal planes. In particular, the core region of the pipe, which had relatively low turbulence, was seen to be bounded by the layers. Also, the shear layers were observed to be elongated in the streamwise directions ($\sim R$), and they appear arc-like in the cross-sectional planes.

Conditional mean flow around the shear layers revealed a strong low speed region beneath the average shear layers. This low momentum flow was associated with strong positive wall-normal velocity fluctuations, and surrounded by two oppositely rotating swirling motions. The shear layers, on the other hand, were observed to be stretched in the azimuthal direction by two oppositely signed secondary motions, keeping the layers thin in the wall-normal direction. These findings are consistent with the conceptual picture of Adrian *et al* [1] and support the relation between the shear layers and the hairpin structures.

Moreover, conditional averaging across the detected shear layers revealed significant jumps in the flow properties (*e.g.* turbulent shear stress, streamwise and wall normal velocities) occurring in the wall normal direction. In the azimuthal direction, on the other hand, these layers were observed to block the flow, causing a decrease in the streamwise velocity. In both direction, however, the analysis showed that these regions are highly dissipative. Even for the shear layers near the core of the pipe, a significant increase in the average dissipation rate occurs.

Further analysis on the shear layers was performed through two point spatial correlations to reveal if and how much they affect the surrounding flow in an average sense. The two point correlations were conditioned on the wall normal centre of the shear layers, where the shear layers were grouped into according to their wall normal centre. For comparison, general correlations (*i.e.* not conditioned on shear layers) were also evaluated for a given wall normal reference position. The resulting correlations revealed that the shear layers significantly affect the average size of the correlation coefficient peaks in all directions. Moreover, it was seen that the streamwise length of the structures are of the same order as the large scale motions, which support the argument that the shear layers are bounding the large scale motions having uniform velocities, *i.e.* UMZs. This argument will be further discussed in the next chapter. Furthermore, cross correlations were carried out for several reference points above and below the centre of the shear layers. The results revealed a significant decrease in the correlations across the layers, and the points below and above the layers are less correlated. This clearly shows the blockage effect of the internal shear layers similar to TNTIs.

4

UNIFORM MOMENTUM ZONES

4.1 INTRODUCTION

In Chapter 3, the properties of the internal shear layers identified using a 3D detection scheme were discussed in detail. The results revealed that these highly dissipative structures are elongated in both the streamwise and spanwise directions. Furthermore, the internal shear layers are bounded by large scale regions of nearly uniform velocities. This strongly suggest that the shear layers are the edges of the so-called uniform momentum zones (UMZs). Therefore, in this chapter, we detect and analyse the edges of the UMZs for later comparison with the internal shear layers.

The UMZs are basically large scale regions identified by employing the histogram approach of Adrian *et al.* [1] and de Silva *et al.* [111]. With this current work, we aim to provide a comparison between these two different detection methods for the shear layers in a statistically steady turbulent pipe flow. In previous studies (*e.g.* de Silva *et al.* [111], Kwon *et al.* [73], Laskari *et al.* [74]), the edges of the UMZs were analysed in wall normal-streamwise planes (and for 2D data only). Here the analysis is extended to other orientations of the plane, *i.e.* wall normal-streamwise versus wall normal-spanwise plane, when using the histogram method. Furthermore, with all the UMZ edges determined from the wall normal-streamwise planes at different azimuthal position across the pipe, the cross-stream connectivity of the UMZ edges can also be explored, which also allows assessing the consistency of the method.

For the analysis in the present chapter, the same datasets, as well as the same notations and the coordinate system are used, as in Chapters 2 and 3. This chapter is organised as follows: In the following section (§ 4.2), the UMZs and their edges are analysed over the wall normal-streamwise (§ 4.2.1) and wall normal-spanwise planes (§ 4.2.2), separately. Then, in Section 4.2.3, a visual and a quantitative comparison is given of the UMZ edges obtained using the histogram approach and the shear layers that were detected using a 3D detection method in Chapter 3. Finally, the findings are summarized in Section 4.3.

4.2 RESULTS AND DISCUSSION

4.2.1 UMZS IN THE WALL NORMAL-STREAMWISE PLANE

In this section, we use the streamwise-wall normal plane to plot the histogram of the streamwise velocities, and accordingly detect the continuous edges of the UMZs. The wall normal plane extends from $y = 0.05R$ to the core of the pipe ($y = R$). The streamwise extent of the plane, on the other hand, is limited to $\sim 2.2R$ (explained below) for each flow condition considered in this section. Since the data was acquired in the cross section of the pipe with time-resolved stereoscopic PIV, the streamwise length was reconstructed using Taylor hypothesis with the bulk velocity as the convection velocity. Following de Silva *et al.* [111], the location of a UMZ edge was approximated by the streamwise veloc-

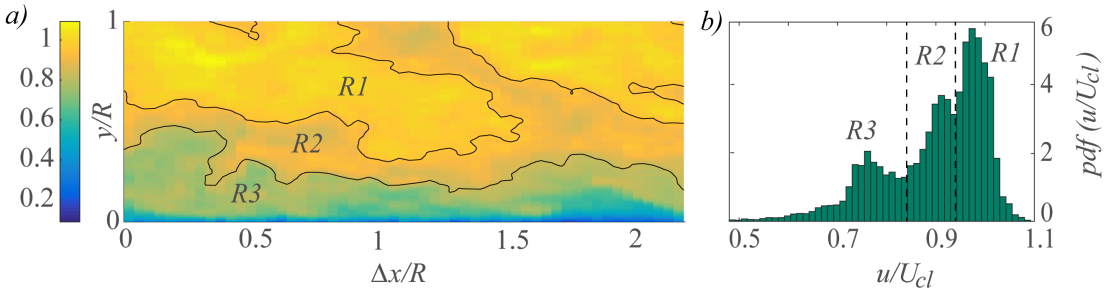

Figure 4.1: (*a*) Sample instantaneous field of the streamwise velocity, u, normalised by the central velocity of the pipe, U_{cl}, together with the detected UMZs and their edges on a wall normal-streamwise plane. (*b*) The corresponding histogram of the streamwise velocities over the plane shown in (*a*). *R1*, *R2* and *R3* show three different regions of similar velocities (UMZs), while the black continous lines in (*a*) correspond to the mid points between the peaks in the *pdf* as indicated by the dashed lines in (*b*).

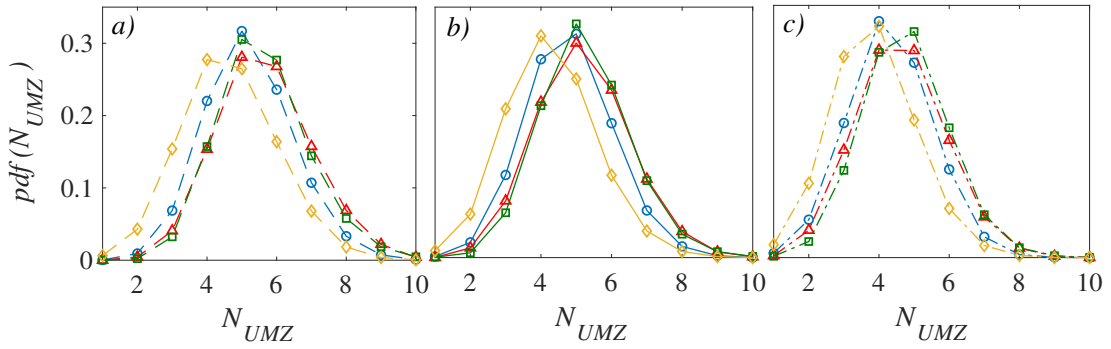

Figure 4.2: *Pdf* of the number of the detected UMZs over the wall normal-streamwise planes with *case A* (*a*), *case B* (*b*) and *case C* (*c*). Yellow (diamond), blue (circle), red (triangle) and green (square) correspond to the flow conditions at $Re_\tau = 340$, 752, 999 and 1259, respectively.

ity contour corresponding to the mid-point between the local peaks in the histogram of the streamwise velocities. Figure 4.1 (*a*) shows a sample field of the streamwise velocity together with the UMZ edges (black lines), and (*b*) shows the corresponding histogram of the streamwise velocities over this plane. The local peaks on the histogram correspond to the so-called modal velocities, and the locations of the UMZ edges in (*a*) were the mid point between these modal velocities. The regions demarcated by these edges, *i.e.* *R1, R2* and *R3*, are called UMZs, since within each region the magnitude of streamwise velocity is nearly constant. Note that the histogram of the streamwise velocities was not much affected by peak locking. Therefore, the raw data without any smoothing was used throughout this chapter.

In this section, all the streamwise velocities over each plane were distributed over 50 histogram bins, which corresponds to a bin size of $\sim 0.12 U_{cl}$ for all the cases considered. In addition, to correctly identify the modal velocities and accordingly the edges of the UMZs, the greater of the peaks that were separated by only a single histogram bin was

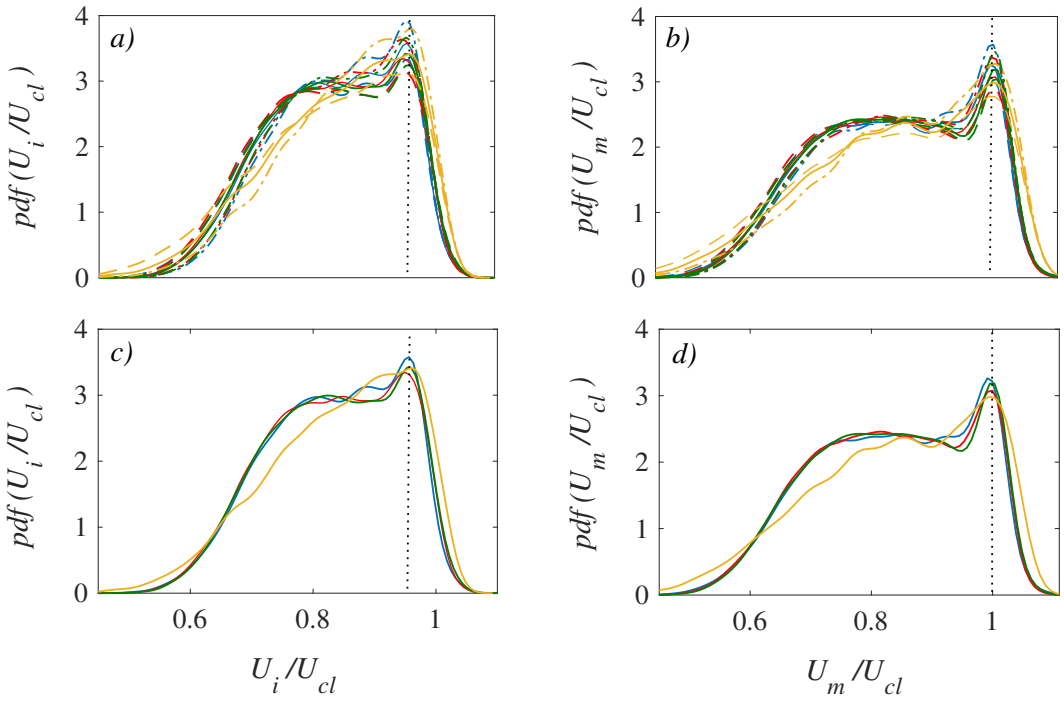

Figure 4.3: *Pdf* of the velocities corresponding to the location of the UMZ edges, U_i/U_{cl}, (*a, c*) and the *pdf* of the modal velocities, U_m/U_{cl}, (*b, d*). Dashed, full and dotted lines show the results for the *case A*, *case B* and *case C*, respectively. Results for the *case B* are shown separately in (*c, d*). Yellow, blue, red and green correspond to the flow conditions $Re = 340$, 752, 999 and 1259, respectively.

chosen as the peak, and the smaller one was ignored. Furthermore, peaks whose count was less than 0.5% of the total number of the data points in the considered plane were also ignored to avoid noisy peaks affecting the identification near the wall. It should also be noted here that the modal velocities are highly dependent on the number of histogram bins. If the number of bins increases, then more modal velocities and UMZ edges are identified. However, the locations of the detected UMZ edges become very close to each other, such that the distance between them becomes less than the thickness of the shear layers discussed in Chapter 3.

Another important parameter affecting the number and the location of the UMZ edges is the streamwise extent of the considered plane. If the streamwise length of the plane is very long then no separation between the regions of similar velocities occurs, since the histogram would average to its mean, which is resulting in a single peak. On the other hand, if the streamwise length is very short then the total number of data points in the plane is not enough to accurately define the UMZs and their edges. In this study, a streamwise length ($\sim 2.2R$) was chosen after conducting several analysis with different streamwise lengths, ranging between $1.2R$ and $2.5R$. The results revealed that, although the number density of the UMZ edges varied with the size of the streamwise distance, the overall statistics were observed to be almost identical over the ranges considered. Therefore, to have enough data points for each flow condition, a streamwise length $\sim 2.2R$ was employed. This length corresponds to $\Delta x^+ \approx 752$, 1682, 2208 and 2798 for $Re_\tau = 340$, 752, 999 and 1259, respectively.

In this section, the azimuthal continuity of the detected modal velocities was also used as an additional criterion on the peaks of the histogram plots. Compared to the base case (*case A*), where no azimuthal condition is applied, for *case B* only the peaks that also appeared at least on one of the neighbouring wall normal-streamwise planes are considered. The azimuthal spacing between two neighbouring planes is $0.01R$ (arc length) at the wall, which is much smaller than the thickness of the internal shear layers. For *case C*, on the other hand, the peaks on the histogram of the base plane were required to repeat on two other consecutive planes located azimuthally either before or after the current azimuthal position. Note that, throughout this chapter, unless otherwise stated, the results using the first azimuthal criterion (*case B*) are presented.

Figure 4.2 shows the resulting *pdf* of the number of the UMZs in a plane for each Reynolds number and also for the different azimuthal conditions (*cases A, B* and *C*, mentioned above). It can be seen that the distributions are not very sensitive to the azimuthal condition. Similar behaviour with respect to the azimuthal condition is also observed in the *pdfs* of the velocities corresponding to the identified UMZ edges, and of the modal velocities. From these plots it can also be seen that a significant number of the velocities corresponding to the UMZ edges appear around 95% of the central velocity of the pipe, U_{cl}, while the modal velocity *pdfs* peak at U_{cl}. Similar behaviour was also reported previously by Kwon *et al.* [73] for a turbulent channel flow using a similar histogram approach.

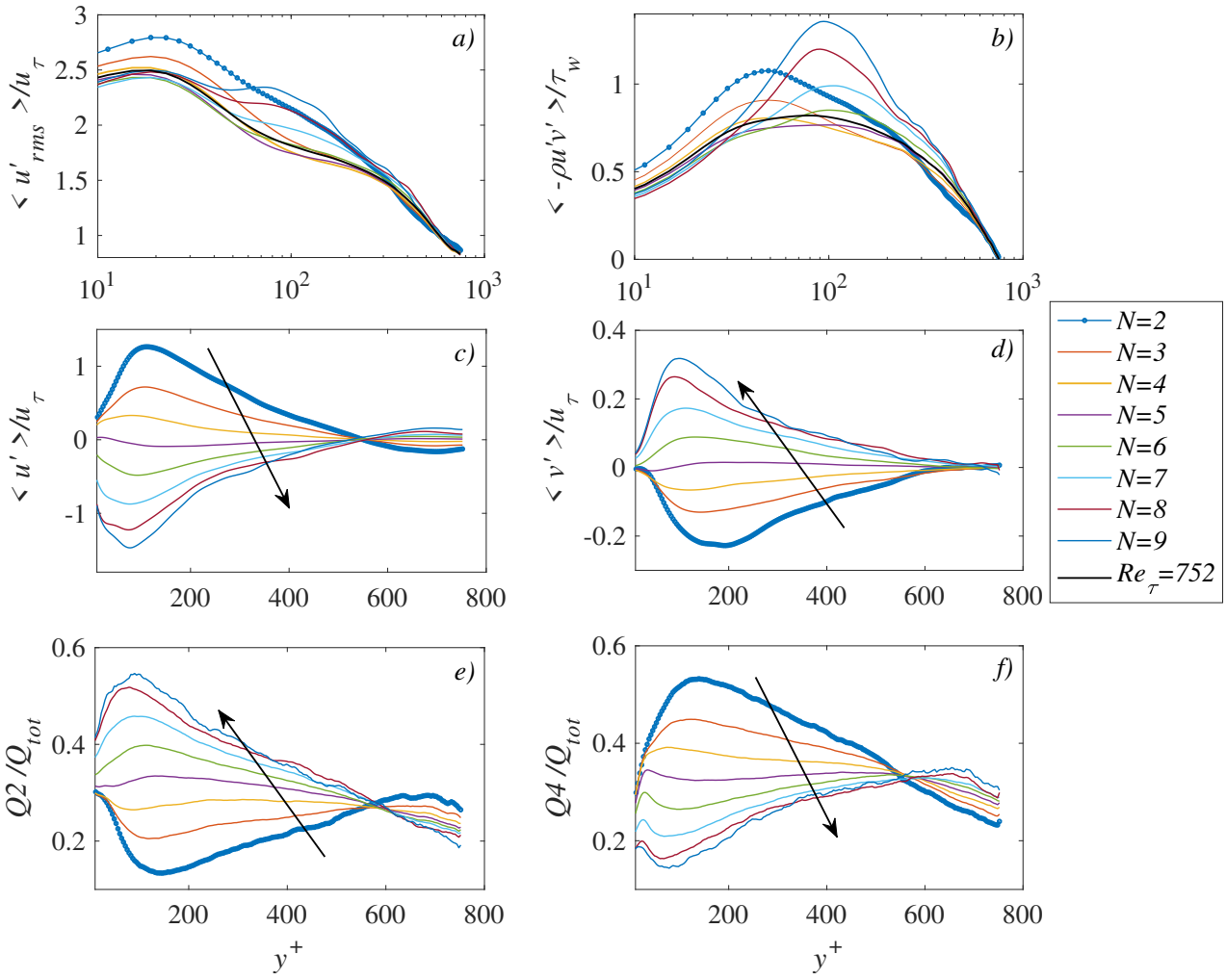

Figure 4.4: *Rms* of the streamwise velocity (*a*), turbulent shear stress (*b*), mean of the streamwise velocity fluctuation (*c*), mean of the wall normal velocity fluctuation (*d*), Q2 events (*e*) and Q4 events (*h*) that were conditioned on the number, N, of the UMZs for $Re_\tau = 752$. u_τ, τ_w and Q_{tot} are the wall friction velocity, wall friction and the total number of the quadrant events, respectively. Arrows show the direction of an increase in the number of the UMZs. Data show in black in (*a* and *b*) corresponds to the baseline profiles without any conditioning.

To investigate if there is any correlation between the number of the UMZs and the turbulence statistics, such as the *rms* of the streamwise velocity, turbulent shear stress, mean of the streamwise and wall normal velocity fluctuations and sweep ($u' > 0$, $v' < 0$, $Q4$) and ejection ($u' < 0$, $v' > 0$, $Q2$) events, further analysis was performed conditioning these profiles on the number of the detected UMZs in the plane (Figure 4.4). It can be seen that different behaviour for the profiles are observed with different number of the nearly uniform zones. For the *rms* and the turbulent shear stress profiles, it can be seen that for the number of zones (*i.e.* $N = 4, 5$ and 6) the statistics are similar to the unconditional results. For the higher numbers (*i.e.* $N = 7, 8$ and 9), a significant increase in the turbulence intensity, as well as the turbulent shear stress is observed within the logarithmic layer. Near the wall and the core of the pipe, however, these profiles are similar to the profiles for the cases where $N = 4, 5$ or 6. For the other two lowest numbers ($N = 2$ and 3), on the other hand, it can be seen that both the turbulence intensity and the turbulent shear stress values are higher than the unconditional cases in the inner wall cycle whereas they are approaching to the unconditional values near the core region. Furthermore, from the conditional mean of the streamwise and wall normal velocity fluctuations (*i.e.* u' and v') as well as the quadrant events ($Q2$ and $Q4$), it can be seen that a small number of zones (*i.e.* $N < 5$) is associated with positive streamwise and negative wall normal veloctity fluctuations, which results in sweep events, $Q4$. The higher (*i.e.* $N > 5$) number of the zones, on the other hand, is associated with negative streamwise and positive wall normal velocity fluctuations, that is ejection ($Q2$) events, as can be seen in Figure 4.4 (e and f). Similar relation between $Q2$ and $Q4$ events and number of the UMZs was recently reported by Laskari *et al.* [74] in a TBL. Note that, in Figure 4.4, only the profiles for $Re_\tau = 752$ are shown for brevity, since the results for the other flow conditions are similar.

Finally, in this section, the edge of the UMZs detected over the wall normal-streamwise planes at each of the azimuthal planes were projected onto the cross section of the pipe for each flow condition (Figure 4.5). It can be seen that for the lowest Reynolds number (*i.e.* $Re_\tau = 340$), the edge of the UMZs are coherent in the spanwise direction and separating the regions of similar velocities in the cross section of the pipe, in the same way as in the wall normal-streamwise planes where they were originally identified. The same applies to the results obtained at other Reynolds numbers. However, the continuity of the UMZ edges in the spanwise direction is not as clear as those for $Re_\tau = 340$. This is partly due to the noisy peaks in the histogram at higher Reynolds number, which could be a result of the decreased spatial resolution in the streamwise direction, hence, smaller amount of velocity points in a given area. In addition, the increased random behaviour of the flow with the Reynolds number is also an important factor effecting the histograms of the streamwise velocities.

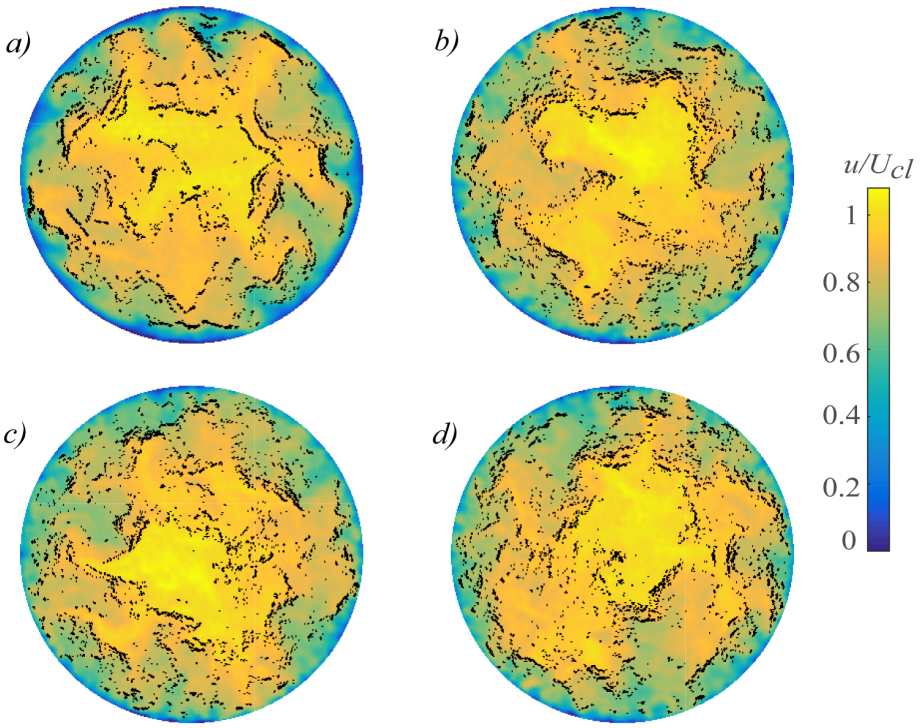

Figure 4.5: The projection of the edges of the UMZs, which were detected using the streamwise-wall normal plane, onto the wall normal-azimuthal plane (black regions) for the flow conditions $Re_\tau = 340$ (*a*), $Re_\tau = 752$ (*b*), $Re_\tau = 999$ (*c*) and $Re_\tau = 1259$ (*d*). Background colour shows the instantaneous streamwise velocity field normalised by the central velocity, U_{cl}.

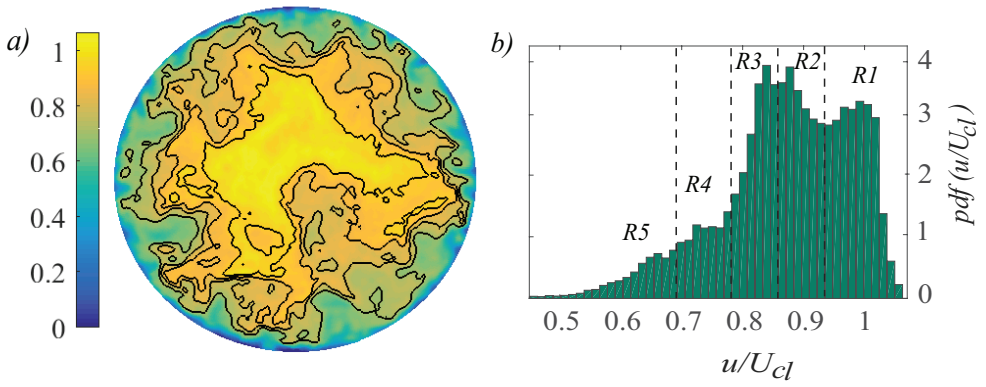

Figure 4.6: (*a*) Sample instantaneous field of the streamwise velocity, u, normalised by the central velocity of the pipe, U_{cl}, together with the detected edges of the UMZs (black contour lines) on a wall normal-spanwise plane. (*b*) The corresponding histogram of the streamvise velocities over the plane shown in (*a*). *R1*, *R2*, *R3*, *R4* and *R5* show five different regions of similar velocities (UMZs), while the black continous lines in (*a*) correspond to the location of the UMZ edges determined by the dashed lines in (*b*).

4.2.2 UMZS IN THE WALL NORMAL-SPANWISE PLANE

In this section, the UMZs and their edges were detected over the cross section of the pipe, which has not been reported before. In this case, the UMZs and their edges were detected using the histogram of the streamwise velocities in the spanwise-wall normal plane where the bin size was $\sim 0.12U_{cl}$. As before, the locations of the UMZ edges on that plane were identified by considering the mid point between the local peaks in the histogram (Figure 4.6). For the histogram peaks that were separated by a single bin, the greater one was selected as before (§ 4.2.1).

As can be seen in Figure 4.7 (*a*), similar distribution for the total number of the UMZs in the cross section is observed for all the considered flow conditions. These distributions are also consistent with those, except for $Re = 340$, presented in Figure 4.2 based on the detection in the streamwise wall-normal plane. Also, the *pdfs* of the velocities corresponding to the location of the UMZ edges are quite similar to those obtained in the streamwise wall-normal plane (compare Figure Figure 4.7 (*b*) and Figure 4.3 (*a, c*)). Again, the edge velocities are mostly appearing around $0.95U_{cl}$, bounding the relatively less turbulent core region of the pipe.

4.2.3 COMPARISON OF THE UMZ EDGES AND THE SHEAR LAYERS

In this part, the edges of the UMZs and the identified shear layers are compared (both visually and quantitatively). Figure 4.8 and 4.9 provide a visual comparison of the UMZ edges detected using different orientation of the planes and the shear layers. These figures present the results for $Re_\tau = 340$ and for $Re_\tau = 752$, respectively, to allow comparison

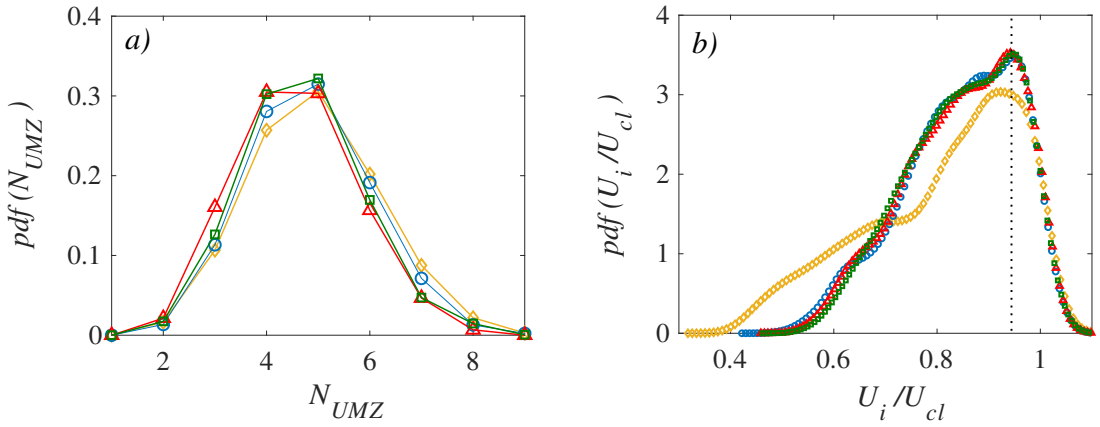

Figure 4.7: (*a*) *Pdf* of the number of the UMZs detected using the spanwise-wall normal planes. (*b*) *Pdf* of the instantaneous velocities corresponding to the location of the detected UMZ edges. Yellow (diamond), blue (circle), red (triangle) and green (square) symbols correspond to the flow conditions $Re_\tau = 340$, 752, 999 and 1259, respectively.

between two different Reynolds numbers. From the contour plots in Figure 4.8 (*b*) and 4.9 (*b*), it can be seen that the shear layers are appearing on the continuous edges of the UMZs which were detected using the cross section pdf (wall normal-spanwise plane). Although the shear layers are not fully connected in the azimuthal direction as are the UMZ edges, they have a significant azimuthal length. When the UMZ edges that were detected from wall normal-streamwise planes are compared with the shear layers (see Figure 4.8 (*c*) and 4.9 (*c*)), it can also be seen that they correspond mostly to the regions of intense shear. Furthermore, the azimuthal extent of the densely populated regions of the UMZ edges (magenta) can be seen to be comparable to the azimuthal length of the shear layers.

Based on the visualizations it appears that the shear layers coincide with the edges of the UMZs. This correspondence was quantified by considering the distance from the core of a shear region to the nearest edge of the UMZs (defined over the wall normal-streamwise plane). It was found that this distance is smaller than the thickness of the shear layers (Figure 4.10 (*a*)). When the locations of the core of the shear layers are compared with those of the UMZ edges defined over the cross section of the pipe, it can be seen that all the shear layers are residing very close proximity of the these UMZ edges; see Figure 4.10 (*b*). For the distance between the UMZ edges determined over the two different orientation of planes, it can be seen in Figure 4.10 (*c*) that the distance is greater than the previous two cases. These results show that the shear layers detected by the 3D method have a very good overlap with the UMZ edges detected by the histogram method. However, the reverse is not the case. This is obvious for the UMZ edges determined from the cross section of the pipe, since the shear layers are not continuous in the azimuthal direction. For the UMZ edges determined from the wall normal-streamwise planes, these UMZ edges do not always correspond to a detected shear layer. It should also be noted in this section that the results are quite similar over the range of the Reynolds numbers considered.

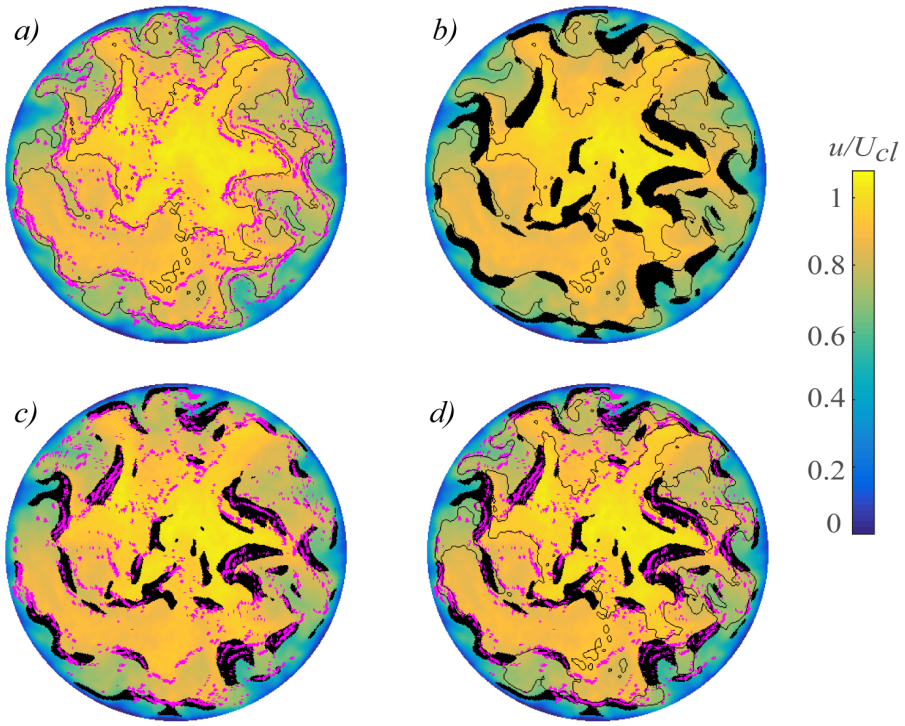

Figure 4.8: Comparison of the shear layers detected using the 3D method (black regions), edges of the UMZs defined using the wall normal-spanwise planes (black contour lines) and the projection of the UMZ edges identified over the wall normal-streamwise planes (magenta regions). (*a, b, c*) and (*d*) show different combinations of the UMZ edges and the shear layers for better comparison. Results correspond to the flow contion at Re = 340, and backgound colormap shows the instantaneous streamwise velocity normalised by U_{cl}.

Finally, when the *pdf* of the number of the UMZs that were determined based on the occurrence of the shear layers at each spanwise and streamwise location (Figure 4.10 (*d*)) are compared with those in Figure 4.2 and Figure 4.7 (*a*), a very similar distribution was found. These results also suggest that the distribution for the number of the UMZs does not change with Reynolds number in a turbulent pipe flow; at least within the range of the Reynolds number considered in this study, no significant variation was found.

4.3 CONCLUSIONS

Following the work in Chapter 3, where a comprehensive analysis on the internal shear layers which were defined using a 3D detection method was provided, in the present chapter, UMZs and their edges were investigated using the histogram approach.

The histogram approach has been frequently employed in the literature, however, the analysis has been limited to the wall normal-streamwise planes at a certain spanwise po-

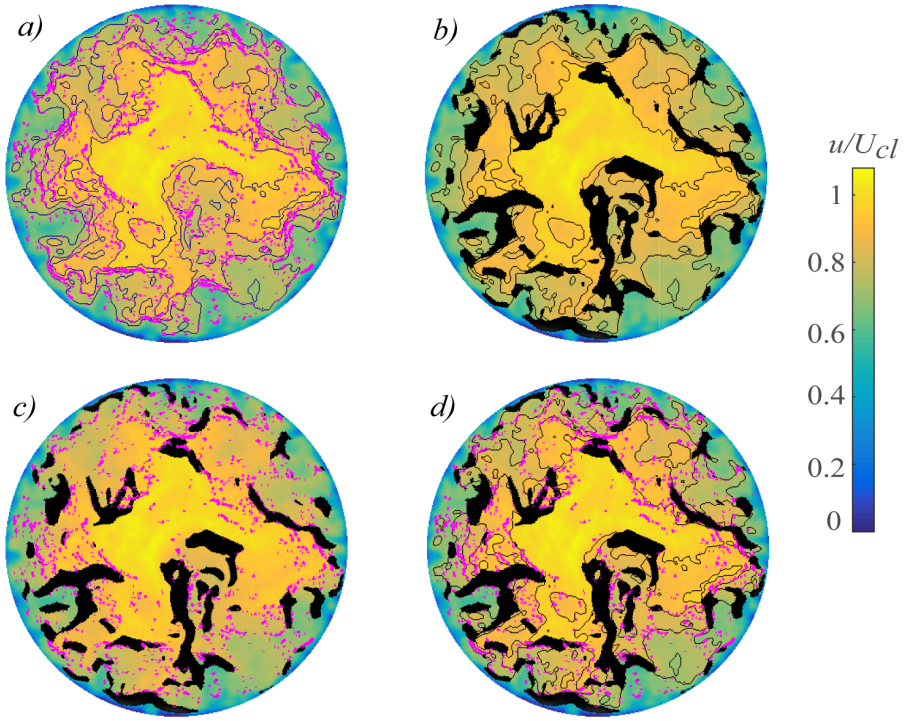

Figure 4.9: Comparison of the shear layers detected using the 3D method (black regions), edges of the UMZs defined using the wall normal-spanwise planes (black contour lines) and the projection of the UMZ edges identified over the wall normal-streamwise planes (magenta regions). (*a, b, c*) and (*d*) shows different combinations of the UMZ edges and the shear layers for better comparison. Results correspond to the flow contion at $Re = 752$, and backgound colormap shows the instantaneous streamwise velocity normalised by U_{cl}.

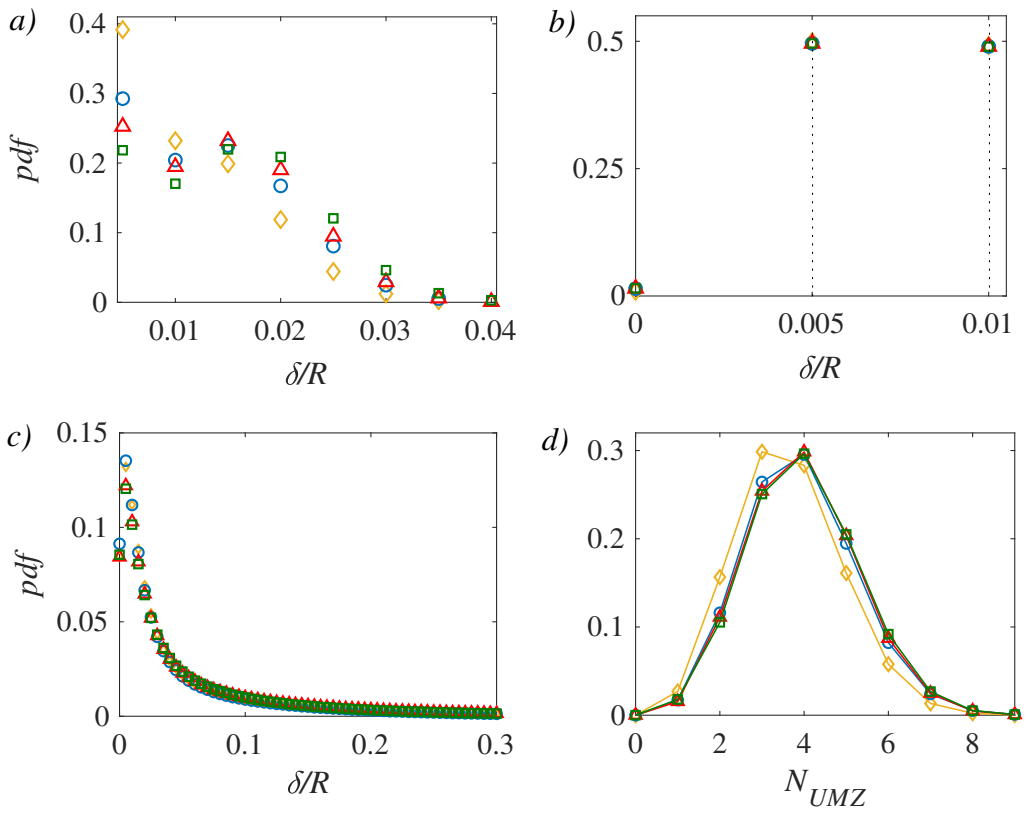

Figure 4.10: *Pdf* of the distance of the core of the shear layers (Chapter 3) from the edges of the UMZs defined using the wall normal-streamwise planes (*a*) and using the wall normal-spanwise planes (*b*). (*c*) *Pdf* of the distance of the UMZ edges determined in wall normal-streamwise planes to the UMZ edges detected using the wall normal-spanwise planes. (*d*) *Pdf* of the number of the UMZs which were determined based on the occurance of shear layers at each spanwise and streamwise direction. Yellow (diamond), blue (circle), red (triangle) and green (square) correspond to the flow conditions $Re = 340$, 752, 999 and 1259, respectively.

sition, over which the histogram is constructed using the streamwise velocity information. Therefore, the spanwise width of the UMZ edges could not be obtained. With the current work, on the other hand, the UMZ edges that were obtained over the wall normal-streamwise planes at each azimuthal position were projected onto the cross section of the pipe. With this approach, the spanwise extent of the UMZ edges could be visualised. The results showed that the UMZ edges appear to be connected in the spanwise direction (when the densely populated regions of the UMZ edges are considered).

Furthermore, different than in previous studies, a different orientation of the plane, *i.e.* wall normal-spanwise plane, was also used to investigate the UMZ edges in the cross section of the pipe with the same histogram approach. Analysis with this new plane also revealed similar UMZ edges that are separating regions of nearly uniform velocities, similar to the findings in the wall normal-streamwise planes.

In the last part of this chapter, the UMZ edges defined using the histogram approach with two different orientation of the planes were compared with each other, as well as the shear layers that were defined using the 3D detection method. Both visual results and the quantitative analysis showed that the detected shear layers mostly reside over the detected UMZ edges, such that the distance of the core of the shear layers from the UMZ edges was found to be much smaller than the thickness of the shear layers. However, since the spanwise and streamwise lengths of the intense shear regions do not appear as long as the UMZ edges, also because of the nature of the histogram method, the reverse does not hold, *i.e.* the detected UMZ edges through the histogram method do not always appear to overlap with the shear layers defined by the 3D method.

5

AN EXPERIMENTAL STUDY ON RAMP-TYPE ACCELERATING/DECELERATING TURBULENT PIPE FLOWS

5.1 INTRODUCTION

From the blood flow in large arteries to the flow over wind turbine rotors, unsteady turbulent flows are commonly encountered in nature as well as in engineering and biomedical sciences. Considering its practical impact on these fields, the ability to accurately predict and model these type of flows is very important. The research on unsteady turbulent flows is also important to gain further insight into the nature of turbulent flows. In particular, the non-periodic unsteady flows, which is the focus of this chapter, can reveal valuable information about the non-equilibrium state of turbulent flows.

Studies on unsteady turbulent flows can be classified into two broad groups, *i.e.* periodic and non-periodic flows. For periodic turbulent flows, the unsteadiness is imposed by periodic pulsations (having non-zero mean flow) or oscillations (having zero mean flow). The frequency and amplitute of these regular changes together with the mean flow rate define the unsteady flow (*e.g.* Mizushina *et al.* [89]; Tardu *et al.* [115], Choi *et al.* [23], Maurizio & Stefano [100], He & Jackson [50]). Non-periodic turbulent flow, on the other hand, is a non-equilibrium state. These type of flows are studied by either a rapid (step-like) or a gradual (ramp-like) change in the initial statistically steady turbulent state that eventually ends up with a different turbulent state. The process is highly dependent on the rate at which the unsteadiness is imposed and the difference between the initial and final turbulent states.

One of the earliest works on unsteady turbulent flow was conducted experimentally by Maruyama *et al.* [86]. They considered turbulent pipe flow and achieved the unsteadiness by a step-like change in the mass flow rate by the help of solenoid and sluice valves. They carried out instantaneous velocity and wall shear stress measurements by an electrochemical method (with probes made of platinum wires). The variation in the turbulence intensity led them to conclude that the propagation and generation of the new turbulence was the dominant process after the sudden increase in the mass flow rate in the pipe, while the decay of the old turbulence is the leading process after the step-like decrease. They also observed that the turbulence first responded near the wall, and then the response propagated towards the core of the pipe. This finding was later supported by the experiments of He & Jackson [49], who studied constantly accelerating and decelerating turbulent pipe flows using two-component laser Doppler anemometry (LDA). They also detected three different delays in the response of turbulence, *i.e.* in turbulence production, energy redistribution among its three components, and radial propagation of turbulence.

Considerable effort has also been put into the investigation of wall shear stress behaviour after the onset of unsteadiness (Shuy, [110]; Kurokawa & Morikawa [72], Ariyaratne *et al.* [6], Brunone & Berni [19], He *et al.* [47], [48]). He *et al.* ([47], [48]) observed that depending on the balance between the inertia of the flow and the delays in the response of turbulence, the wall shear stress undergoes three different stages in a gradually accelerated turbulent pipe flow. During the first stage, the wall shear stress first overshoots the quasi-steady value, and then decreases until it undershoots. The second phase starts

with the generation of new turbulence, which increases the wall shear stress again. Finally, in the third stage, the wall shear stress approaches the quasi-steady value. If the total wall shear stress is split into the quasi-steady and unsteady parts, it was reported that the latter component tends to be positive for an accelerated flow due to inertia (due to increase in the velocity gradients), while the delays in the response of turbulence tend to cause a negative value for the unsteady wall shear stress (Vardy *et al.* [125], He *et al.* [48]). Similar competition between the inertia and delays in the response of turbulence occur for a gradually decelerating flow too, which finally determines the sign of the unsteady component of the wall shear stress (Ariyaratne *et al.* [6]).

In addition to these studies, a different perspective on the transition process of non-periodic flows was introduced by He & Seddighi ([51]) based on their DNS in a turbulent channel flow exposed to a step increase in the flow rate. They argued that the transition from a certain turbulent state at low Reynolds number ($Re_b = 2800$) to another turbulent state ($Re_b = 7400$) is similar to a boundary layer bypass transition due to free stream turbulence. Here, Re_b is defined based on the bulk velocity and half channel height. They reported three distinct stages during the turbulent transition process, namely: pre-transition, transition, and fully turbulent stages. When compared with laminar-turbulent transition, these phases correspond to buffeted laminar flow, the intermittent flow, and fully turbulent flow phases. They showed that the initial streaky structures become elongated in the streamwise direction during the pre-transition stage. With the generation of local turbulent spots, due to the growing instabilities, the transition stage starts. These turbulent spots grow both in the streamwise and spanwise directions until they inhabit the entire wall surface, which finally completes the whole transition process. Later, He & Seddighi ([52]) extended this work with different initial and final Reynolds numbers ranging from $Re_b = 2800$ to $Re_b = 12600$. Although they found the same three phases resembling the laminar-turbulent transition, they observed significant differences in the flow structures depending on the Reynolds number ratio. For low Reynolds number ratios, for instance, the elongated streaky structures and turbulent spots become less identifiable.

The existing literature on non-periodic turbulent flows is quite limited. In particular, very little is known about the coherent structures (*e.g.* large scale motions, shear layer structures) and their development along accelerating/decelerating flows. To shed some light on this issue, an experimental investigation with stereo-PIV was conducted in accelerating and decelerating turbulent pipe flow. The ramp-type unsteadiness for both cases were achieved by a constant change in the mass flow rate starting from an initial statistically steady turbulent state.

This chapter is organised as follows: A description of the experimental setup, methodology and flow conditions is given in section 2. This is followed, in section 3, by the results of the first and second order turbulence statistics, the structural properties of coherent motions based on two-point correlations and a brief discussion of the development of shear layer like structures along the acceleration/deceleration. Finally, the findings are summarized in section 4.

5.2 EXPERIMENTAL DATASETS AND METHODOLOGY

The stereo-PIV experiments for steady and unsteady flow conditions were performed in the same pipe flow facility that was introduced in Chapter 2. The experiments for the statistically steady flow conditions were carried out at Re_D = 15393 and Re_D = 47727. Here, Re_D is the Reynolds number based on the diameter, D, of the pipe, $Re_D = U_b D/\nu$, where U_b is the bulk velocity, and ν is the kinematic viscosity of the fluid (which is water for the current experiments). Further details about these datasets including the accuracy of these measurements can be found in Chapter 2.

The unsteady cases, on the other hand, were achieved through a ramp-type change in the mass flow rate, which was controlled with a LabView programme. The first unsteady case covers the experiments conducted along the imposed acceleration from an initial steady turbulent state of $Re_D = 15393$ to a different turbulent state where $Re_D = 40228$ (Figure 5.1 (*a*)). The second case, on the other hand, consists of the experiments where the mass flow was decelerated at a constant rate from the steady turbulent state, Re_D = 47727, to $Re_D = 23396$ (Figure 5.1 (*b*)). Using the same LabView programme, the two high-speed cameras were triggered by the initial input sent to the centrifugal pump to change the flow rate, and the time-resolved stereo-PIV images were recorded in the cross section of the pipe for ~ 2.1 s.

Due to a time lag in the mass flow meter (Krohne-Altometer), the resulting bulk velocity information from the flow meter was rendered inaccurate. Therefore, at each time instant, the bulk velocity was determined based on the data from the stereo-PIV images. The difference between the bulk velocities determined from the PIV images and the flow meter is less than 2.5% for all the steady flow conditions considered in this chapter. Therefore, similar error is expected in the determination of the bulk velocity during the ramps. Consequently, the evaluation of the Reynolds number (Figure 5.1) was derived using stereo-PIV. As can be seen in these plots, for both cases after a time lag of ~ 0.21 s, the Reynolds number starts to change. On the other hand, it can be seen that both ramps are quite repeatable, where a maximum deviation of $\sim 1.3\%$ and $\sim 0.34\%$ occurs among the repeated cases for the accelerated and decelerated cases, respectively. These deviations are acceptable considering the maximum deviation occurring among the repeated steady cases, which is $\sim 0.3\%$. Furthermore, to analyse the development of the response of turbulence, as well as the structural properties along these ramps, the trajectories in Figure 5.1 (*a* and *b*) are divided into five equal length segments, *i.e.* $T_1 = t_1 - t_2$, $T_2 = t_2 - t_3$, $T_3 = t_3 - t_4$, $T_4 = t_4 - t_5$ and $T_5 = t_5 - t_6$, where $t_1 = 0$ s, $t_2 = 0.42$ s, $t_3 = 0.84$ s, $t_4 = 1.26$ s, $t_5 = 1.68$ s and $t_6 = 2.1$ s. The statistical properties are averaged over these sections in order to improve statistical convergence.

As previously mentioned, both steady and unsteady turbulent flows were captured with high-speed, stereoscopic PIV, where the measurement plane was perpendicular to the streamwise velocity. The thickness of the light sheet was 0.9 mm. The particle images were recorded using two high speed CMOS cameras with a 2176×1600 pixel format

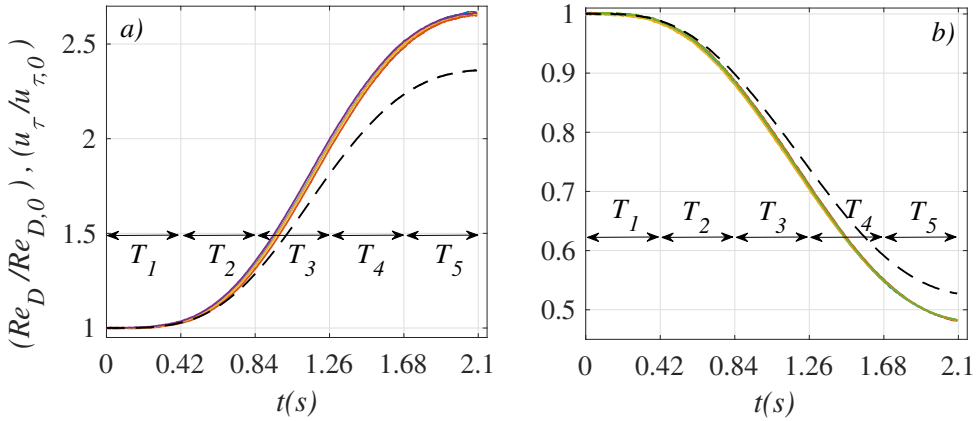

Figure 5.1: Excursions of the ramp-type accelerating (a) and decelerating (b) unsteady turbulent flow cases, along which the time-resolved PIV images were recorded. Solid lines correspond to $Re_D/Re_{D,0}$, and different colours represent the repeated experiments for the same case. Here, Re_D, and $Re_{D,0}$ represents the instantaneous and initial Reynolds numbers, respectively, which are defined based on the bulk velocity, U_b, and the diameter of the pipe, D. Black dashed lines correspond to the instantaneous wall friction velocity, u_τ, normalised by the initial value, $u_{\tau,0}$, during the same excursion. The excursions for both unsteady cases last $t \sim 2.1$ s.

(Phantom VEO 640L 4M, LaVision). The field of view of was $2.39R \times 2.23R$, where R is the radius of the pipe. The high speed cameras were equipped with a Micro-Nikkor F105 mm objective operating at an aperture number of $f_\# = 11$, and the time-resolved vector fields were captured at a frame rate of 0.859 kHz. Three independent sets for the steady cases, and 4 and 5 sets for the accelerating and decelerating flow cases were collected, respectively, where each set contains 1799 instantaneous velocity fields.

For all these experiments, calibration, data acquisition, and post-processing were performed with a commercial software package (Davis 8.4, LaVision). The PIV images were interrogated with a multi-pass interrogation technique, where the final interrogation windows had a 24×24 pixel size with 75% overlap, corresponding to a spatial resolution based on the window size of 11.1 and 29.7 viscous wall units u_τ/ν for the steady cases, $Re_D = 15393$ and 47727, respectively. The spatial resolution of the unsteady cases varies between these two numbers.

Similar to the previous chapters, r, θ and x represents the radial, azimuthal and axial coordinates, respectively. With a coordinate transformation from the cylindrical coordinates to the Cartesian coordinates, x, $y = R - r$ and $z = r\theta$ represent the streamwise, wall normal and spanwise direction, respectively. The corresponding instantaneous velocity components are shown by u, v and w. Velocity fluctuations are denoted by prime symbols (*e.g.* u'), and mean quantities are denoted by capital letters (*e.g.* U). The superscript '+' is used to denote the inner scaling of length (*e.g.* $y^+ = yu_\tau/\nu$) and velocity (*e.g.* $u^+ = u/u_\tau$). Moreover, in this chapter, u_τ and $u_{\tau,0}$ represents the wall friction velocity for the instantaneous and initial steady state flow conditions, respectively. Note that, all these wall friction

definitions are based on the Blasius emprical correlation [15], since direct (fast enough) pressure measurements were not possible during the current experiments.

5.3 RESULTS AND DISCUSSION

5.3.1 FIRST AND SECOND ORDER TURBULENCE STATISTICS

One of the difficulties in unsteady turbulent flow studies is to acquire a large number of independent samples, which is crucial for accurately determining the velocity fluctuations and therefore the turbulence statistics. In this work, to determine the velocity fluctuations, at each time instant, t, along the ramp, the local mean velocity at each wall normal position, y, is determined by averaging the independent sets, n, and also using spanwise averaging, z, (*e.g.* $u'(y, z, t, n) = u(y, z, t, n) - U(y, t)$), with:

$$U(y, t) = \frac{1}{Z \times N} \sum_{z=1}^{Z} \sum_{n=1}^{N} u(y, z, t, n). \tag{5.1}$$

Here, Z and N represents the total azimuthal points at each wall normal position and the number of the independents sets, respectively. Note that the present method is only for determining the velocity fluctuations; all the turbulence statistics (*e.g. rms*, two-point correlations) were determined based on the standard approaches, as in Chapter 2.

To assess the accuracy of the fluctuations determined by this method, the *rms* profiles based on this method were compared with those based on both temporal and spanwise averaging (the standard approach) for the steady cases, *i.e.* $Re_D = 15393$ and 47727. Figure 5.2 (*a, b*) show the resulting *rms* profiles between $y/R = 0.05 - 1$ for both cases. It can be seen in Figure 5.2 that the fluctuations determined on basis of the method defined in this chapter is in quite good agreement with their counterparts defined by the standard approach, except at the wall normal distances above $y/R = 0.8$. Near the core of the pipe, apparently, more samples are needed to accurately define the velocity fluctuations. In the present chapter, the analysis was conducted between $y/R = 0.1 - 0.8$, and the deviations in the *rms* of the streamwise velocity fluctuations were found to be less than 3.6% everywhere in this range for both flow conditions. For the other *rms* profiles, the results are identical except the *rms* profile of the wall normal velocity fluctuation for $Re_D = 15393$, where an overestimation around $\sim 7\%$ is observed. Further details about the accuracy of the steady data itself can be found in Chapter 2.

For further analysis, the data along the unsteady accelerating and decelerating ramps were divided into five equal time intervals (see Figure 5.1 (*a, b*)), over which the turbulence statistics were determined. Figure 5.3 shows the profiles for the mean streamwise velocity over each time interval for the accelerating (*a, c*) and decelerating (*b, d*) flows. In (*a, b*), it can be seen that in the first time interval, there is no change in the mean streamwise velocity profiles. Starting with the second interval, deviations from the initial profiles

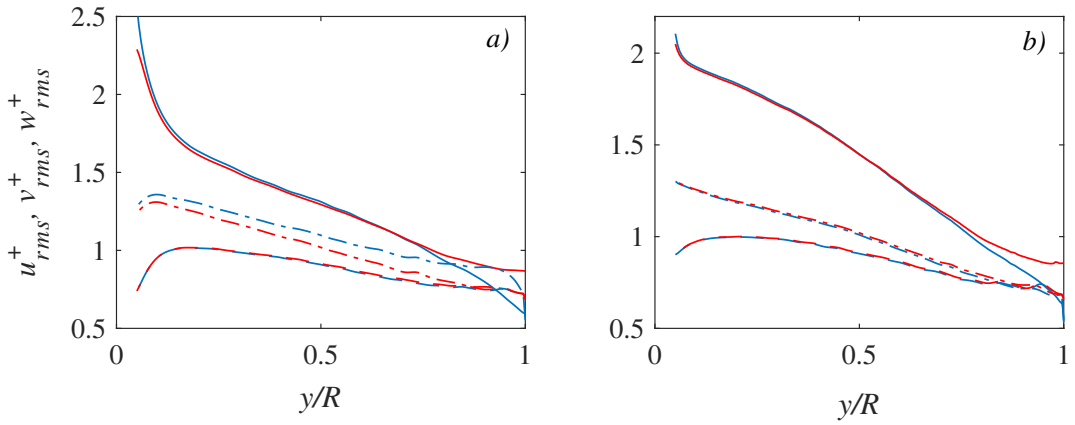

Figure 5.2: *Rms* profiles of the velocity components for the steady cases, *i.e.* $Re_D = 15393$ (*a*) and 47727 (*b*). Solid (−), dashed (−−) and dotted-dashed (−·) lines correspond to u^+_{rms}, v^+_{rms} and w^+_{rms}, respectively. Profiles shown by red correspond to the results using the velocity fluctuations determined from the standard approach, while the profiles shown by blue present the results where the velocity fluctuations were determined based on the method described in this section. For both approaches, however, time resolved data used for the determination of the *rms* profiles.

become significant. When the mean streamwise velocity profiles are normalised by the instantaneous wall friction velocity, it can be seen that the mean velocity profiles for the decelerating flow (*d*) follow the log law for each time interval. For the accelerating case (*c*), on the other hand, starting with the second time interval, deviations in the log region appear. The mean streamwise profiles first overshoot the profile for the initial steady case (shown in blue) in the log region, then become quite similar again, and in the final time interval undershoot it. Considering the studies of He *et al.* ([48], [47]) who reported the response of the wall friction for an accelerated turbulent pipe flow, the deviations from the log profile could be due to a possible discrepancy between the real wall friction during the acceleration and the one determined from the PIV images, which is based on Blasius theory for a statistically steady flow. Otherwise, it implies the difference in the behaviour of accelerated flow from the steady turbulent flow. The decelerating flow, on the other hand, behaves like a quasi-steady flow, where all the profiles determined from each time interval collapse, when the wall friction velocity information is derived from steady Blasius theory.

For the same time intervals along the ramps, the *rms* of the streamwise velocity fluctuations and the turbulent shear stress profiles are shown in Figure 5.4 (*a, c*) and (*b, d*), respectively. Profiles in (*a, b*) correspond to the results for the accelerated flow, while the profiles for the decelerated flow are shown in (*c, d*). For both the accelerating and decelerating cases, it can be seen that there is a delay in the response of turbulence to the change in the mass flow rate, such that the profiles from the first two sections are nearly identical when normalised by the initial $u_{\tau,o}$. When the *rms* of the streamwise velocity and

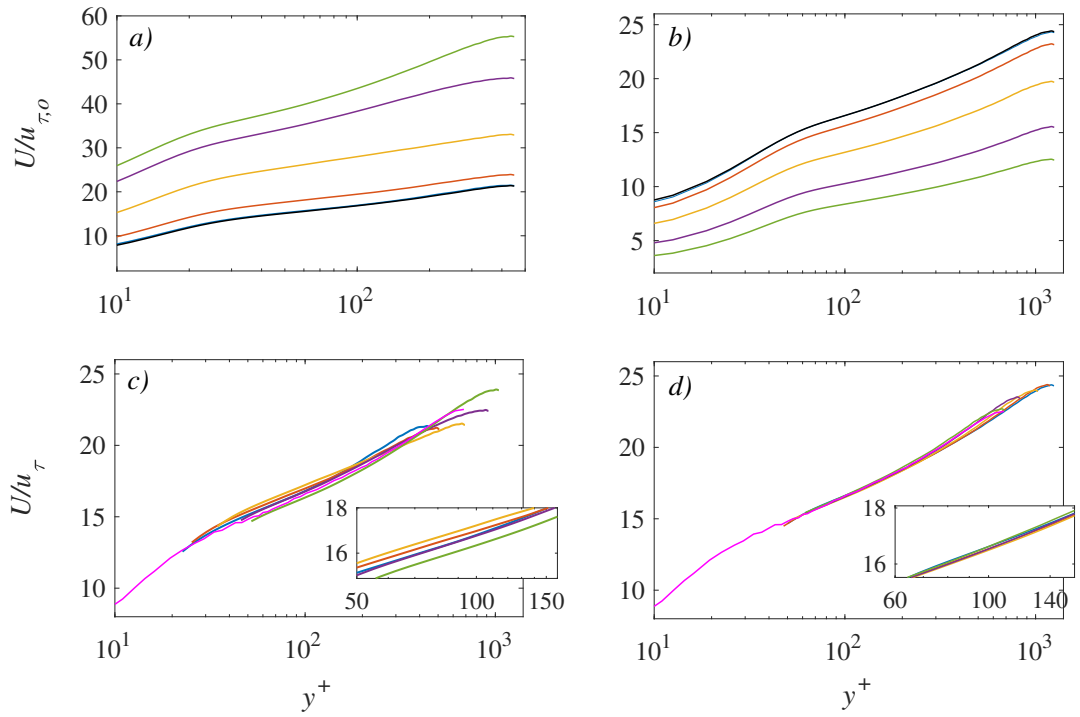

Figure 5.3: Mean velocity profiles of the streamwise velocity, U, for the accelerating flow, (*a, c*) and decelerating flow, (*b, d*). The mean profiles in (*a* and *b*) are normalised by the initial wall friction velocity, $u_{\tau,0}$, while profiles in (*c* and *d*) are normalised by the instantaneous wall friction velocity, u_τ. Both $u_{\tau,0}$ and u_τ are determined using the bulk velocity information from the PIV images. Blue, red yellow, purple and green lines correspond to the data averaged over T_1, T_2, T_3, T_4 and T_5, respectively. Profiles shown by black (*a* and *b*) and magenta (*c* and *d*) correspond to the statistically steady initial flow conditions and the experimental data of Toonder & Nieuwstadt ([121]) at $Re_D = 24600$, respectively. Insets in (*c* and *d*) provide closer views.

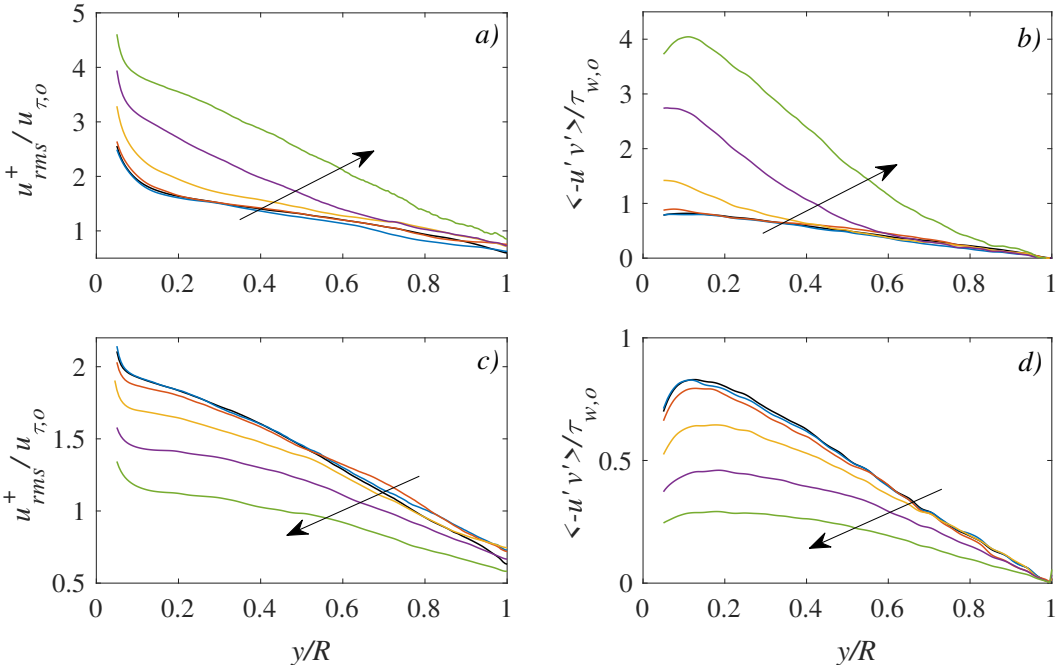

Figure 5.4: *Rms* profiles of the streamwise velocity fluctuation, u^+_{rms}, (*a, c*) and Reynolds shear stress, $(-\overline{u'v'})$, (*b, d*), for the accelerating (*a, b*) and decelerating (*c, d*) flows. *Rms* and Reynolds shear stress profiles are normalised by the wall friction velocity, $u_{\tau,0}$, and the wall friction, $\tau_{w,\,o}$, of the initial steady state. Blue, red yellow, purple and green lines correspond to the data averaged over times T_1, T_2, T_3, T_4 and T_5, respectively. Black lines show the initial steady data. Arrows shows the direction of the time increase.

Reynolds shear stress profiles are normalised by u_τ and τ_w, respectively, it can be seen in Figure 5.5 that the overall turbulence intensity and turbulent shear stress are lower for the accelerating case, whereas they are higher for the decelerating case when compared with their steady counterparts. This again may be explained by a delay in the response of turbulence.

Finally, the *rms* of all the velocity components as well as turbulent shear stress profiles are plotted versus time (Figure 5.6). For convergence, the data was averaged over certain bins, *i.e.* $y/R = 0.1-0.2,\ 0.2-0.3,\ 0.3-0.4,\ 0.4-0.5,\ 0.5-0.6,\ 0.6-0.7,\ 0.7-0.8$. Moreover, the profiles were smoothed using a moving average filter with a length of $l_w/l = 0.056$, where l is the overall temporal length of the data (in seconds). As has been reported in the literature, the response of turbulence is observed to appear first near the wall for both cases (accelerating and decelerating), and then it propagates towards the core of the pipe.

5.3.2 TWO-POINT SPATIAL CORRELATIONS

In this section, the development of two-point correlations along the accelerating and decelerating ramps is investigated. Similar to § 5.3.1, the averaging was performed over five

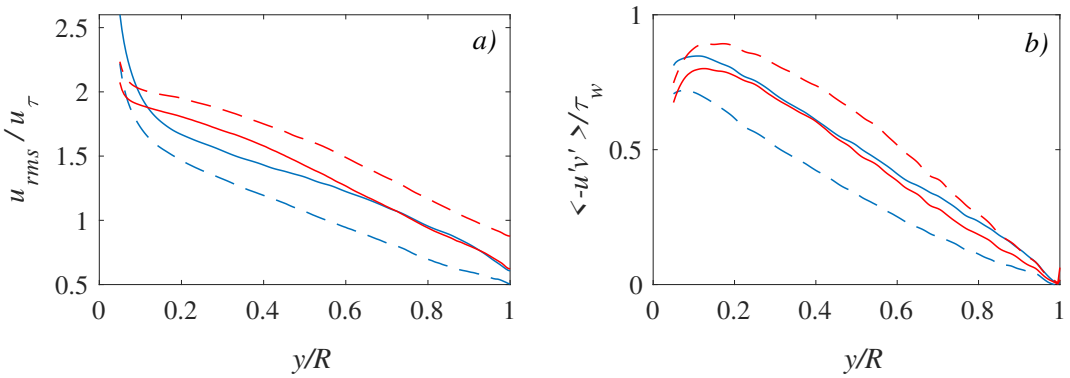

Figure 5.5: *Rms* profiles of the streamwise velocity fluctuation, u^+_{rms}, (*a*) and Reynolds shear stress, $(-\overline{u'v'})$, (*b*). Solid blue and red lines represent the initial steady data for $Re_D = 15793$ and $Re_D = 47727$, respectively. Dashed blue and red lines correspond to the averaged data along the accelerating and decelerating ramps, respectively. Profiles are normalised by the instantaneous wall friction velocity, $u_{\tau,}$, and wall friction, τ_w, determined from the PIV snapshots averaged over the independent sets.

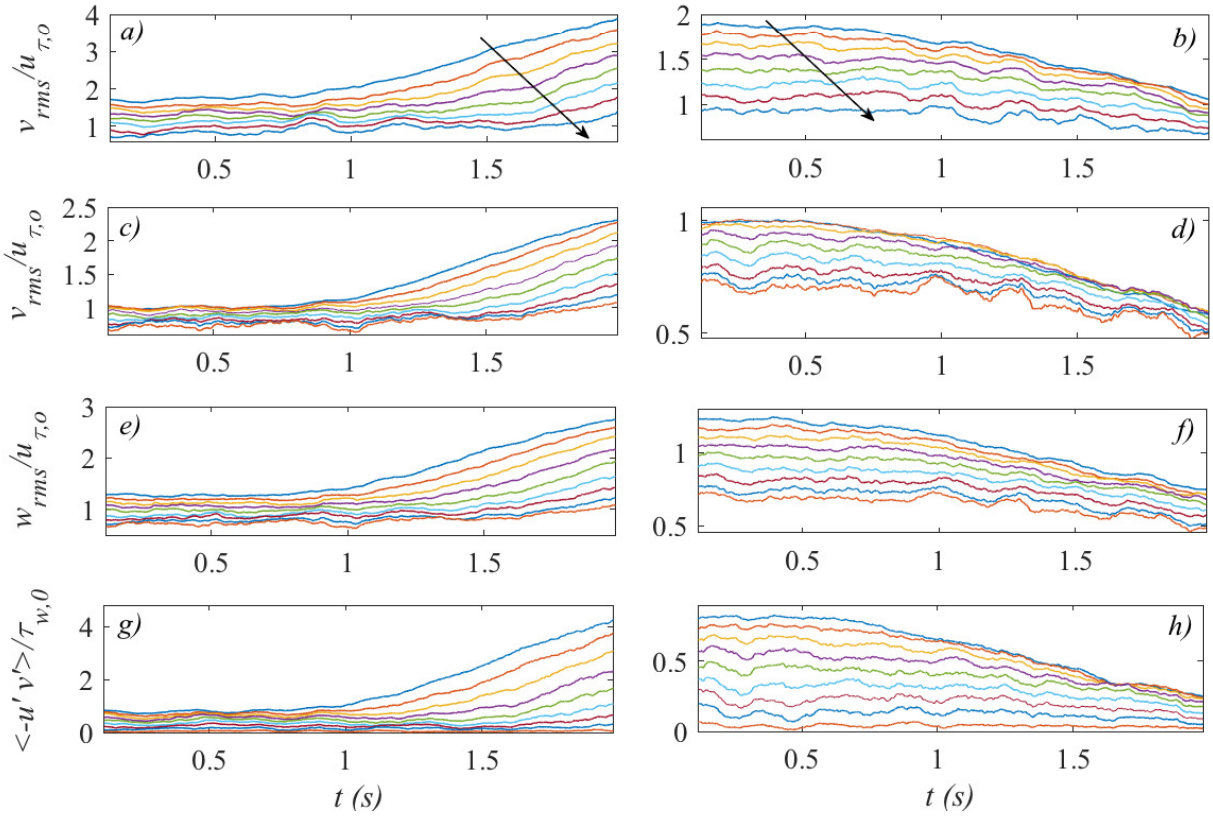

Figure 5.6: *Rms* profiles of the streamwise velocity, u^+_{rms}, (*a, b*), wall normal velocity, v^+_{rms}, (*c, d*), azimuthal velocity, w^+_{rms}, (*e, f*) and Reynolds shear stress, $-\overline{u'v'}$, (*g, h*), for the accelerating (*a, c, e, g*) and decelerating (*b, d, f, h*) flows. *Rms* and Reynolds shear stress profiles are normalised by the wall friction velocity, $u_{\tau,0}$, and the wall friction, $\tau_{w,0}$, of the initial steady state. Arrows shown in (*a, b*) denote (for each column) the direction of the binned data from the wall ($y/R = 0.1 - 0.2$) to the core of the pipe ($y/R = 0.7 - 0.8$) with an equal increment of 0.1.

different time intervals along the ramps. Results are compared with those for the steady cases (Chapter 2).

Two-point correlations are examined first in the spanwise-wall normal planes for each time interval for four different reference wall normal positions. The contours of the resultant two point correlation coefficients are shown in Figure 5.7 for the accelerating flow and in Figure 5.8 for the decelerating flow. In these figures, the contours shown in the first row correspond to the correlation coefficients for the initial statistically steady cases, Re_0, and the remaining rows present the ones over the previously specified time intervals. Since over the first time interval, T_1, no significant changes were observed in the flow as discussed in the previous section (§ 5.3.1), the differences between the results in the first and the second rows could be explained by convergence. For both cases (accelerated or decelerated), the contours of the correlation coefficients over each time interval are very similar to those of the steady cases (see also Chapter 2), where the positive correlations are surrounded by negatively correlated ones. These results show that during the studied acceleration or deceleration, the large-scale motions present initially in the steady flow preserve their structural organisation in the spanwise-wall normal planes.

Two-point correlations were also computed in the spanwise-streamwise planes for several reference wall normal locations. The resulting contours of the correlation coefficients are presented in Figure 5.9 and Figure 5.10 for the accelerating and decelerating flows, respectively. Note that the streamwise extend of the flows were constructed using Taylor's hypothesis with local mean velocity over each time interval. Similar to the correlations in the spanwise-wall normal planes, the correlation coefficients in the spanwise-streamwise planes also show that the averaged structural organisations are very similar to those reported for the steady flow conditions (Chapter 2).

Furthermore, using the method described in Chapter 2 (Figure 2.7), the width (l_z) and the length (l_x) of these correlation peaks were quantified for $R = 0.5$ over each time interval along the ramps. Figure 5.11 (*a, c*) show the width (*a*) and the length (*c*) of the correlation coefficients for the accelerating flow, while (*b, d*) correspond to the width (*b*) and the length (*d*) of the correlation coefficients for the decelerating flow. The error bars in these profiles show the maximum deviations from the mean considering each repeated sets for the same time interval. For the decelerated flow, it can be seen in (*b*) that the width of the correlation peaks in the first time interval (at each reference wall normal position) are almost identical to the ones obtained for the initial steady turbulent state. This was expected for the convergent results since no changes were observed in the turbulence statistics over this time interval when compared with the initial steady case. Similarly, over the second time interval, it can be seen that the width of the peaks are preserved at each wall position. However, over the third and the fourth time intervals, a significant increase in the width of the correlation coefficients is observed for the reference wall positions $y/R < 0.6$. The increase in the core region occur in the fourth interval. In the final time interval, on the other hand, the width of the correlation peaks are observed to be similar at each reference wall position. The overall increase in the width of the correlation coefficients observed during

Figure 5.1 ations in the mal locations, nd 0.8 (fourth 5393; second, he time inter- grey contour s correspond to a negative correlation of −0.05 and −0.1, respectively.

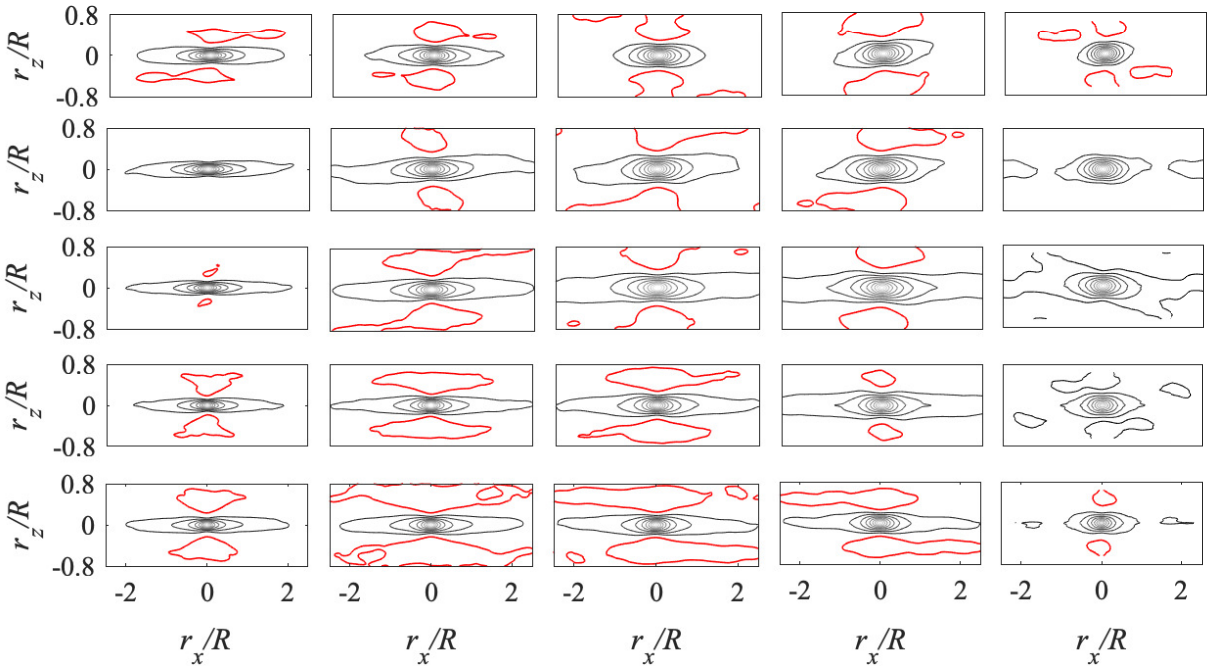

Figure 5.9: Two-point correlation coefficient of the streamwise velocity fluctuations in the spanwise-streamwise planes at several several wall normal locations, *i.e.* $y/R = 0.1$ (first column), 0.2 (second column), 0.35 (third column), 0.5 (fourth column) and 0.8 (fifth column). First, second, third, fourth and fifth rows represent the data over the time intervals T_1, T_2, T_3, T_4 and T_5, respectively, along the acceleration ramp. Positive correlations are shown by grey contour lines varied from 0.1 to 1, while red contour lines correspond to a negative correlation of -0.05.

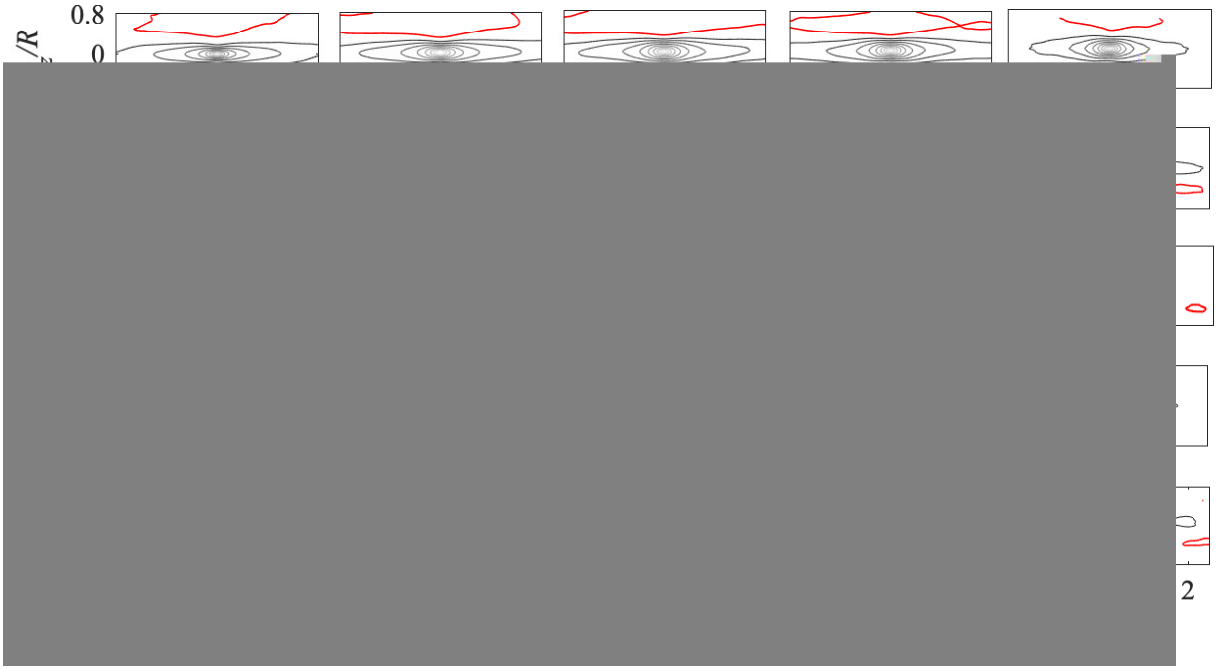

Figure 5.10: Two-point correlation coefficient of the streamwise velocity fluctuations in the spanwise-streamwise planes at several several wall normal locations, *i.e.* $y/R = 0.1$ (first column), 0.2 (second column), 0.35 (third column), 0.5 (fourth column) and 0.8 (fifth column). First, second, third, fourth and fifth rows represent the data over the time intervals T_1, T_2, T_3, T_4 and T_5, respectively, along the deceleration ramp. Positive correlations are shown by grey contour lines varied from 0.1 to 1, while red contour lines correspond to a negative correlation of -0.05.

the deceleration (between $Re_D = 47727 \rightarrow 23396$) is higher than the difference between the width of the correlation coefficients obtained in the steady flow conditions in the range $Re_D = 47727 \rightarrow 15393$ (shown in black data in the same figure). These results show that the width of the large scale motions increase during deceleration. During the acceleration, on the other hand, in the first three intervals, and for the wall positions $y/R < 0.5$, the widths of the correlation peaks are seen to be very similar (differences are within the maximum deviations that occur for each case). For $y/R \geq 0.5$, the differences could be explained by the lack of convergence since the observed difference at these wall positions is very similar to the difference observed between the repeated steady cases. Starting with the fourth time interval, a significant decrease in the width of the correlation peak is observed at the wall positions $y/R < 0.5$. The same width is preserved in the final interval near the wall; however, it increases dramatically for $y/R > 0.3$. Considering that the maximum deviations occurring in the repeated sets for the same time interval are smaller, this significant decrease in the last two intervals should be explained by the effect of the acceleration on the development of the averaged structures.

For the streamwise length of the correlation peaks during the deceleration, it can be seen in Figure 5.11 (*d*) that at each reference wall position the length scale is more or less constant when the time intervals are compared; at least the width of the correlation peaks are not decreasing with the decrease in the Reynolds number in time, as observed for the steady cases. Similarly, during the acceleration, especially near the wall, the streamwise width of the correlation peaks is seen to be very similar to each other over each time interval. Beyond $y/R > 0.4$, on the other hand, no clear trend is observed for the development of the length of the structures during acceleration. But, still the length of the averaged structures can be inferred to be of the same order when the results over each time interval are compared.

5·3·3 INTERNAL SHEAR LAYERS

In this section, shear-layer like structures bounding the regions of similar streamwise velocities are investigated for the current ramp-up/ramp-down turbulent flows using the same detection method as discussed in detail in Chapter 3. Some examples of these structures on the cross-section of the pipe (azimuthal-wall normal plane) during the flow development are shown in Figure 5.12 and Figure 5.13 for the accelerated and decelerated flows, respectively. The subplots correspond to different time instants along the ramps, *i.e.* 0.002 s (*a*), 0.63 s (*b*), 1.05 s (*c*), 1.47 s (*d*), 1.89 s (*e*) and 2.08 s (*f*). The shear layers (shown by black contours) are seen to have similar wall normal thicknesses and azimuthal lengths during the acceleration or deceleration, which was further quantified in Figure 5.14 (*a, b*) for the acceleration and deceleration cases, respectively. Here the open symbols represent the data over the time intervals along the ramps, while filled squares and circles correspond to the data at the initial steady state cases. To compare the results at different wall

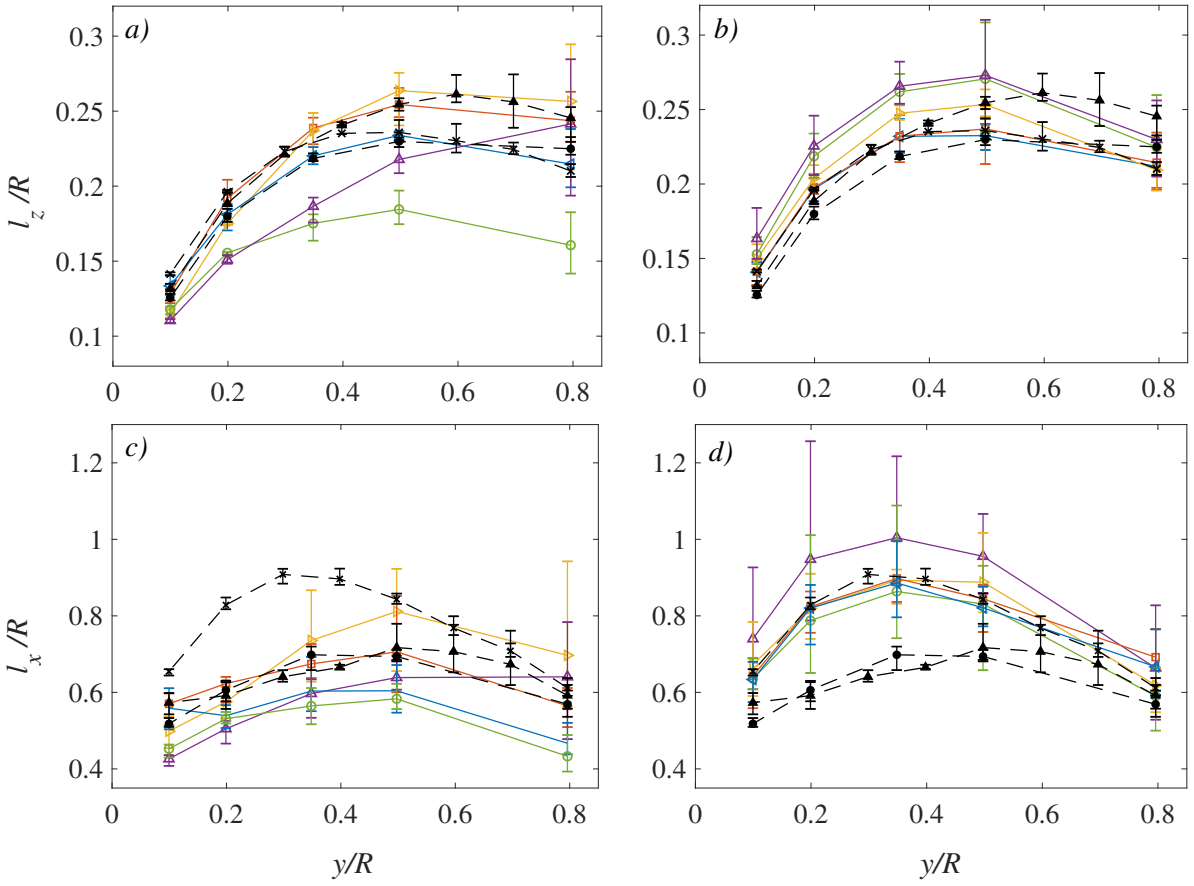

Figure 5.11: (Spanwise) width, l_z/R, (a and b) and streamwise length, l_x/R, (c and d) of the correlation peaks determined for $R_{uu} \geq 0.5$ at several wall normal locations. Data in (a and c) were obtained during the acceleration, while those in (b and d) were determined during the deceleration. Solid blue (◁), orange (□), yellow (▷), purple (△) and green (○) lines with the symbols correspond to the averaged length scales over the times T_1, T_2, T_3, T_4 and T_5, respectively. Results shown by black dashed lines with the (▲), (●) and (×) symbols belong to the steady cases at $Re_D = 15393, 27092$ and 47727, respectively, which were discussed in Chapter 2. Error bars show the maximum deviation from the mean occuring among the repeated sets.

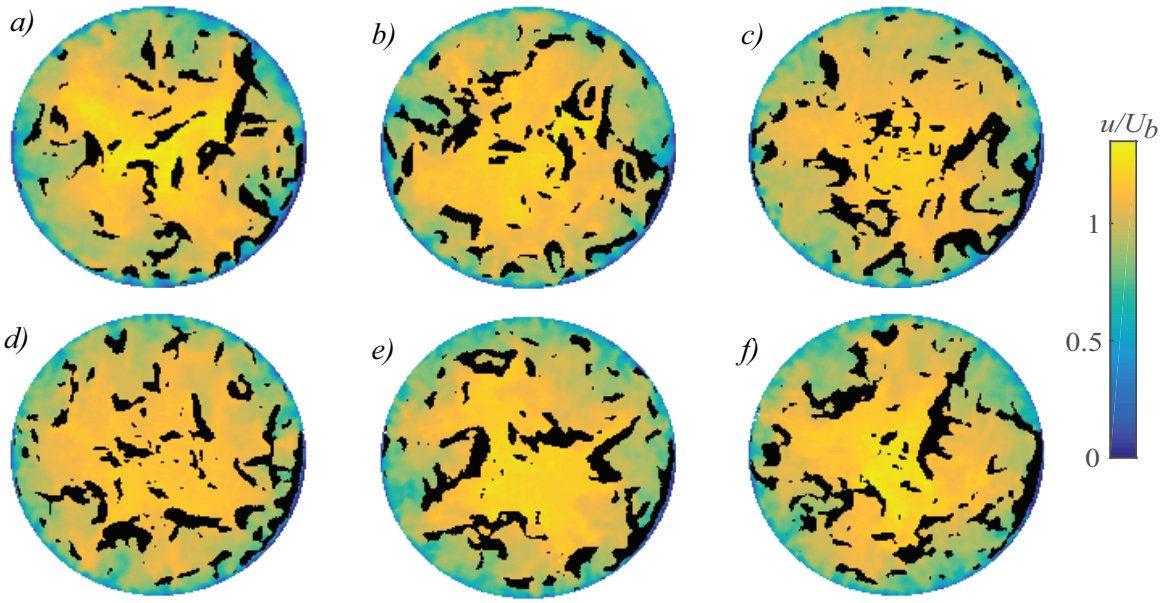

Figure 5.12: Instantaneous velocity fields for the streamwise velocity (colormap) together with the internal shear layers (shown by black contours) at different time instants along the accelerated flow, *i.e.* (*a*) ∼0.02 s, (*b*) ∼0.63 s, (*c*) ∼1.05 s, (*d*) ∼1.47 s, (*e*) ∼1.89 s and (*f*) ∼ 2.08 s. The streamwise velocities are normalised by the instantaneous bulk velocity, U_b.

normal locations, the shear layers are grouped based on the wall normal location of their centres, *i.e.* the layers between $y/R = 0.1 - 0.2$, $0.2 - 0.3$, $0.3 - 0.4$, $0.4 - 0.5$, $0.5 - 0.6$, $0.6 - 0.7$ and $0.7 - 0.8$.

In Figure 5.14 (*a, b*), it can be seen that the jumps in the streamwise velocity over the shear layers averaged for the first time interval are very similar to the jumps for the initial steady turbulent states for both ramps. This is expected since no significant effect of the unsteadiness is observed in this interval compared to the initial turbulent state. Also the average Reynolds number over this interval is very close to that of the initial steady state. When the initial steady turbulent states are compared, it is seen that these jumps are higher for the lower Reynolds number at each wall-normal location. The streamwise jumps over the layers in the first time interval for both ramps follow this behaviour. Starting with the second time interval, these jumps over the shear regions are seen to decrease as the Reynolds number increases along the ramp (Figure 5.14 (*a*)) until the final time interval, where the flow approaches steady state and the jumps are increasing again. Still, the final velocity jumps are lower than the velocity jumps observed at the initial Reynolds number. For the decelerating case, on the other hand, no significant changes are observed on the velocity jumps when the results for each time interval are compared (Figure 5.14 (*b*)). However, different than the accelerating flow, the jumps in the streamwise velocity along the decelerating ramp are observed not to decrease.

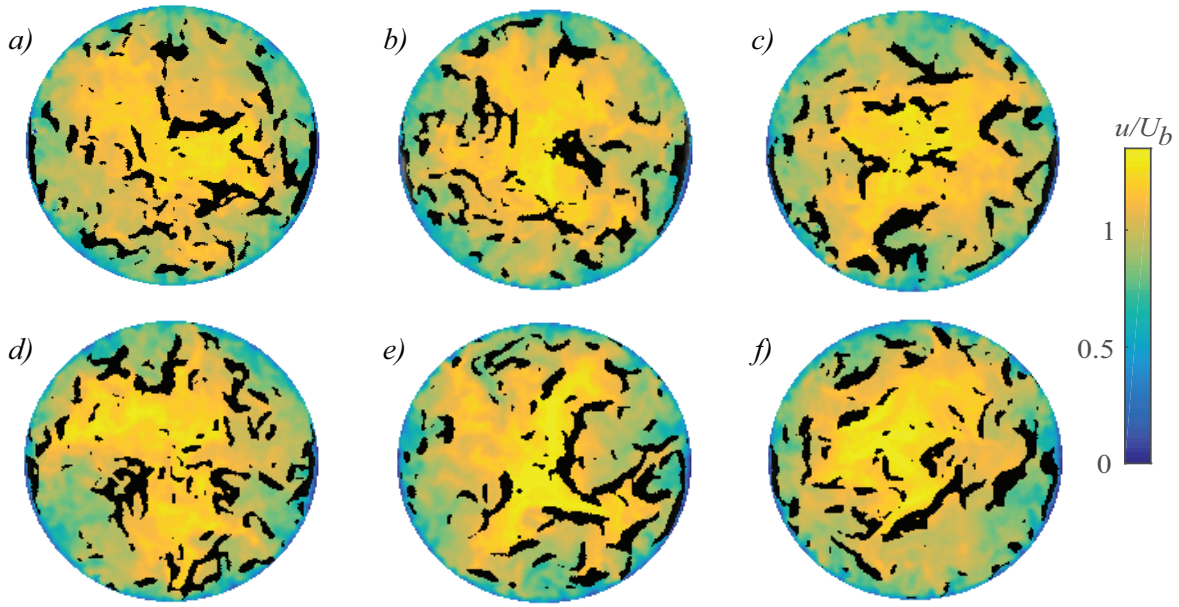

Figure 5.13: Instantaneous velocity fields for the streamwise velocity (colormap) together with the internal shear layers (shown by black contours) at different time instants along the decelerated flow, *i.e.* (*a*) ∼0.02 s, (*b*) ∼0.63 s, (*c*) ∼1.05 s, (*d*) ∼1.47 s, (*e*) ∼1.89 s and (*f*) ∼ 2.08 s. The streamwise velocities are normalised by the instantaneous bulk velocity, U_b.

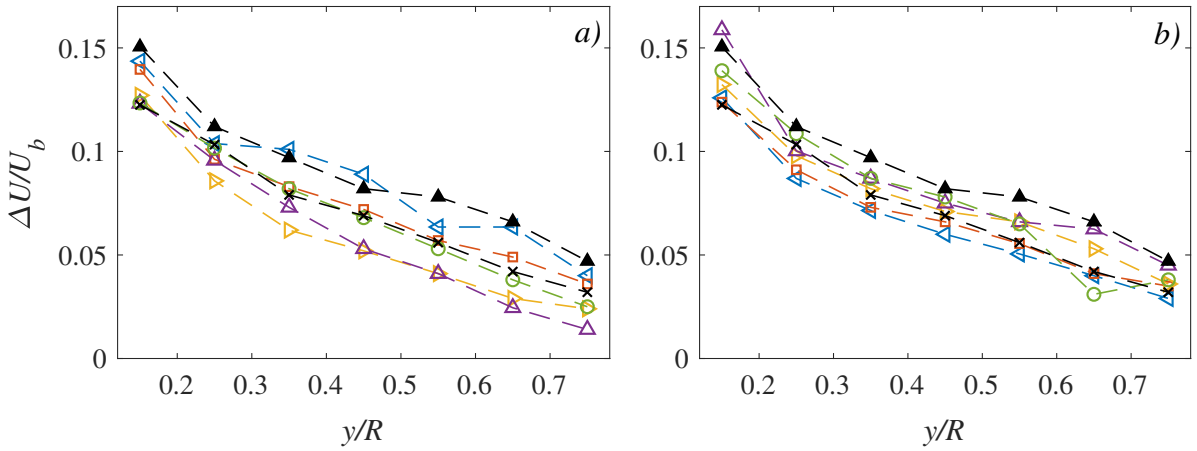

Figure 5.14: Conditionally averaged streamwise velocity jumps over the detected shear layers which were grouped according to their wall normal location for the accelerated flow case (*a*) and decelerating flow case (*b*). Dashed blue (◁), orange (□), yellow (▷), purple (△) and green (○) lines with the symbols correspond to the data the time intervals T_1, T_2, T_3, T_4 and T_5, respectively. Results shown by black dashed lines with the (▲) and (×) symbols belong to the steady cases at $Re_\tau = 459$ and $Re_\tau = 1233$, respectively.

5.4 CONCLUSIONS

In this chapter, an analysis was presented on accelerating/decelerating turbulent pipe flows based on a series of stereo-PIV measurements. The acceleration and deceleration in the flow was achieved by changing the mass flow rate from an initial statistically steady turbulent state to another turbulent state. The acceleration was imposed at an initial Reynolds number of $Re_D = 15393$ while the deceleration started from $Re_D = 47727$. The Reynolds numbers at the end of the ramp-type excursions were $Re_D = 40228$ and $Re_D = 23396$ for the accelerating and decelerating cases, respectively.

In the first part of the study, first and second order turbulence statistics were discussed along the ramp-up/ramp-down turbulent flows. It was seen that the decelerated flow behaves like a quasi-steady flow when the mean streamwise velocities normalized by the inner variables along five different time intervals are compared. Some deviations from the log law, however, were observed for the accelerated flow, which could be related to the behaviour of the wall friction velocity along the ramp-up flow. Also, similar to previous studies, delays in the response of turbulence were observed. The response was faster near the wall and then the adjustment propagated towards core of the pipe.

The second part of this chapter focused on properties of the energetic flow structures, in particular their width and length, through two-point correlations. The results revealed that the width and the length of the average structures are comparable to those of the average structures at steady flow conditions.

Finally, in this chapter, the internal shear layers were analysed using the detection method introduced in Chapter 3. Similar to the steady turbulent cases, the shear structures were observed to demarcate the regions of nearly uniform velocity as the unsteady flows develop along the ramps. However, as the flow accelerated it was seen that the magnitude of these velocity jumps is decreasing. For the deceleration, on the other hand, the jumps in the streamwise velocities over the shear layers were similar at each time interval along the ramp.

6

EXPERIMENTAL INVESTIGATION OF TORQUE HYSTERESIS BEHAVIOUR OF TAYLOR-COUETTE FLOW

This chapter is adapted from M. Gul, G. E. Elsinga, and J. Westerweel. "Experimental investigation of torque hysteresis behaviour of Taylor–Couette Flow." In: *Journal of Fluid Mechanics* 836 (2018), 635–648.

6.1 INTRODUCTION

Taylor-Couette flow occurs between two concentric and independently rotating cylinders. It represents one of the closed systems in fluid mechanics that is widely used as a model system for turbulence studies (*e.g.* see the recent review article by Grossmann *et al.* [42]). In this highly symmetric system, the power input can be controlled via the differential rotation of the cylinders, and the resultant energy dissipation can be measured by means of the torque on the cylinders. Different geometrical parameters and differential rotation of the cylinders enable us to observe various flow regimes (*e.g.* Andereck *et al.* [4], Dong [27], Tokgöz [119]).

The relevant geometrical parameters are the radius ratio, η, defined as the ratio of the inner and outer cylinder radius, and the aspect ratio, Γ, defined as the length of the cylinders, L, relative to the gap width, d (Figure 6.1 (*a*)). The flow conditions at the ends of the cylinders can also be considered as a geometrical parameter. Some other parameters defining Taylor-Couette flow are the shear Reynolds number, $Re_s = 2\,|\eta Re_o - Re_i\,|/(1+\eta)$, and the rotation number, $Re_\Omega = (1-\eta)(Re_o + Re_i)/(\eta Re_o - Re_i)$ (Dubrulle *et al.* [31]). Here, $Re_o = 2\pi f_o r_o d/\nu$ and $Re_i = 2\pi f_i r_i d/\nu$ are the outer and inner cylinder based Reynolds numbers, respectively, where f_o, f_i are the rotation frequencies and r_o, r_i are radii of the outer and inner cylinders, respectively, and ν is the kinematic viscosity of the fluid.

Andereck *et al.* [4] conducted flow visualisation experiments at a radius ratio of 0.883 and accordingly formed a comprehensive map of different flow states occurring in Taylor-Couette flow at low and moderate Reynolds numbers. At low inner and outer cylinder Reynolds numbers the flow was observed to be laminar with several distinct flow states. As they increased the Reynolds number to a shear Reynolds number of 5.9×10^3 no obvious structures were observed in the flow, and they termed this regime as 'featureless turbulence'. However, recent experimental and numerical studies (*e.g.* Bilson and Bremhors [13], Dong [28], Ravelet *et al.* [101], Tokgoz *et al.* [117], Huisman *et al.* [55], Ostilla-Mónico *et al.* [95]) showed the persistence of large scale structures even at much higher Reynolds numbers.

In their study, Lathrop *et al.* [75] proposed that a boundary layer transition to a turbulent regime occurs at a Reynolds number of 1.3×10^4 based on their highly accurate torque and wall shear stress measurements. Later, this finding was verified by local measurements by Lewis and Swiney [78]. The transition can also be seen in the torque scaling experiments of Wendt [128]. Recent experimental (*e.g.* Lathrop *et al.* [75], Huismann *et al.* [56]) and numerical (*e.g.* Ostilla-Mónico *et al.* [94]) studies showed that at Reynolds numbers beyond the transition the boundary layer is turbulent having a logarithmic velocity profile similar to other wall bounded turbulent flows.

Studies carried out by Brauckmann and Eckhardt ([18], [63]), van Gils *et al.* [38] and Paoletti & Lathrop [96] showed that optimum angular momentum transport occurs around moderate counter-rotation, *i.e.* $f_o/f_i \approx -0.4$ with radius ratios $0.5 < \eta < 0.7245$. A recent study conducted by Tokgöz [119] revealed that at a constant shear Reynolds number of

2.9×10^4 and a radius ratio of 0.917, coherent structures change orientation from Taylor vortices to inclined vortices and to Taylor column-like structures at rotation numbers of -0.083, -0.010 and 0, respectively. He relates this change in the orientation with the rotation numbers to the change in the angular momentum transport and therefore torque. So, depending on the control parameters, differences in turbulent states occur.

An interesting question raised recently is whether multiple states exist in turbulent Taylor-Couette flows at the same experimental conditions (Huisman *et al.* [55]). They performed torque and velocity measurements at a very high shear Reynolds number, of the order of 10^6. During their experiments they followed basically two different trajectories at a constant shear Reynolds number while varying a, defined as $a = -f_o/f_i$. One trajectory is in the direction of increasing a, while the other one is in the direction of decreasing a. Their results reveal that hysteresis occurs with a high probability (80%) within a certain range of values for a, *i.e.* $0.17 < a < 0.51$. They conjecture that this difference in the torque values is due to different turbulent states occurring in the Taylor-Couette flow. Later, Van der Veen *et al.* [126] continued this work with a different setup having a higher aspect ratio ($\Gamma = 18.3$ compared to $\Gamma = 11.7$ before). They measured the radial and azimuthal velocity components at several axial locations. Similar to their earlier study, they observed bifurcation and different velocity distributions for a certain range of values for a, most significantly in the radial velocity component. They concluded that hysteresis in highly turbulent Taylor-Couette flow is robust, meaning that it occurs also at $\Gamma = 18.3$. However, the detailed dependence of the hysteresis on the geometrical parameters, such as the aspect ratio, radius ratio and boundary conditions at the ends of a Taylor-Couette facility, remains unclear. Furthermore, we wonder if the torque hysteresis represents a genuine change in the turbulent flow state, *i.e.* the structure of velocity fluctuations, as opposed to a change in the base flow, *i.e.* mean flow. Hence, in order to understand the hysteresis or multiple states in turbulent Taylor-Couette flow further studies with different geometrical parameters and flow conditions are required.

In this study, we performed torque and PIV measurements for different geometrical configurations and flow conditions to study the hysteresis in Taylor-Couette flow up to a shear Reynolds number of 5.5×10^4, which is beyond the transition regime, and therefore can be considered as fully turbulent. Different geometrical configurations were achieved by changing the aspect ratio and the end conditions, while maintaining a radius ratio of $\eta = 0.917$.

This chapter is organised as follows: A description of the experimental setup and methodology is given in Section 6.2. This is followed, in Section 6.3, by the results of the torque measurements at different shear Reynolds number and aspect ratio, and the analysis based on the PIV measurements at the shear Reynolds number of 4.4×10^4 and aspect ratio of 88. Finally, the findings are summarized in Section 6.4.

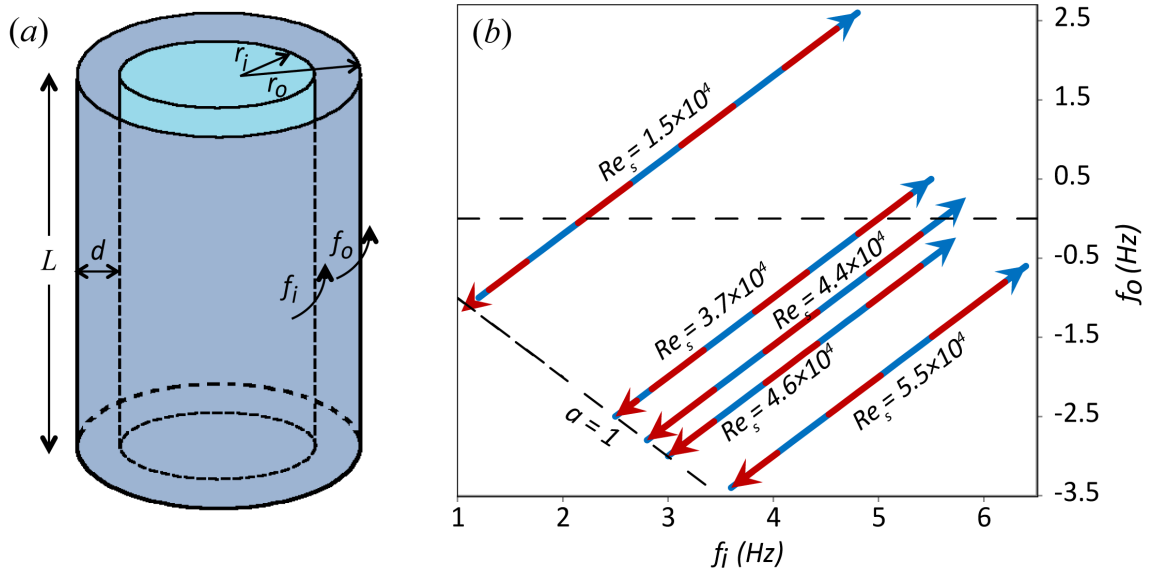

Figure 6.1: Schematic of a Taylor–Couette system (a) and sketch of the trajectories in the (f_i, f_o) parameter space followed during the torque measurements for different constant Re_s (b). The red and blue arrows respectively indicate the direction of increasing and decreasing frequency ratio, a, along each trajectory.

6.2 EXPERIMENTAL SETUP AND METHODOLOGY

Torque measurements were performed in the same Taylor-Couette flow facility with water as the working fluid. However, cylinders of different length were used to vary the aspect ratio. The axial aspect ratio, $\Gamma = L/d$, of the shorter and the taller cylinder was 22 and 88, respectively. Fully filled Taylor-Couette systems were closed at both ends with end plates rotating together with the outer cylinder. On the other hand, intermediate values for Γ were achieved by changing the water level in the taller cylinder, where the system had only the lower end plate while the upper boundary was a free surface (Figure 6.2). For all cases the inner and outer cylinder radii were $r_i = 110$ mm and $r_o = 120$ mm respectively, which resulted in a gap width $d = 10$ mm and a radius ratio of $\eta = 0.917$.

During the torque measurements the outer and the inner cylinders were rotated varying the frequency ratio, while maintaining a constant difference in the frequencies of the two cylinders, $\Delta f = f_i - f_o$. Therefore, the shear Reynolds number, Re_s, remained constant. In order to investigate the hysteresis in the torque, the frequency ratio, a, was first decreased incrementally, and at the end of the trajectory it was increased again with the same increments for each data set. Since the measurements with various step sizes showed that the hysteresis is not affected by the step size used, larger increments in a outside the hysteresis loop were used to shorten the overall measurement time. After each increment in a, torque data were collected for two minutes after waiting for the flow to reach stable conditions. Finally, the mean torque at each setting was computed. Figure 6.1 (b) shows these trajectories at five different constant shear Reynolds numbers in the (f_i, f_o) parameter space

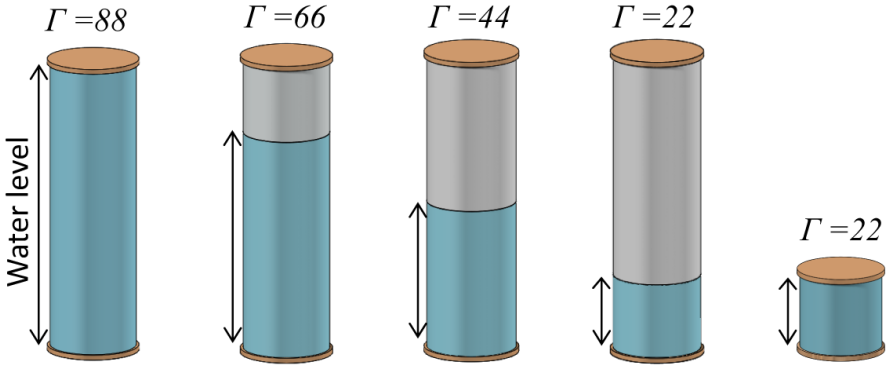

$Re_s = 1.5 \times 10^4$	Γ1R1				
$Re_s = 3.7 \times 10^4$	Γ1R2				
$Re_s = 4.4 \times 10^4$	Γ1R3	Γ2R3	Γ3R3	Γ4R3	
$Re_s = 4.6 \times 10^4$	Γ1R4				
$Re_s = 5.5 \times 10^4$				Γ4R5	Γ5R5

Figure 6.2: Schematic showing the water level in the gap of the tall and short Taylor-Couette cylinders with the resulting aspect ratios, Γ, as well as the shear Reynolds numbers, Re_s, studied. The labels for the considered cases are given in the table.

and indicates the range of the measurements. In addition, Figure 6.2 provides a schematic, summarizing and labelling all the cases considered for this study.

In our Taylor-Couette setup the water temperature cannot be actively controlled. Thus, to avoid significant changes in temperature during the measurements, the system was operated for a few hours until a stable temperature was reached before taking the measurements. Furthermore, the temperature was recorded at the start and at the end of each data set. Repeated experiments showed that the hysteresis always occurred over the same range of rotational numbers and with approximately the same magnitude, even if the temperature difference in these experiments for an individual set varied between 0°C to 2.2°C. Moreover, the range of rotational numbers for which hysteresis occurs spans only a limited part of the full range of a covered in each experiment, and the torque differences in the hysteresis loop were small. Therefore, the power supplied to the flow was nearly constant, and consequently we may assume that the temperature change is small during hysteresis. This is confirmed by separate measurements covering only the range of rotational numbers corresponding to the hysteresis loop, which showed temperature changes less than 0.5°C (compared to 2.2°C for the full range).

On the other hand, not only for each individual data set, but also for the combined data set for a certain flow case, approximately constant temperature conditions should be maintained. For that, we applied a threshold of 2.2°C on the temperature variation among the data sets for a particular flow case, and accordingly, we excluded the data that causes a temperature variation exceeding the threshold. This resulted in an overall deviation of less than 0.5% in the torque at $a = 1$, which is outside the hysteresis loop in all cases, where

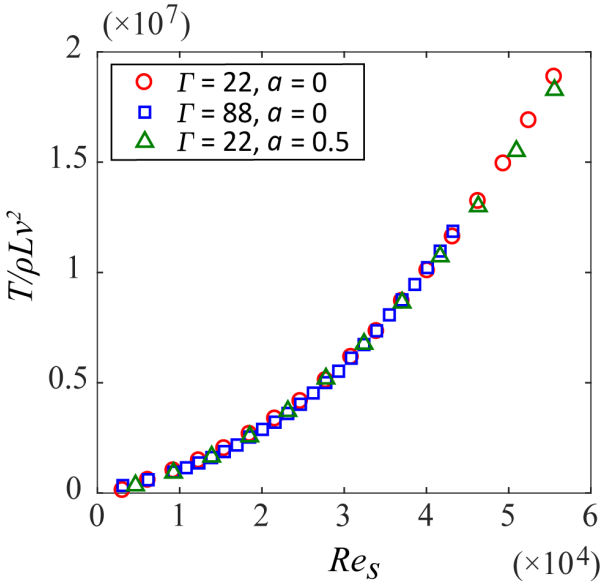

Figure 6.3: Corrected and normalized torque at different Re_s for the short cylinder ($\Gamma = 22$) and the taller cylinder ($\Gamma = 88$).

we expect the torque to return to the same value at the end of an experiment. Finally, as a result of this threshold, the temperature difference over the remaining sets varies between 0°C to 1.2°C.

The torque measurements were performed by means of a torque-meter (HBM T20WN, 2 Nm) attached to the inner cylinder shaft. Therefore, the measured torque contained contributions from the Taylor-Couette flow and the von Kármán flow. The latter flow state is the flow in the gap between the end plates which are rotating together with the inner and outer cylinders. The contribution of the von Kármán flow was determined for several shear Reynolds numbers, based on the study conducted by Greidanus *et al.* [40] in the same setup (their Figure 4 (*a*)). Accordingly, the torque values were corrected. After applying the correction, a very good agreement in the torque was found for both the shorter and taller cylinders at $a = 0$ and $a = 0.5$ (Figure 6.3). The corrected torque, T, before and after the laminar-turbulent flow transition follows a similar power law, *i.e.* $T \propto Re_s^{\alpha}$. In the turbulent flow regime, α is between 1.77 and 1.80 for the cases shown in Figure 6.3, which are in the range of previously reported values (*e.g* Wendt [128], Lathrop *et al.* [75], van Gils *et al.* [38]). The standard uncertainty of the mean torque for an individual data set, $\varepsilon_{mean} = \sigma_T/\sqrt{N}$, was also determined for each case studied. Here, σ_T is the standard deviation of the torque, and N is the number of independent samples (Adrian & Westerweel [2]). The uncertainty was found to be less than the magnitude of the hysteresis in the torque, ΔT, *i.e.* ($\varepsilon_{mean} \sim 10^{-2}\Delta T$), for all the cases considered. Further information about the setup and accuracy of the measurements (torque and stereo & tomo PIV) conducted in the same facility can be found in the studies of Ravelet *et al.* [101], Tokgöz [119] and Greidanus *et al.* [41].

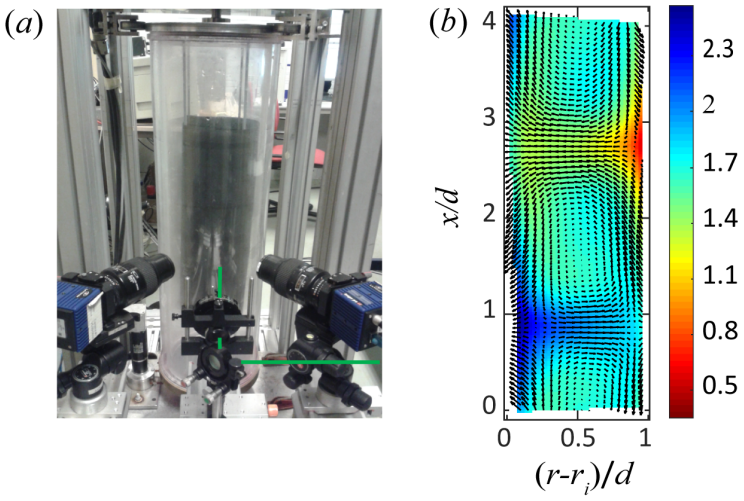

Figure 6.4: Stereo-PIV set-up with two high-resolution cameras (*a*). Green lines indicate the laser sheet. Sample mean velocity field (*b*). Arrows indicate the radial and axial velocities, while the azimuthal velocity (normalized by the outer cylinder velocity) is represented by colour coding.

In Figure 6.3, the corrected torque was normalized by $\rho L \nu^2$. However, all following torque data were normalized with the torque value, T_{ref}, obtained at $a = 0$ along the trajectory where a increases, which facilitates an easy comparison of the hysteresis loops at different flow conditions.

Finally, stereoscopic PIV measurements were conducted in the plane spanning the radial and the axial directions, which allowed examination of the large-scale flow structures. Fluorescent spheres (rhodamine B) with a mean diameter of 15 μm and a nominal density of 1.1 g/cm^3 were used as tracer particles. The tracers were illuminated by a double-pulsed Nd:YAG laser in a 1 mm thick light sheet, and the scattered light was recorded by two double-frame CCD cameras (Imager Pro LX 16M) in a stereoscopic configuration with a 90° angle between the viewing directions. The field of view was $4.09d \times 0.84d$, which was imaged onto 4872×1000 pixels. The time separation between the laser pulses was adjusted such that in each case the average particle image displacement is around 6 pixels. For each measurement, 800 image pairs, hence velocity fields, were obtained. The raw PIV images were processed with a commercial code (DAVIS 7.2 by LaVision GmbH). A multi-pass algorithm was applied with a final interrogation area of 32×32 pixels for the $a = 0$ and $a = 0.12$ cases, and 64×64 pixels for the $a = 0.22$ and $a = 0.4$ cases. The corresponding in-plane spatial resolution is $0.027d \times 0.027d$ and $0.054d \times 0.054d$, respectively, which is sufficient to capture the large-scale turbulent motions ($O(d)$) and the mean flow structures. Furthermore, a 50% overlap of adjacent interrogations was used for all cases. A picture showing the stereo-PIV setup and a sample velocity field is given in Figure 6.4 (*a*) and Figure 6.4 (*b*), respectively.

6.3 RESULTS AND DISCUSSIONS

6.3.1 TORQUE MEASUREMENTS

The effect of the shear Reynolds number, Re_s, on the hysteresis is investigated first. Figure 6.5 presents the measured torque for four different values of Re_s between 1.5×10^4 and 4.6×10^4 at an aspect ratio of 88. The lowest shear Reynolds number (Figure 6.5(A)) is around the laminar-turbulent transition Reynolds number, while the other shear Reynolds numbers correspond to the fully turbulent regime. The blue symbols represent measurements taken for decreasing a, while the red symbols represent for increasing a. The results clearly depict a hysteresis in the torque at all shear Reynolds numbers considered. The magnitude of the hysteresis in terms of the normalized torque depends on the shear Reynolds number. Moreover, a clear difference in the hysteresis behaviour is visible between the transitional case (Figure 6.5(A)) and the turbulent regime (Figures 5(B)-(D)). For the turbulent regime the torque values obtained for increasing a (red) are higher than the values obtained for the opposite trajectory, whereas the reverse is observed for the transition regime. In addition, for the turbulent cases, it can be seen that the hysteresis does not occur around the peak torque values, which is found to be the case in the study of Huisman *et al.* [55] (their Figure 3 (a)). This may be explained by the different radius ratio ($\eta = 0.716$ in their experiment, while $\eta = 0.917$ for the present data), which can cause some discrepancies in Taylor-Couette flow (Ravelet *et al.* [101], Brauckmann & Eckhardt [63], Ostilla-Mónico *et al.* [95]). Moreover, the torque in our Taylor-Couette system follows the same behaviour without any jump between the states, in contrast to the results of Huisman *et al.* [55]. Furthermore, as the shear Reynolds number increases, the range of frequency ratios a, for which the hysteresis is observed, shrinks.

Further torque measurements were conducted with different aspect ratios at a constant shear Reynolds number of $Re_s = 4.4 \times 10^4$. Different aspect ratios were achieved by changing the wetted surface of the cylinders; that is, changing the water level in the gap between the cylinders (see Figure 6.2). The contributions of the top and bottom von Kármán gaps were determined based on the torque obtained at $a = 1$ for all aspect ratios. Note that only in the $\Gamma = 88$ case, the top gap correction needs to be included, while the bottom gap contribution is corrected in all cases. The total gap contribution was found to be as the same as reported by Greidanus *et al.* [40], where a similar frequency ratio ($a = 0.917$) was considered. As can be seen in Figure 6.6, the hysteresis in the resulting torque becomes more pronounced as the aspect ratio increases. It is thus concluded that, as the confinement of the Taylor-Couette flow in the axial direction is reduced, *i.e.* Γ is increased, the hysteresis persists and becomes even more pronounced. It implies that the hysteresis does not result from confinement, but represents a genuine change in the turbulent flow state in the Taylor-Couette gap. Still, end wall conditions can potentially lead to significant changes in the large-scale meridional circulation, and consequently affect the shear boundary layer

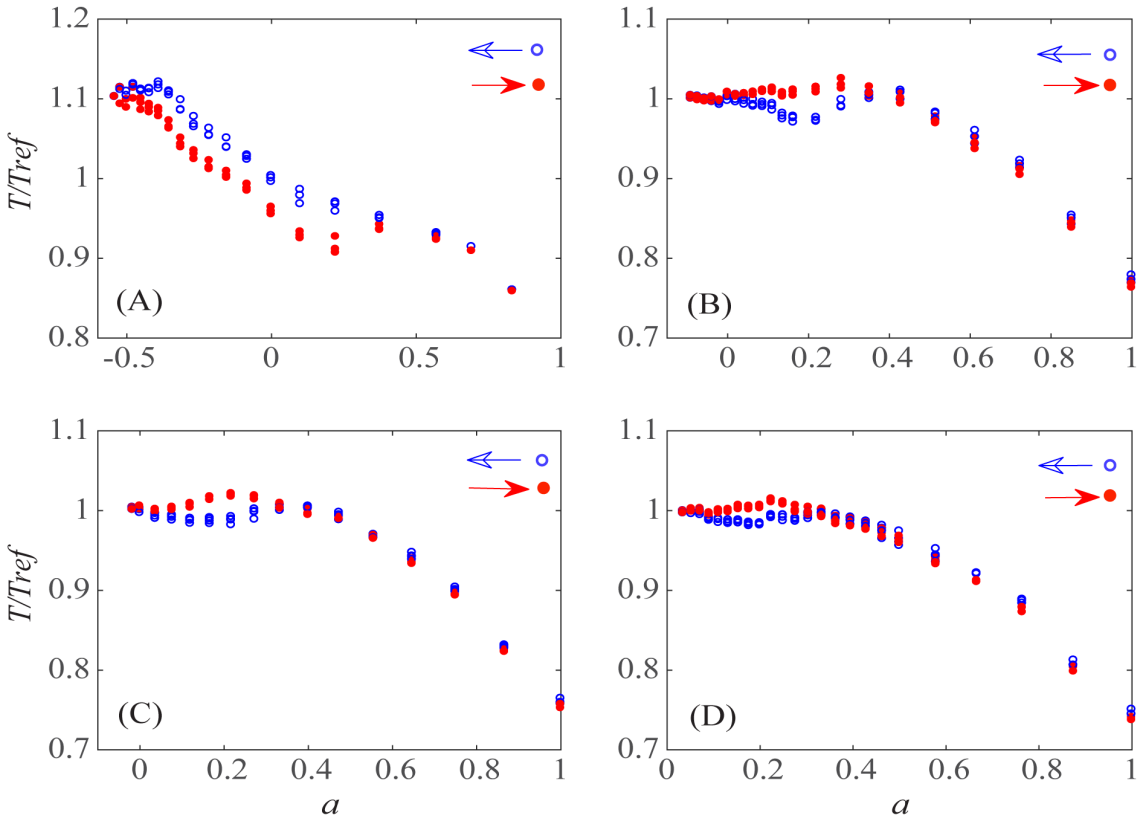

Figure 6.5: Hysteresis in the measured torque, T, at different constant shear Reynolds numbers (A) Γ1R1, $Re_s = 1.5 \times 10^4$, (B) Γ1R2, $Re_s = 3.7 \times 10^4$, (C) Γ1R3, $Re_s = 4.4 \times 10^4$ and (D) Γ1R4, $Re_s = 4.6 \times 10^4$ at an aspect ratio of $\Gamma = 88$. For cases (A) and (B) we show 3 data sets, and for cases (C) and (D) 4 data sets. Torque values are normalized by a reference value, T_{ref} (§6.2).

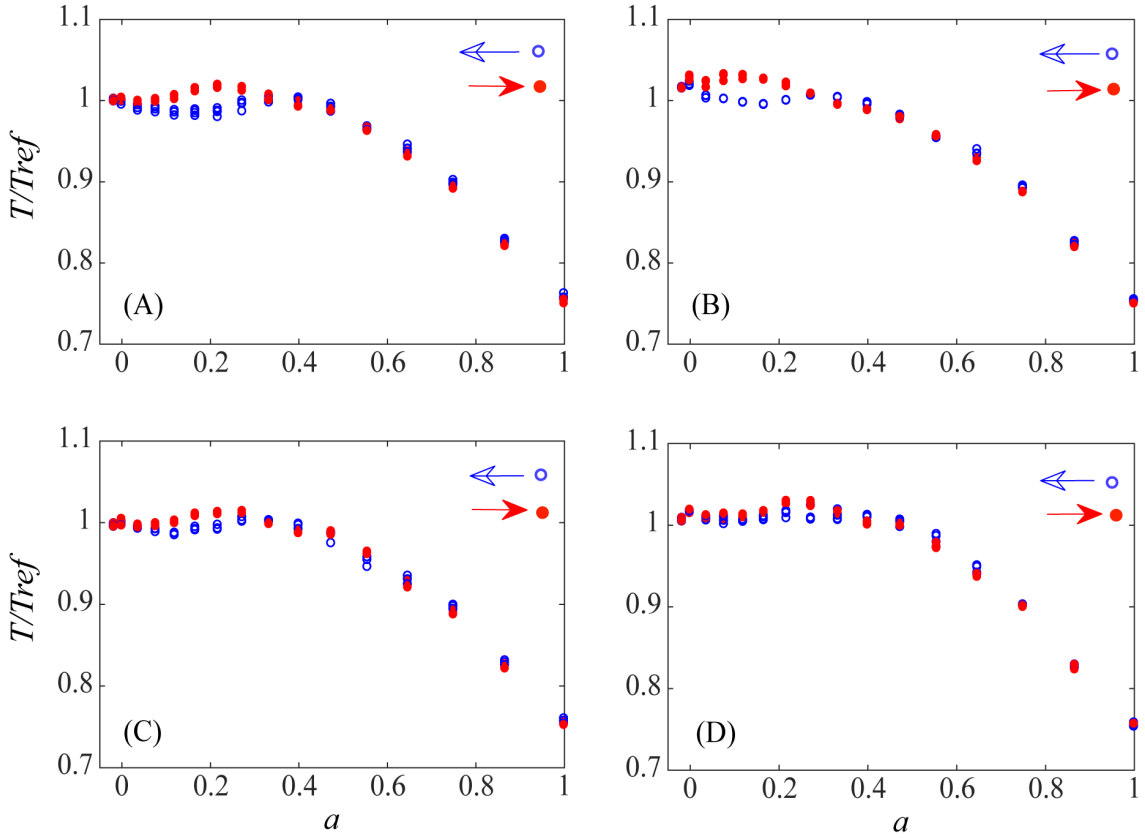

Figure 6.6: Torque hysteresis behaviour at different aspect ratios (A) Γ1R3, Γ = 88, (B) Γ2R3, Γ = 66, (C) Γ3R3, Γ = 44 and (D) Γ4R3, Γ = 22, at $Re_s = 4.4 \times 10^4$. Four data sets for cases (A) and (D), and three data sets for cases (B) and (C) are shown.

on the inner or outer cylinder (Avila *et al.* [7], Lopez [80], Lopez and Avila [81]). Hence, end effects and boundary conditions can affect the hysteresis, especially at low aspect ratio Γ, as discussed below.

Final torque measurements were performed in two different Taylor-Couette setups at the same aspect ratio, Γ = 22, and same shear Reynolds number, $Re_s = 5.5 \times 10^4$. In the shorter setup, the fluid is bounded both from the top and bottom with end plates, whereas in the taller setup it has a free surface at the top, therefore there is no von Kármán gap at the top. Here, a similar analysis was carried out taking into account the different torque contributions of the bottom and top gaps. The corrected and normalized results are presented in Figure 6.7. The measurements were conducted within a temperature range of 23.9 – 24.3°C for case A, and 25.5 – 25.9°C for case B. The maximum temperature change for each run is 0.4°C in both cases. When the two cases in Figure 6.7 are compared, it can be clearly seen that the hysteresis behaviour is different, although the hysteresis in the torque measurements occurs at the same value, $a \approx 0.4$. The hysteresis observed in the shorter set-up covers a shorter range, and inside this region the torque values are higher along the trajectory for decreasing a, which is found to be the reverse of the behaviour observed in the taller system. The resultant torque data for both configurations are in quanti-

tative agreement outside the hysteresis loop, which confirms the correct determination of the torque contribution from the von Kármán' gaps. Hence, all differences between these two systems seem to occur due to the different boundary conditions of the setups.

6.3.2 PIV MEASUREMENTS

After investigating the torque hysteresis, the associated flow structures were examined using the PIV measurements together with the proper orthogonal decomposition (POD) method (Lumley [82]). In particular we consider the case $Re_s = 4.4 \times 10^4$ and $\Gamma = 88$, Γ1R3, which is exemplary for hysteresis in the fully turbulent regime (§ 6.3.1). The average flow contains a large-scale periodic structure consisting of rolls (Figure 6.8 (A)). The wavelength of the rolls was determined based on the mean axial velocity field at four different values for a around the hysteresis region. Figure 6.8 (B) shows the resultant wavelengths normalized by the gap width. Again, blue and red symbols refer to the trajectories followed in the decreasing and increasing a direction, respectively. As is evident from Figure 6.8 (B), inside the hysteresis region the wavelengths of the structures are longer when the trajectory of the increasing a direction is followed (for the $a = 0.22$, $a = 0.12$, $a = 0$ cases). It should be noted that in these cases the torque is also larger along the same trajectory (Figure 6.5 (C)). For the $a = 0.4$ case, where there is no observable hysteresis in the torque data, the values of the wavelengths are the same to within the measurement uncertainty. Similar behaviour is observed in the experimental study of Huisman *et al.* [55] (their Figures 3 (*c*) and (*d*)). In addition, longer wavelengths of the structures would imply fewer rolls in the flow. Therefore, when the results of the wavelengths for the same a values are considered together with the torque results in Figure 6.5 (C), it can be seen that the torque values are higher in the presence of fewer rolls. This result is also in agreement with the findings of Martinez-Arias *et al.* [84] in the turbulent flow regime.

At the same conditions, the POD velocity modes were determined using the snapshot method of Sirovich [113]. The POD modes represent coherent structures, as explained by Lumley [82]. Since the modes are ordered according to their energy magnitude, the most energetic POD mode is the first mode, which often reveals large coherent structures if they exist in the flow. The plots of the axial velocity component of the first mode are presented in Figure 6.9. Note that for visualisation purposes and easy comparison, the ranges of all the colour bars are kept similar except for the data of cases (B) and (C) along the trajectory for increasing a. In Figure 6.9 (D), which corresponds to the case outside the hysteresis region, no significant change (quantitatively) in the flow structures as well as the energy content is observed. On the other hand, in the other two cases (B) and (C), which both occur within the hysteresis loop, it can be seen that the flow structures change significantly, becoming more dispersed along the trajectory for increasing a. Also, a significant decrease in the amplitude of the axial velocity is clearly visible when following the trajectory for increasing a. For case (A), there are changes in the flow structures and in the magnitudes

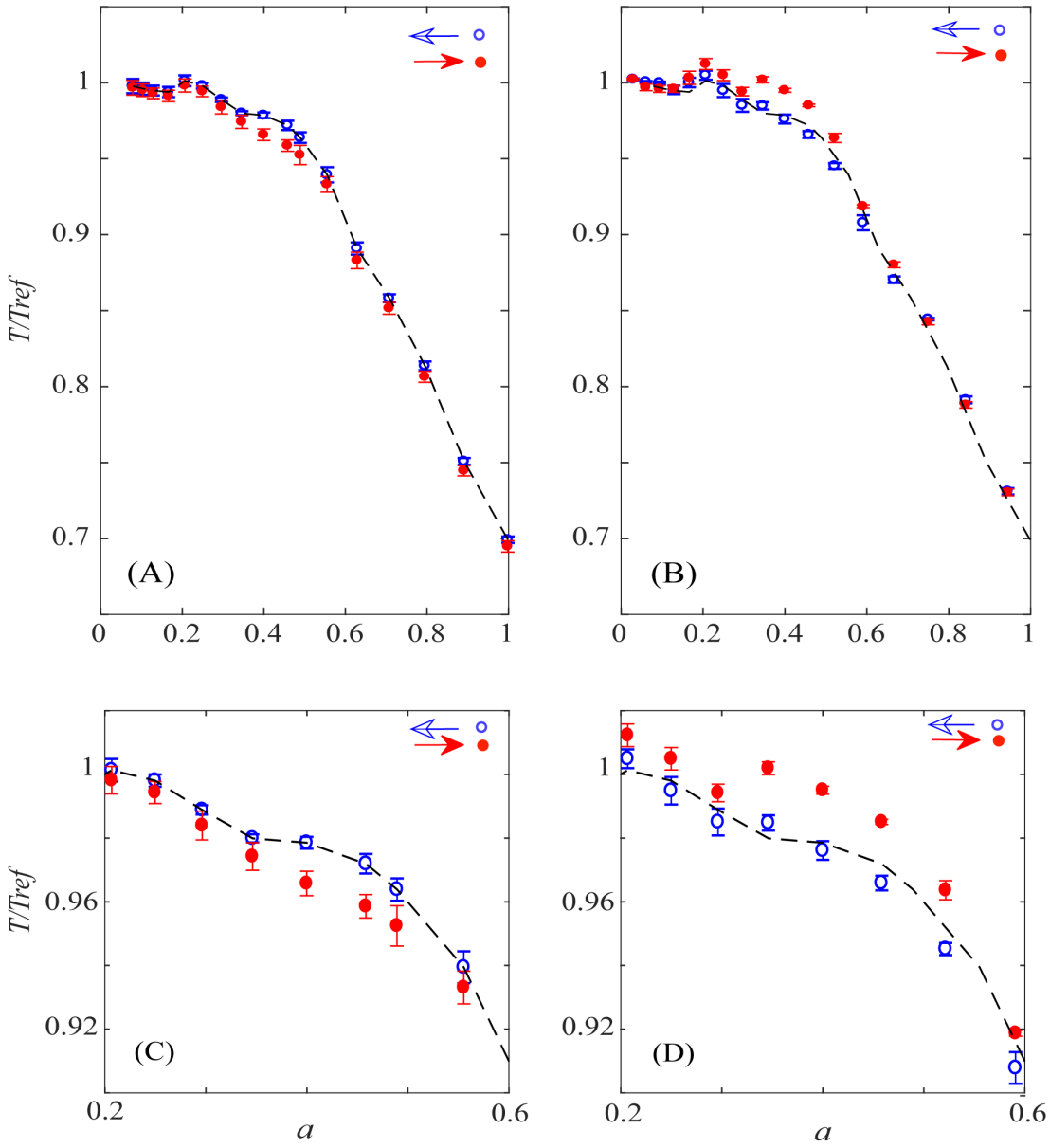

Figure 6.7: Torque hysteresis for two different Taylor–Couette (TC) set-ups, with aspect ratio $\Gamma = 22$ and shear Reynolds number $Re_s = 5.5 \times 10^4$. (A) Shorter TC set-up with two end plates, Γ5R5. (B) Tall TC set-up with bottom end plate and top free surface, Γ4R5. The black dashed line in (A) is a fitted torque curve along the trajectory for decreasing a for the Γ5R5 case, and it is duplicated in (B) for comparison. The error bars show the uncertainty in the repeatability. Panels (C) and (D) are the close-up views of the hysteresis regions of (A) and (B), respectively.

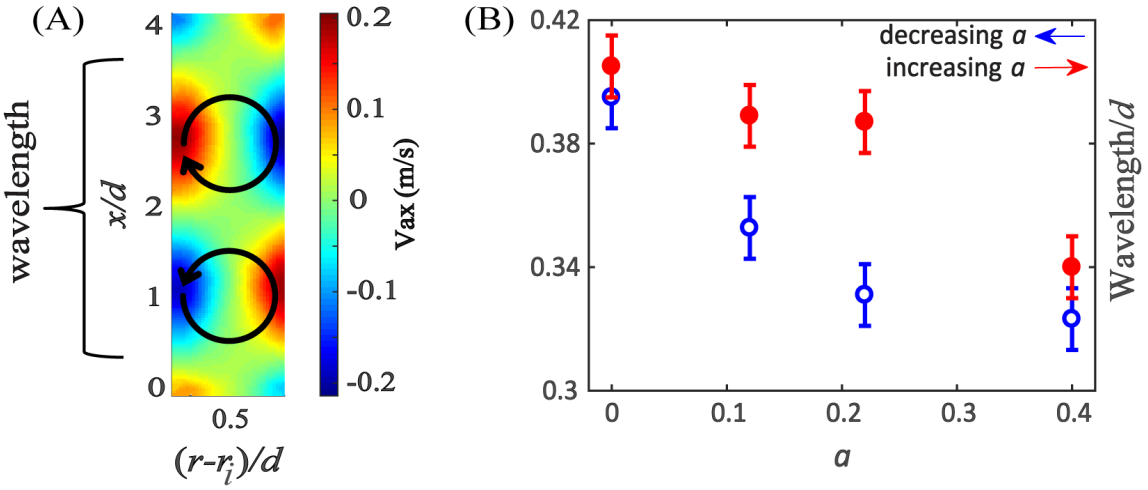

Figure 6.8: (A) Mean velocity field of the axial velocity component and (B) normalized wavelengths of the patterns together with reading errors. The black arrows schematically illustrate the rolls and flow direction.

for axial velocity, but these changes are not as pronounced as for the previous two cases. Similar results were found when the radial and azimuthal velocity components of the first mode are analysed, although for brevity these results are not included in this paper. Hence, it can be concluded that large coherent structures exist in the turbulent flow at this shear Reynolds number, and with the occurrence of the hysteresis in the flow, the effect of following different trajectories at the same flow conditions shows up both quantitatively and qualitatively in the most dominant flow structures. This suggests that a genuine change in the flow dynamics and therefore different flow states occur inside the hysteresis region when different trajectories are followed.

6.4 CONCLUSIONS

Measurements of the torque and of the instantaneous flow fields (using PIV) were performed to study the hysteresis in the measured torque in a Taylor-Couette system with a radius ratio of 0.917 and aspect ratios of 22 to 88.

In the first part of the study, torque measurements were carried out for different shear Reynolds numbers and at different aspect ratios. The results for the torque show that the magnitude of the hysteresis decreases at higher shear Reynolds numbers, whereas it is increasing with increasing aspect ratio. This indicates that the observed hysteresis could be the result of multiple turbulent states, and not due to the confinement of the flow. On the other hand, the resultant torque measurements obtained in two different Taylor-Couette configurations at the same shear Reynolds number and same aspect ratio show different behaviour, which illustrates the relevance of different boundary conditions.

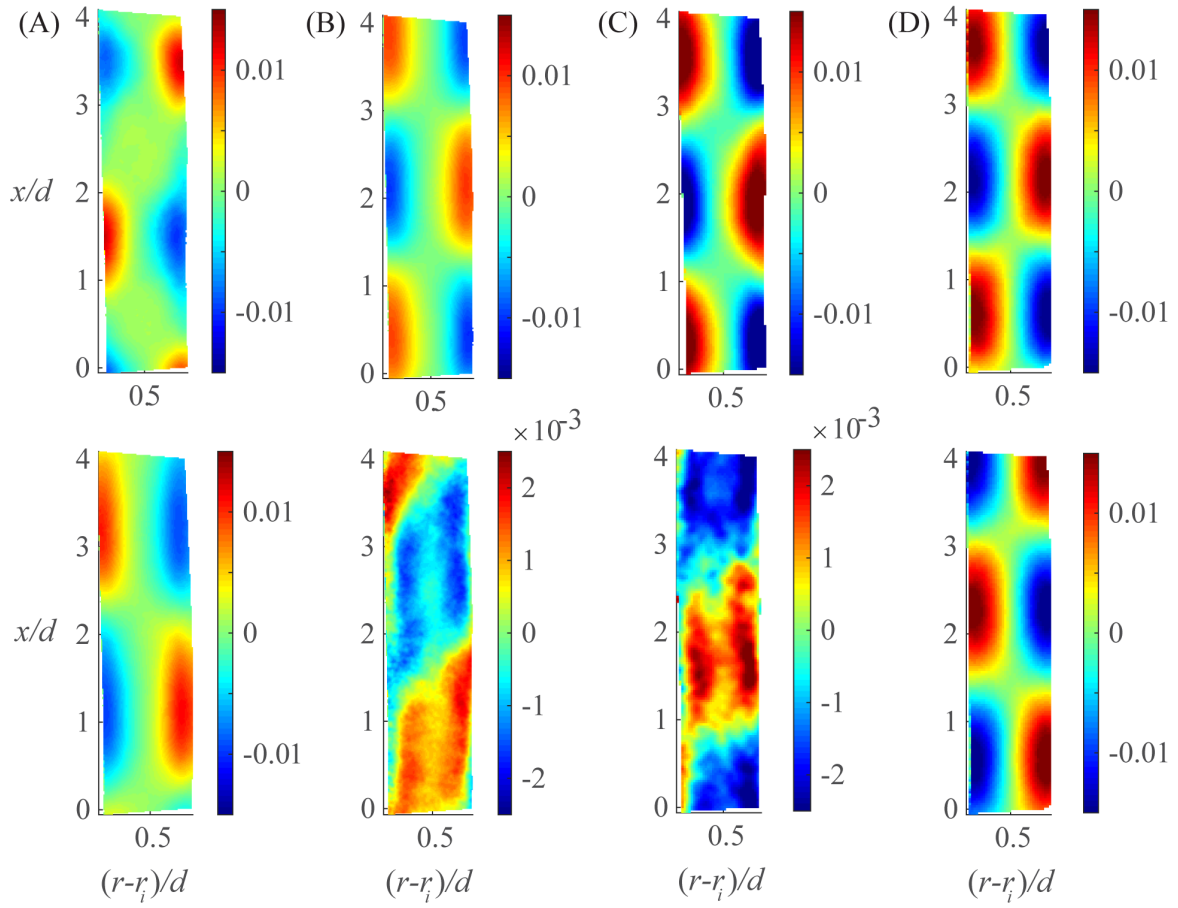

Figure 6.9: First POD mode of the axial velocity component at: (A) $a = 0$, (B) $a = 0.12$, (C) $a = 0.22$ and (D) $a = 0.4$. The top and bottom rows represent the results along the trajectory for decreasing and increasing a, respectively.

Stereoscopic-PIV measurements were performed and the axial wavelength of the structures were determined based on the mean axial velocity field. It was observed that the wavelength, and therefore the number of the rolls along the height of the Taylor Couette gap, changes inside the hysteresis region depending on the direction of the trajectory followed for the frequency ratio a. It was found that the torque values along the trajectory for increasing a are larger inside the hysteresis region where also the wavelengths of the structures are longer. Similarly, the axial velocity component of the first mode shows how the dominant flow structures respond to a change in the measurement direction when hysteresis occurs. With these results it can be concluded that the signature of different turbulent states observed in the behaviour of the torque is also visible in the flow structures.

7

SUMMARY AND OUTLOOK

7.1 SUMMARY

As stated in Chapter 1, this thesis aims to contribute to the physical understanding and the conceptual picture of wall turbulence. In this context, an experimental investigation with stereoscopic PIV was conducted in a turbulent pipe flow and in turbulent Taylor-Couette flow. For the latter study, additionally, torque measurements were performed to investigate the hysteresis behaviour of the flow as well as the behaviour of the associated dominant large-scale motions. For the Taylor-Couette flow, the study covers only the statistically steady flow conditions. The pipe flow study, on the other hand, consists of statistically steady turbulent flow conditions as well as unsteady flows, which are either accelerating or decelerating monotonically between two different turbulent states. Large scale coherent motions and the intense shear regions bounding them are the main structures investigated in the turbulent pipe flow.

The two point correlation analysis conducted in a statistically steady turbulent pipe flow showed large positively correlated regions, that are surrounded by anti-correlated regions. These type of structures suggest the presence of counter rotating streamwise vortex pairs. The average spanwise width and streamwise length of the correlation peaks were found to be $\sim 0.33R$ and $\sim 5R$, respectively, in the log layer for all the steady flow conditions considered in this thesis. Up to a wall distance of $y/R = 0.4$, these structures were observed to become wider in the spanwise direction and longer in the streamwise direction with the wall distance. Beyond $y/R = 0.4$, on the other hand, the widths of the correlation peaks stay similar while their streamwise lengths decrease with the wall distance. Moreover, when different steady flow conditions in the range $Re_\tau = 340 - 1259$ are compared, the spanwise width of the correlation peaks was found to be similar for the higher Reynolds number cases ($Re_\tau \geq 752$) at each wall normal location. For the lower Reynolds numbers, significant deviations were observed beyond $y/R = 0.4$, where the correlation peaks became wider. Similar types of averaged structures (*i.e.* correlations) were also found in the ramp-type accelerating/decelerating turbulent flows considered in this thesis. The streamwise length of the correlation peaks remained the same as in the initial turbulent state during the acceleration/deceleration. Nevertheless, the peaks were found to become wider in the spanwise direction during the deceleration, while their spanwise width is observed to decrease towards the end of the acceleration.

Large scale coherent motions are also visible in the instantaneous velocity fields of wall turbulence, forming regions of nearly uniform streamwise velocities (UMZs). Previous studies, mainly in turbulent boundary layers (TBLs), have shown that these UMZs are bounded by thin highly sheared dissipative regions similar to the turbulent/non-turbulent interfaces (TNTIs). These studies were dealing exclusively with the 2D signatures of shear layers. However, in this thesis, the 3D signature of these structures was provided employing a 3D detection method for the layers in a turbulent pipe flow. It could be seen that the shear layers have a certain finite length in the spanwise direction as well as in the streamwise direction, and bound regions of nearly uniform velocity. The average stream-

wise length of these layers was found to be similar to the streamwise length of the average large scale motions, which were determined by two-point correlations. Moreover, the 3D average flow field conditioned on the wall normal centres of the shear layers revealed a strong low speed region beneath the averaged shear layers, that is associated with strong positive wall-normal velocity fluctuations. Also, this low speed region was observed to be surrounded by two oppositely rotating swirling motions. The average shear layers, on the other hand, were stretched by two azimuthal motions having opposite signs. This average flow field around the shears support the link between the shear layers and hairpin structures. In the second part of this work, the shear layers were treated as the continuous interfaces of the UMZs detected following the approach of de Silva *et al.* [111], but using different orientation of the planes. While the shear layer detection method relies on the velocity gradients, which is the signature of small scale activity, the histogram approach is based on the instantaneous velocity information, *i.e.* large scale motions. It was found in this study that these two methods identify similar regions of intense shear where a step-like change in the streamwise velocity occurs. However, the 3D geometrical features of shear layers can be revealed with the former method only. Highly sheared regions were also identified during the accelerating/decelerating turbulent flows, revealing similar properties as those in steady flow conditions. It was found that the imposed unsteadiness does not affect significantly the geometry of the structures as well as the flow properties across them.

Finally, in a Taylor-Couette flow, the large scale motions were found to be non-unique, leading to different turbulent states at identical flow conditions (*i.e.* shear Reynolds numbers) for a certain range of rotational frequency ratios of the inner and outer cylinders, a. Within the same range of a, the resulting torque values, too, were observed to differ from each other with the change in the flow structures. Although the stereo-PIV and the torque measurements with different aspect ratios of the system revealed that the occurrence of the hysteresis in the present Taylor-Couette system is associated to a genuine change in the flow, still, the aspect ratio as well as the boundary conditions of the system were found to affect the behaviour and the magnitude of this phenomenon. Moreover, it was observed that the hysteresis is more pronounced at lower shear Reynolds numbers.

7.2 OUTLOOK

According to the classical picture of turbulence, the turbulent kinetic energy contained in the large scales is transferred down to the smaller scales, and finally via the viscosity, the energy is dissipated at the smallest scales of turbulence (Richardson [103], Kolmogorov [70]). However, supporting the pioneering arguments of Batchelor and Townsend [12], studies by Yeung *et al.* [133] and Shen & Warhaft [108] showed that this energy transfer can also happen in a single step process without intermediate steps. In addition to this 'forward' energy transfer, a significant transfer of the energy between the scales is also known

to occur 'backward', *i.e.* from the small scales to larger scales, known as 'backscatter' (Pope [99], Aoyama *et al.* [5]). Moreover, the amplitude and the frequency of the small scales was reported to be affected by the large scales (*e.g.* Hutchins and Marusic [59], Mathis *et al.* [87], Ganapathisubramani *et al.* [37]), questioning the postulations of Kolmogorov [70]. So, to gain further understanding about the possible interactions between the small and large scales of turbulence as well as the mechanism of the direct energy transfer between them, it is of interest to investigate the flow dynamics near the detected shear layers, which are dominated by small scale activities occurring between large scale energetically significant motions.

Comparable interfacial layers similar to the internal shear layers have been known to exist also between turbulent/non-turbulent interfaces (TNTI), which has been studied basically in turbulent jet flows and TBLs (*e.g.* Westerweel *et al.* [129], Borrell & Jiménez [16], Eisma *et al.* [32]). As reported by Eisma *et al.* [32], internal shear layers and TNTIs have very similar characteristics in a TBL. These type of interfaces (both TNTIs and internal shear layers) can be further investigated with generating puffs and slugs in a pipe flow. These studies can also reveal information about the mechanism on how these shear layers evolve. Another interesting topic for the internal shear layers is to investigate their scaling, such as their length scales and the scale of the changes in the flow properties across them. For that, data at higher Reynolds numbers with good spatial resolution is needed. How these shear layer properties (*e.g.* thickness of the layers and the magnitude of the jumps in the flow quantities across them) are determined also plays a key role.

So far, the main focus of turbulence studies has been the equilibrium state. Therefore, very little is known about the nature of the non-equilibrium state of turbulence. In the present thesis, a preliminary investigation of unsteady turbulent flow via accelerating/decelerating turbulent pipe flow was conducted. However, in the present study, it was observed that the degree of imposed unsteadiness is not enough to cause a significant change of the structures during the acceleration or deceleration. To increase the unsteadiness, either the acceleration/deceleration between the initial and the final Reynolds numbers should occur faster, or the ratio of these Reynolds numbers should increase while keeping the same ramping time. With the current pipe flow facility, the main limitation was related to the capacity of the centrifugal pump of the facility, which was not capable of handling rapid changes in the flow rate. To achieve this in the same pipe facility, either the centrifugal pump should be replaced by a gear pump, which can handle the transition between these two Reynolds numbers in a shorter time, or another valve system should be added to the set-up such that rapid changes in the mass flow rate can be achieved. On the other hand, while doing this, one should be careful about the water hammer phenomenon to avoid damaging the facility.

For the present Taylor-Couette flow, because of the limitations of the experimental set-up, experiments at higher shear Reynolds numbers (*e.g.* $Re_s \geq 10^5$) could not be achieved. Although the hysteresis phenomenon (*i.e.* multiple turbulent states) was already reported to exist at the shear Reynolds numbers of the order of 10^6 by Huisman *et al.* [55], the

flow is not statistically steady in their measurements. Also, previous studies (*e.g.* Ravelet *et al.* [101] and Brauckmann & Eckhardt [63]), including the present study, showed that different set-ups with different radius ratios could cause differences in the behaviour of the flow. Therefore, it is still an open question if the hysteresis in the torque also exists at very high shear Reynolds numbers in the current set-up. Apart from the hysteresis behaviour, Taylor-Couette flow is of interest to further investigate the characteristics of internal shear layers in canonical wall bounded flows.

REFERENCES

[1] R. J. Adrian, C. D. Meinhart, and C. D. Tomkins. "Vortex organization in the outer region of the turbulent boundary layer." In: *Journal of Fluid Mechanics* 422 (2000), 1–54.

[2] R. J. Adrian and J. Westerweel. *Particle Image Velocimetry*. Cambridge University Press, 2011.

[3] J. Ahn, J. H. Lee, J. Lee, J.-hoon Kang, and H. J. Sung. "Direct numerical simulation of a 30R long turbulent pipe flow at $Re\tau = 3008$." In: *Physics of Fluids* 27.6 (2015), p. 065110.

[4] C. D. Andereck, S. S. Liu, and Harry L. Swinney. "Flow regimes in a circular Couette system with independently rotating cylinders." In: *Journal of Fluid Mechanics* 164 (1986), 155–183.

[5] T. Aoyama, T. Ishihara, Y. Kaneda, M. Yokokawa, K. Itakura, and A. Uno. "Statistics of Energy Transfer in High-Resolution Direct Numerical Simulation of Turbulence in a Periodic Box." In: *Journal of the Physical Society of Japan* 74.12 (2005), pp. 3202–3212.

[6] C. Ariyaratne, S. He, and A. E. Vardy. "Wall friction and turbulence dynamics in decelerating pipe flows." In: *Journal of Hydraulic Research* 48 (2010), pp. 810–821.

[7] M. Avila, M. Grimes, J. M. Lopez, and F. Marques. "Global endwall effects on centrifugally stable flows." In: *Physics of Fluids* 20 (2008), p. 104104.

[8] A. Awasthi and W. Anderson. "Numerical study of turbulent channel flow perturbed by spanwise topographic heterogeneity: Amplitude and frequency modulation within low- and high-momentum pathways." In: *Phys. Rev. Fluids* 3 (2018), p. 044602.

[9] W. J. Baars, N. Hutchins, and I. Marusic. "Reynolds number trend of hierarchies and scale interactions in turbulent boundary layers." In: *Philosophical transactions. Series A, Mathematical, physical, and engineering sciences* 375 (2017).

[10] S. C. C. Bailey, M. Hultmark, A. J. Smits, and M. P. Schultz. "Azimuthal structure of turbulence in high Reynolds number pipe flow." In: *Journal of Fluid Mechanics* 615 (2008), 121–138.

[11] B. J Balakumar and R. J Adrian. “Large- and very-large-scale motions in channel and boundary-layer flows.” In: *Philosophical Transactions of the Royal Society of London A: Mathematical, Physical and Engineering Sciences* 365 (2007), pp. 665–681.

[12] G. K. Batchelor and A. A. Townsend. “The nature of turbulent motion at large wave-numbers.” In: *Proceedings of the Royal Society of London A: Mathematical, Physical and Engineering Sciences* 199.1057 (1949), pp. 238–255.

[13] M. Bilson and K. Bremhorst. “Direct numerical simulation of turbulent Taylor–Couette flow.” In: *Journal of Fluid Mechanics* 579 (2007), 227–270.

[14] R. F. Blackwelder and L. S. G. Kovasznay. “Time Scales and Correlations in a Turbulent Boundary Layer.” In: *The Physics of Fluids* 15.9 (1972), pp. 1545–1554.

[15] H. Blasius. *Das Aehnlichkeitsgesetz bei Reibungsvorgängen in Flüssigkeiten*. Springer Berlin Heidelberg, 1913, pp. 1–41.

[16] G. Borrell and J. Jiménez. “Properties of the turbulent/non-turbulent interface in boundary layers.” In: *Journal of Fluid Mechanics* 801 (2016), 554–596.

[17] P. Bradshaw. “‘Inactive’ motion and pressure fluctuations in turbulent boundary layers.” In: *Journal of Fluid Mechanics* 30 (1967), 241–258.

[18] H. J. Brauckmann and B. Eckhardt. “Direct numerical simulations of local and global torque in Taylor–Couette flow up to Re = 30 000.” In: *Journal of Fluid Mechanics* 718 (2013), 398–427.

[19] B. Brunone and A. Berni. “Wall Shear Stress in Transient Turbulent Pipe Flow by Local Velocity Measurement.” In: *Journal of Hydraulic Engineering-asce-J* 136 (2010).

[20] K. J. Bullock, R. E. Cooper, and F. H. Abernathy. “Structural similarity in radial correlations and spectra of longitudinal velocity fluctuations in pipe flow.” In: *Journal of Fluid Mechanics* 88 (1978), 585–608.

[21] T. A. Casey, J. Sakakibara, and S. T. Thoroddsen. “Scanning tomographic particle image velocimetry applied to a turbulent jet.” In: *Physics of Fluids* 25 (2013), p. 025102.

[22] K. Chauhan, J. Philip, C. M. de Silva, N. Hutchins, and I. Marusic. “The turbulent/non-turbulent interface and entrainment in a boundary layer.” In: *Journal of Fluid Mechanics* 742 (2014), 119–151.

[23] K. S. Choi, J. R. Debisschop, and B. R. Clayton. “Turbulent Boundary-Layer Control by Means of Spanwise-Wall Oscillation.” In: *AIAA Journal* 36 (1998), pp. 1157–1163.

[24] K. T. Christensen and R. J. Adrian. “Statistical evidence of hairpin vortex packets in wall turbulence.” In: *Journal of Fluid Mechanics* 431 (2001), 433–443.

[25] D. J. C. Dennis and T. B. Nickels. "On the limitations of Taylor's hypothesis in constructing long structures in a turbulent boundary layer." In: *Journal of Fluid Mechanics* 614 (2008), 197–206.

[26] D. J. C. Dennis and T. B. Nickels. "Experimental measurement of large-scale three-dimensional structures in a turbulent boundary layer. Part 1. Vortex packets." In: *Journal of Fluid Mechanics* 673 (2011), 180–217.

[27] S. Dong. "Direct numerical simulation of turbulent Taylor–Couette flow." In: *Journal of Fluid Mechanics* 587 (2007), 373–393.

[28] S. Dong. "Turbulent flow between counter-rotating concentric cylinders: a direct numerical simulation study." In: *Journal of Fluid Mechanics* 615 (2008), 371–399.

[29] C. W. H. van Doorne and J. Westerweel. "Measurement of laminar, transitional and turbulent pipe flow using Stereoscopic-PIV." In: *Experiments in Fluids* 42 (2007), 259–279.

[30] A. A. Draad. "Laminar-Turbulent Transition in Pipe Flow for Newtonian and non-Newtonian fluids." PhD thesis. Delft University of Technology, 1996.

[31] B. Dubrulle, O. Dauchot, F. Daviaud, P. Y. Longaretti, D. Richard, and J. P. Zahn. "Stability and turbulent transport in Taylor–Couette flow from analysis of experimental data." In: *Physics of Fluids* 17 (2005).

[32] J. Eisma, J. Westerweel, G. Ooms, and G. E. Elsinga. "Interfaces and internal layers in a turbulent boundary layer." In: *Physics of Fluids* 27 (2014).

[33] G. E. Elsinga, R. J. Adrian, B. W. Oudheusden, and F. Scarano. "Three-dimensional vortex organization in a high-Reynolds-number supersonic turbulent boundary layer." In: *Journal of Fluids Mechanics* 644 (2010), 35–60.

[34] G. E. Elsinga, T. Ishihara, M. V. Goudar, C. B. da Silva, and J. C. R. Hunt. "The scaling of straining motions in homogeneous isotropic turbulence." In: *Journal of Fluid Mechanics* 829 (2017), 31–64.

[35] B. Ganapathisubramani, K. Lakshminarasimhan, and N. T. Clemens. "Determination of complete velocity gradient tensor by using cinematographic stereoscopic PIV in a turbulent jet." In: *Experiments in Fluids* 42 (2007), pp. 923–939.

[36] B. Ganapathisubramani, E. K. Longmire, and I. Marusic. "Characteristics of vortex packets in turbulent boundary layers." In: *Journal of Fluid Mechanics* 478 (2003), 35–46.

[37] B. Ganapathisubramani, N. Hutchins, J. P. Monty, D. Chung, and I. Marusic. "Amplitude and frequency modulation in wall turbulence." In: *Journal of Fluid Mechanics* ().

[38] D. P. M. van Gils, S. G. Huisman, G.-W. Bruggert, C. Sun, and D. Lohse. "Torque Scaling in Turbulent Taylor-Couette Flow with Co- and Counterrotating Cylinders." In: *Phys. Rev. Lett.* 106 (2011), p. 024502.

[39] H. L. Grant. "The large eddies of turbulent motion." In: *Journal of Fluid Mechanics* 4 (1958), 149–190.

[40] A. J. Greidanus, R. Delfos, and J. Westerweel. "Drag reduction by surface treatment in turbulent Taylor-Couette flow." In: *Journal of Physics: Conference Series* 318 (2011), p. 082016.

[41] A. J. Greidanus, R. Delfos, S. Tokgoz, and J. Westerweel. "Turbulent Taylor-Couette flow over riblets: drag reduction and the effect of bulk fluid rotation." In: *Experiments in Fluids* 56 (2015), p. 107.

[42] S. Grossmann, D. Lohse, and C. Sun. "High–Reynolds Number Taylor-Couette Turbulence." In: *Annual Review of Fluid Mechanics* 48 (2016), pp. 53–80.

[43] M. Guala, S. E. Hommema, and R. J. Adrian. "Large-scale and very-large-scale motions in turbulent pipe flow." In: *Journal of Fluid Mechanics* 554 (2006), 521–542.

[44] M. Guala, M. Metzger, and B. J. McKeon. "Interactions within the turbulent boundary layer at high Reynolds number." In: *Journal of Fluid Mechanics* 666 (2011), 573–604.

[45] M. Gul, G. E. Elsinga, and J. Westerweel. "Experimental investigation of torque hysteresis behaviour of Taylor–Couette Flow." In: *Journal of Fluid Mechanics* 836 (2018), 635–648.

[46] A. K. Gupta, J. Laufer, and R. E. Kaplan. "Spatial structure in the viscous sublayer." In: *Journal of Fluid Mechanics* 50 (1971), 493–512.

[47] S. He, C. Ariyaratne, and A. E. Vardy. "Wall shear stress in accelerating turbulent pipe flow." In: *Journal of Fluid Mechanics* 685 (2011), 440–460.

[48] S. He, C. Ariyaratne, and A.E. Vardy. "A computational study of wall friction and turbulence dynamics in accelerating pipe flows." In: *Computers & Fluids* 37 (2008), pp. 674 –689.

[49] S. He and J. D. Jackson. "A study of turbulence under conditions of transient flow in a pipe." In: *Journal of Fluid Mechanics* 408 (2000), 1–38.

[50] S. He and J. D. Jackson. "An experimental study of pulsating turbulent flow in a pipe." In: *European Journal of Mechanics B, Fluids* 28 (2009), pp. 309–320.

[51] S. He and M. Seddighi. "Turbulence in transient channel flow." In: *Journal of Fluid Mechanics* 715 (2013), 60–102.

[52] S. He and M. Seddighi. "Transition of transient channel flow after a change in Reynolds number." In: *Journal of Fluid Mechanics* 764 (2015), 395–427.

[53] M. R. Head and P. Bandyopadhyay. “New aspects of turbulent boundary-layer structure.” In: *Journal of Fluid Mechanics* 107 (1981), 297–338.

[54] K. Horiuti and Y. Takagi. “Identification method for vortex sheet structures in turbulent flows.” In: *Physics of Fluids* 17 (2005), p. 121703.

[55] S. G. Huisman, R. C.A. van der Veen, C. Sun, and D. Lohse. “Multiple states in highly turbulent Taylor–Couette flow.” In: *Nature Communications* 5 (2011), p. 3820.

[56] S. G. Huisman, S. Scharnowski, C. Cierpka, C. J. Kähler, D. Lohse, and C. Sun. “Logarithmic Boundary Layers in Strong Taylor-Couette Turbulence.” In: *Phys. Rev. Lett.* 110 (2013), p. 264501.

[57] N. Hutchins, W. T. Hambleton, and I. Marusic. “Inclined cross-stream stereo particle image velocimetry measurements in turbulent boundary layers.” In: *Journal of Fluid Mechanics* 541 (2005), 21–54.

[58] N. Hutchins and I. Marusic. “Large-scale influences in near-wall turbulence.” In: *Philosophical Transactions of the Royal Society of London A* 365 (2001), pp. 647–664.

[59] N. Hutchins and I. Marusic. “Evidence of very long meandering features in the logarithmic region of turbulent boundary layers.” In: *Journal of Fluid Mechanics* 579 (2007), 1–28.

[60] J. Hwang and H. J. Sung. “Influence of large-scale motions on the frictional drag in a turbulent boundary layer.” In: *Journal of Fluid Mechanics* 829 (2017), 751–779.

[61] T. Ishihara, Y. Kaneda, and J. C. R. Hunt. “Thin Shear Layers in High Reynolds Number Turbulence-DNS Results.” In: *Flow, Turbulence and Combustion* 91 (2013), pp. 895–929.

[62] T. Ishihara, H. Ogasawara, and Julian C.R. Hunt. “Analysis of conditional statistics obtained near the turbulent/non-turbulent interface of turbulent boundary layers.” In: *Journal of Fluids and Structures* 53 (2015), pp. 50 –57.

[63] H. J. Brauckmann and B. Eckhardt. “Intermittent boundary layers and torque maxima in Taylor-Couette flow.” In: *Physical Review E.* 87 (2013), p. 033004.

[64] E. Jerke. “Pollutant dispersion in wall-bounded turbulent flows: an experimental assessment.” PhD thesis. Delft University of Technology, 2017.

[65] Y. Jodai and G. E. Elsinga. “Experimental observation of hairpin auto-generation events in a turbulent boundary layer.” In: *Journal of Fluid Mechanics* 795 (2016), 611–633.

[66] C. Kähler. “The significance of coherent flow structures for the turbulent mixing in wallbounded flows.” In: *Dissertation, DLR Forschungsbericht* (2004).

[67] K. C. Kim and R. J. Adrian. "Very large-scale motion in the outer layer." In: *Physics of Fluids* 11 (1999), pp. 417–422.

[68] S. J. Kline, W. C. Reynolds, F. A. Schraub, and P. W. Runstadler. "The structure of turbulent boundary layers." In: *Journal of Fluid Mechanics* 30 (), pp. 741–773.

[69] V. Kolář. "Vortex identification: New requirements and limitations." In: *Int. J. Heat Fluid Flow* 28 (2007), pp. 638–652.

[70] A. Kolmogorov. "The Local Structure of Turbulence in Incompressible Viscous Fluid for Very Large Reynolds' Numbers." In: *Akademiia Nauk SSSR Doklady* 30 (1941), pp. 301–305.

[71] A. G. Kravchenko, H. Choi, and P. Moin. "On the relation of near-wall streamwise vortices to wall skin friction in turbulent boundary layers." In: *Physics of Fluids A: Fluid Dynamics* 5 (1993), pp. 3307–3309.

[72] J. Kurokawa and M. Morikawa. "Accelerated and Decelerated Flows in a Circular Pipe : 1st Report, Velocity Profile and Friction Coefficient." In: *Bulletin of JSME* 29 (1986), pp. 758–765.

[73] Y. S. Kwon, J. Philip, C. M. de Silva, N. Hutchins, and J. P. Monty. "The quiescent core of turbulent channel flow." In: *Journal of Fluid Mechanics* 751 (2014), 228–254.

[74] A. Laskari, R. de Kat, R. J. Hearst, and B. Ganapathisubramani. "Time evolution of uniform momentum zones in a turbulent boundary layer." In: *Journal of Fluid Mechanics* 842 (2018), 554–590.

[75] D. P. Lathrop, J. Fineberg, and H. L. Swinney. "Transition to shear-driven turbulence in Couette-Taylor flow." In: *Phys. Rev. A* 46 (1992), pp. 6390–6405.

[76] J. H. Lee and H. J. Sung. "Comparison of very-large-scale motions of turbulent pipe and boundary layer simulations." In: *Physics of Fluids* 25 (2013), p. 045103.

[77] J. Lee, J. Ahn, and H. J. Sung. "Comparison of large- and very-large-scale motions in turbulent pipe and channel flows." In: *Physics of Fluids* 27 (2015).

[78] G. S. Lewis and H. L. Swinney. "Velocity structure functions, scaling, and transitions in high-Reynolds-number Couette-Taylor flow." In: *Phys. Rev. E* 59 (1999), pp. 5457–5467.

[79] Z. Liu, R. J. Adrian, and T. J. Hanratty. "Large-scale modes of turbulent channel flow: transport and structure." In: *Journal of Fluid Mechanics* 448 (2001), 53–80.

[80] J. M. Lopez. "Subcritical instability of finite circular Couette flow with stationary inner cylinder." In: *Journal of Fluid Mechanics* 793 (2016), 589–611.

[81] J. M. Lopez and M. Avila. "Boundary-layer turbulence in experiments on quasi-Keplerian flows." In: *Journal of Fluid Mechanics* 817 (2017), 21–34.

[82] J. L. Lumley. “The structure of inhomogeneous turbulent flow.” In: *Atmospheric Turbulence and Radio Wave Propagation (ed. A. M. Yaglom & V. I. Tatarski)* (1967), 166–178.

[83] Y. Maciel, M. Robitaille, and S. Rahgozar. “A method for characterizing cross-sections of vortices in turbulent flows.” In: *International Journal of Heat and Fluid Flow* 37 (2012), pp. 177–188.

[84] B. Martínez-Arias, J. Peixinho, O. Crumeyrolle, and I. Mutabazi. “Effect of the number of vortices on the torque scaling in Taylor–Couette flow.” In: *Journal of Fluid Mechanics* 748 (2014), 756–767.

[85] I. Marusic. “On the role of large-scale structures in wall turbulence.” In: *Physics of Fluids* 13 (2001), pp. 735–743.

[86] T. Maruyama, T. Kuribayashi, and T. Mizushina. “The Structure of the Turbulence in Transient Pipe Flows.” In: *Journal of Chemical Engineering of Japan* 9 (1976), pp. 431–439.

[87] R. Mathis, N. Hutchins, and I. Marusic. “Large-scale amplitude modulation of the small-scale structures in turbulent boundary layers.” In: *Journal of Fluid Mechanics* 628 (2009), 311–337.

[88] C. D. Meinhart and R. J. Adrian. “On the existence of uniform momentum zones in a turbulent boundary layer.” In: *JPhysics of Fluids* 7 (1995), pp. 694–696.

[89] T. Mizushina, T. Maruyama, and H. Hirasawa. “Structure of Turbulence in Pulsating Pipe Flows.” In: *Journal of Chemical Engineering of Japan* 8.3 (1975), pp. 210–216.

[90] J. P. Monty, J. A. Stewart, R. C. Williams, and M. S. Chong. “Large-scale features in turbulent pipe and channel flows.” In: *Journal of Fluid Mechanics* 589 (2007), 147–156.

[91] J. P. Monty, N. Hutchins, H. C. H. NG, I. Marusic, and M. S. Chong. “A comparison of turbulent pipe, channel and boundary layer flows.” In: *Journal of Fluid Mechanics* 632 (2009), 431–442.

[92] J. P. Monty, N. Hutchins, H. C. H. Ng, I. Marusic, and M. S. Chong. “A comparison of turbulent pipe, channel and boundary layer flows.” In: *Journal of Fluid Mechanics* 632 (2009), 431–442.

[93] J. A. Mullin and W. J. A. Dahm. “Dual-plane stereo particle image velocimetry measurements of velocity gradient tensor fields in turbulent shear flow. I. Accuracy assessments.” In: *Physics of Fluids* 18 (2006).

[94] R. Ostilla-Mónico, E. P. van der Poel, R. Verzicco, S. Grossmann, and D. Lohse. “Boundary layer dynamics at the transition between the classical and the ultimate regime of Taylor-Couette flow.” In: *Physics of Fluids* 26 (2014), p. 015114.

[95] R. Ostilla-Mónico, E. P. van der Poel, R. Verzicco, S. Grossmann, and D. Lohse. "Exploring the phase diagram of fully turbulent Taylor–Couette flow." In: *Journal of Fluid Mechanics* 761 (2014), 1–26.

[96] M. S. Paoletti and D. P. Lathrop. "Angular Momentum Transport in Turbulent Flow between Independently Rotating Cylinders." In: *Phys. Rev. Lett.* 106 (2011), p. 024501.

[97] A. E. Perry and C. J. Abell. "Scaling laws for pipe-flow turbulence." In: *Journal of Fluid Mechanics* 67 (1975), 257–271.

[98] A. E. Perry and M. S. Chong. "On the mechanism of wall turbulence." In: *Journal of Fluid Mechanics* 119 (1982), 173–217.

[99] S. B. Pope. *Turbulent Flows*. Cambridge University Press, 2000.

[100] M. Quadrio and S. Stefano. "Numerical simulation of turbulent flow in a pipe oscillating around its axis." In: *Journal of Fluid Mechanics* 424 (2000), 217–241.

[101] F. Ravelet, R. Delfos, and J. Westerweel. "Influence of global rotation and Reynolds number on the large-scale features of a turbulent Taylor–Couette flow." In: *Physics of Fluids* 22 (2010), p. 055103.

[102] O. Reynolds. "IV. On the dynamical theory of incompressible viscous fluids and the determination of the criterion." In: *Philosophical Transactions of the Royal Society of London A: Mathematical, Physical and Engineering Sciences* 186 (1895), pp. 123–164.

[103] L. F. Richardson. "Atmospheric diffusion shown on a distance-neighbour graph." In: *Proceedings of the Royal Society of London A: Mathematical, Physical and Engineering Sciences* 110.756 (1926), pp. 709–737.

[104] S K Robinson. "Coherent Motions in the Turbulent Boundary Layer." In: *Annual Review of Fluid Mechanics* 23 (1991), pp. 601–639.

[105] B. J. Saxton-Fox T.and McKeon. "Coherent structures, uniform momentum zones and the streamwise energy spectrum in wall-bounded turbulent flows." In: *Journal of Fluid Mechanics* 826 (2017), R6.

[106] W. Schoppa and F. Hussain. "Coherent structure generation in near-wall turbulence." In: *Journal of Fluid Mechanics* 453 (1983), 57–108.

[107] K.V. Sharp and R. J. Adrian. "PIV study of small-scale flow structure around a Rushton turbine." In: *AIChE J* 4 (2001), pp. 766–778.

[108] X. Shen and Z. Warhaft. "The anisotropy of the small scale structure in high Reynolds number turbulent shear flow." In: *Physics of Fluids* 12 (2000), pp. 2976–2989.

[109] J. Sheng, H. Meng, and R. O. Fox. "A large eddy PIV method for turbulence dissipation rate estimation." In: *Chem Eng Sci* 20 (2000), pp. 4423–4434.

[110] E. B. Shuy. "Wall shear stress in accelerating and decelerating turbulent pipe flows." In: *Journal of Hydraulic Research* 34 (1996), pp. 173–183.

[111] C. M. de Silva, N. Hutchins, and I. Marusic. "Uniform momentum zones in turbulent boundary layers." In: *Journal of Fluid Mechanics* 786 (2016), 309–331.

[112] C. M. de Silva, J. Philip, N. Hutchins, and I. Marusic. "Interfaces of uniform momentum zones in turbulent boundary layers." In: *Journal of Fluid Mechanics* 820 (2017), 451–478.

[113] L. Sirovich. "Turbulence and the dynamics of coherent structures. Part I. Coherent structures." In: *Quarterly of Applied Mathematics* 45 (1987), pp. 561–571.

[114] C. R. Smith and S. P. Metzler. "The characteristics of low-speed streaks in the near-wall region of a turbulent boundary layer." In: *Journal of Fluid Mechanics* 129 (1983), 27–54.

[115] S. F. Tardu, G. Binder, and R. F. Blackwelder. "Turbulent channel flow with large-amplitude velocity oscillations." In: *Journal of Fluid Mechanics* 267 (1994), 109–151.

[116] G. I. Taylor. "The Spectrum of Turbulence." In: *Proceedings of the Royal Society of London A: Mathematical, Physical and Engineering Sciences* 164 (1938), pp. 476–490.

[117] S. Tokgoz, G. E. Elsinga, R. Delfos, and J. Westerweel. "Experimental investigation of torque scaling and coherent structures in turbulent Taylor–Couette flow." In: *Journal of Physics: Conference Series* 318 (2011), p. 082018.

[118] S. Tokgoz, G. E. Elsinga, R. Delfos, and J. Westerweel. "Spatial resolution and dissipation rate estimation in Taylor–Couette flow for tomographic PIV." In: *Experiments in Fluids* 53 (2012), 561–583.

[119] S. Tokgöz. "Coherent Structures in Taylor-Couette Flow: Experimental Investigation." PhD thesis. Delft University of Technology, 2014.

[120] C. D. Tomkins and R. J. Adrian. "Spanwise structure and scale growth in turbulent boundary layers." In: *Journal of Fluid Mechanics* 490 (2003), 37–74.

[121] J. M. J. den Toonder and F. T. M. Nieuwstadt. "Reynolds number effects in a turbulent pipe flow for low to moderate Re." In: *Physics of Fluids* 9 (1997), pp. 3398–3409.

[122] A. A. Townsend. "The turbulent boundary layer." In: *Boundary Layer Research* (1958), 1–15.

[123] A. A. Townsend. "Equilibrium layers and wall turbulence." In: *Journal of Fluid Mechanics* 11 (1961), 97–120.

[124] A. A. Townsend. "The Structure of Turbulent Shear Flow." In: *Cambridge University Press* (1976).

[125] A. E. Vardy, J.M.B. Brown, and S. He. “Signs of unsteady friction.” In: *Proceedings of the ninth international conferences on pressure surges* 685 (2004), 493–507.

[126] R. Van der Veen, S. Huisman, O.-Y. Dung, H. L. Tang, C. Sun, and D. Lohse. “Exploring the phase space of multiple states in highly turbulent Taylor-Couette flow.” In: *Physical Review Fluids* 1 (2016), p. 024401.

[127] L. Wei, G. E. Elsinga, G. Brethouwer, P. Schlatter, and Johansson A. V. “Universality and scaling phenomenology of small-scale turbulence in wall-bounded flows.” In: *Flow, Turbulence and Combustion* 26 (2014).

[128] F. Wendt. “Turbulente Strömungen zwischen zwei rotierenden konaxialen Zylindern.” In: *Ingenieur-Archiv* 4 (1933), pp. 577–595.

[129] J. Westerweel, C. Fukushima, J. M. Pedersen, and J. C. R. Hunt. “Mechanics of the Turbulent-Nonturbulent Interface of a Jet.” In: *Phys. Rev. Lett.* 95 (2005), p. 174501.

[130] B. Wieneke. “Stereo-PIV using self-calibration on particle images.” In: *Experiments in Fluids* 39 (2005), 267–280.

[131] N. A. Worth and T. B. Nickels. “Some characteristics of thin shear layers in homogeneous turbulent flow.” In: *Philosophical Transactions of the Royal Society of London A: Mathematical, Physical and Engineering Sciences* 369.1937 (2011), pp. 709–722.

[132] X. Wu, J. R. Baltzer, and R. J. Adrian. “Direct numerical simulation of a 30R long turbulent pipe flow at R=685: large- and very large-scale motions.” In: *Journal of Fluid Mechanics* 698 (2012), 235–281.

[133] P. K. Yeung, James G. Brasseur, and Qunzhen Wang. “Dynamics of direct large-small scale couplings in coherently forced turbulence: concurrent physical- and Fourier-space views.” In: *Journal of Fluid Mechanics* 283 (1995), 43–95.

[134] J. Zhang, B. Tao, and J. Katz. “Turbulent flow measurement in a square duct with hybrid holographic PIV.” In: *Experiments in Fluids* 23 (1997), pp. 373–381.

[135] J. Zhou, R. J. Adrian, S. Balachandar, and T. M. Kendall. “Mechanisms for generating coherent packets of hairpin vortices in channel flow.” In: *Journal of Fluid Mechanics* 387 (1999), 353–396.

[136] J.G. Zhou, R. Adrian, and S. Balachandar. “Autogeneration of near wall vortical structure in channel flow.” In: *Physics of Fluids* 8 (1996), pp. 288–290.

[137] J. C. del Álamo and J. Jiménez. “Spectra of the very large anisotropic scales in turbulent channels.” In: *Physics of Fluids* 15 (2003), pp. L41–L44.

[138] J. C. del Álamo, J. Jiménez, P. Zandonade, and R. D. Moser. “Scaling of the energy spectra of turbulent channels.” In: *Journal of Fluid Mechanics* 500 (2004), 135–144.

[139] J. C. del Álamo, J. Jiménez, P. Zandonade, and R.D. Moser. “Self-similar vortex clusters in the turbulent logarithmic region.” In: *Journal of Fluid Mechanics* 561 (2006), 329–358.

ACKNOWLEDGMENTS

This thesis would not have been possible without the help of many people who supported and motivated me during these years.

First of all, I am sincerely grateful to my supervisors Prof. Dr. Jerry Westerweel and Dr. Gerrit E. Elsinga for giving me the opportunity of joining the Laboratory for Aero & Hydrodynamics at TU Delft and pursue this PhD project. I thank you for your professional guidance, support, advice and the freedom you have provided me in my research path.

As the experimentalists in the lab, I think we are lucky to be surrounded by outstanding technicians. So, I would like to thank Jasper Ruijgrok, Jan Graafland and Edwin Overmars for their technical support.

Special thanks go to Caroline Legierse, not only for her administrative support but also for her kindness, cheerfulness, friendship and for all the fun conversations we had in the lab. I would also like to thank Maria, Annette and Joost from FOM for their administrative support and fast response whenever I needed during my employment.

Big thanks go to Arati and Hema for their kindness, helpfulness and friendship in the lab.. I very much enjoyed the chats and all the events we had together. All were full of fun!

I would also like to thank Pepijn, Yuk Man, Mike, Andries and Tariq (chronologically) for the fun times and discussions we had in the office, as well as for their helpfulness.

I would like to extend my thanks to (in no order) Koen, Sedat, Manu, Soren, Florian, Pedro, Saad, Sita, Greta, Cenk, Daniele, Carlos, Jerke, Ernst Jan, Arnoud, Maurice, Norbert, Marieke, Ankur, Gem, Henke, Mohammad, Jasper Tomas, Amitosh, John, Wout, Willian, Dries, Guiermo, Parvis, Lee, Wim-Paul, Gijs Ooms, Villam de Water, Christian Poelma, Ellert, Christian Potma, Mark Tummers, René Delfos, Mathieu, Daniel Tam, Göktürk, Eduardo. I very much enjoyed working in the same lab with you.. also very much enjoyed the coffee breaks, lunches, movie nights, dinners, drinks, lab outings, barbecues, Christmas & New Year events that we had all together.. It was also very fun to be in the Panta Rhei board, and very nice coincidence for me personally to run across Heraclitus of Ephesus again. Well, with all these memories, the Aero-Hydro Lab and Delft will always occupy a very particular place in my life.

I would also like to thank all the people in the Women and Science intervisions. Especially, Sixue, Nicole and Susanna.. thank you very much for your support and the fruitful discussions we had in the last weeks of my PhD. Also, I would like to thank you Rosemarijn for being so gentle, considerate, and creating such a trustful environment for us during the meetings.

Special thanks to Özge, Damla, Valentina, Mustafa and Ezgi.. Ah, we had so many things together in Delft, cannot be put into words.. Your friendship and support in Delft

was so precious to me.. Thank you very much for everything! Çiğdem, seninle gerek sohbet etmek gerekse de çalışmak çok güzeldi, çok teşekkür ederim her şey için! Kudret ve Ferize teyzelerim, size de ayrıca çok teşekkür etmek isterim. Hollanda'ya taşındığım zamandaki desteğiniz hem ailem hem de benim için çok kıymetliydi.

Canım anneciğim, babacığım ve biriciğim Deryam.. Sadece doktora sürecinde değil her zaman yanımda olup her koşulda beni desteklediğiniz için, koşulsuz sevginiz için, beraber ağlayıp beraber güldüğümüz için, bütün paylaştıklarımız için, bana öğrettiğiniz ve bana kattığınız her şey için size minnettarım. İyi ki varsınız.. Ve iki gözümün iki çiçeği Berkin ve Ekin.. İyi ki ailemize katıldınız bitanelerim, dünyamıza renk kattınız.. Her zamanki desteği ve sevgisinin yanında, en çok da sizler için canım ablam Dilek'e sonsuz teşekkürler.. Hepinizi çok seviyorum, iyi ki varsınız, iyi ki benim ailemsiniz..

This work is part of the research programme of the Foundation for Fundamental Research on Matter (FOM), which is part of the Netherlands Organisation for Scientific Research (NWO).

Melika Gül
Delft, October 2018

ABOUT THE AUTHOR

Melika Gül was born in Tunceli and grown up in Izmir, Turkey. She studied Aerospace Engineering (graduated with first rank) at Middle East Technical University (METU, Ankara, 2006-2010), where she also obtained her M.S. degree (2010-2013) as high honour student in experimental aerodynamics. Between Nov. 2010- Aug. 2014, she was employed full-time by METU as a teaching and research assistant. In 2014, she started her PhD research at Delft University of Technology (Delft, Netherlands, Sept. 2014- Oct. 2018), that was funded by the Foundation for Fundamental Research on Matter (FOM). She obtained her PhD title in October 2019 specializing in experimental fluid mechanics and turbulence. Since November 2018, she has been working at the University of Southampton (Southampton, UK) as a postdoctoral researcher.

LIST OF PUBLICATIONS

PAPERS:

[4] M. Gul, G. E. Elsinga, and J. Westerweel. "Internal Shear Layers and Edges of Uniform Momentum Zones in a Turbulent Pipe Flow." Under review. In: Journal of Fluid Mechanics.

[3] M. Gul, G. E. Elsinga, and J. Westerweel. "Experimental investigation of torque hysteresis behaviour of Taylor–Couette Flow." In: Journal of Fluid Mechanics 836 (2018), pp. 635–648.

[2] M. Gul and O. Uzol and I. S. Akmandor. "An experimental study on active flow control using synthetic jet actuators over S809 airfoil." In: Journal of Physics: Conference Series. 524 (2014), 012101.

[1] M. Gul and O. Uzol and I. S. Akmandor. "Flow Control with synthetic jet actuators under adverse pressure gradient boundary layer." In: 32nd AIAA Applied Aerodynamics Conference. 836 (2014).

SELECTED CONFERENCE CONTRIBUTIONS:

[7] M. Gul, G. E. Elsinga, and J. Westerweel. "Internal shear layers and uniform momentum zones in a turbulent pipe flow." 16th European Turbulence Conference, Stockholm, Sweden, 2017.

[6] M. Gul, G. E. Elsinga, and J. Westerweel. "Internal Shear Layers and Uniform Momentum Zones in a Turbulent Pipe Flow." 70th American Physical Society (APS) Division of Fluid Dynamics meeting, Denver, CO, USA, 2017.

[5] M. Gul, G. E. Elsinga, and J. Westerweel. "Internal Shear Layers in a Turbulent Pipe Flow." EUROMECH Colloquium 590:Turbulent/nonturbulent interfaces: from laboratory to geophysical scales. London, UK, 2017.

[4] M. Gul, G. E. Elsinga, and J. Westerweel. "In Pursuit of Turbulence: Large-Scale Motions in Turbulent Pipe Flow." Physics@Veldhoven. Veldhoven, The Netherlands, 2017.

[3] M. Gul, G. E. Elsinga, and J. Westerweel. "Experimental Investigation of Geometry on Torque Hysteresis Behaviour of Taylor-Couette Flow." 15th European Turbulence Conference, Delft, The Netherlands, 2015.

[2] M. Gul and O. Uzol and I. S. Akmandor. “Flow Control with synthetic jet actuators under adverse pressure gradient boundary layer.” 32nd AIAA Applied Aerodynamics Conference, Atlanta, USA, 2014.

[1] M. Gul and O. Uzol and I. S. Akmandor. “An experimental study on active flow control over S809 airfoil using synthetic jet actuators.” Conference on Wind Energy Science and Technology, Ankara, Turkey, 2013.